ROTATION CURVE MASS MODELING OF DISK GALAXIES

By

Aaron Ambrose Dutton

B. A. University of Cambridge, 1998

A THESIS SUBMITTED IN PARTIAL FULFILLMENT OF

THE REQUIREMENTS FOR THE DEGREE OF

MASTER OF SCIENCE

in

THE FACULTY OF GRADUATE STUDIES

DEPARTMENT OF PHYSICS AND ASTRONOMY

We accept this thesis as conforming

to the required standard

THE UNIVERSITY OF BRITISH COLUMBIA

April 2003

In presenting this thesis in partial fulfilment of the requirements for an advanced degree at the University of British Columbia, I agree that the Library shall make it freely available for reference and study. I further agree that permission for extensive copying of this thesis for scholarly purposes may be granted by the head of my department or by his or her representatives. It is understood that copying or publication of this thesis for financial gain shall not be allowed without my written permission.

Department of Physics & Astronomy

The University of British Columbia
Vancouver, Canada

Date 17th April 2003

DE-6 (2/88)

Abstract

The standard Cold Dark Matter (CDM) model for cosmological structure formation has been remarkably successful in explaining the observed large scale structure of the universe. At the scale of individual galaxies, however, CDM faces serious challenges; one of these is the apparent discrepancy between the steep density profiles found in cosmological N-body simulations and the flatter density profiles inferred from optical rotation curves of low surface brightness galaxies. We have developed a new comprehensive rotation curve mass modeling decomposition code and tested it on 6 mass modeling standards, previously studied by Blais-Ouellette (2000). Our decompositions allow for all cosmologically-motivated types of halos, thin or thick disks, variable disk M/L ratio, adiabatic contraction of the dark halo, and non-spherical halos. We investigate the allowed range of inner density profile shapes as a function of disk M/L ratio. This program is being developed for an upcoming application to a new sample of 24 high and low surface brightness galaxies with wide-field optical/IR imaging and high-resolution long-slit Hα rotation curves.

Table of Contents

List of Tables

List of Figures

Acknowledgments

First and foremost, I would like to thank my supervisor Stéphane Courteau, without whom this project would not have happened, for the guidance and confidence he has given me and whose enthusiasm and work ethics have motivated me to work harder. Secondly, I thank Douglas Scott for his careful reading of this thesis and providing useful comments. Thanks also to Claude Carignan for supplying electronic data files, John Dubinski for discussions about the triaxial shape of dark matter halos, and Joel Primack for discussions about adiabatic contraction.

Chapter 1

Introduction

1.1 Cosmological motivation

The Cold Dark Matter (CDM) paradigm and its variants (e.g. ΛCDM) have proved remarkably successful in explaining the observed large scale structure of the universe. Examples of these successes on large scales include: the abundance and clustering of galaxy clusters (Peacock et al. 2001; Verde et al. 2002; Lahav et al. 2002), the statistical properties of the Lyman$-\alpha$ forest (e.g. Phillips et al. 2001), and the power spectrum of the cosmic microwave background anisotropies (e.g. Jaffe et al. 2001, Hinshaw et al. 2003). On scales of individual galaxies, however, there exists a number of discrepancies between observations and the predictions of numerical simulations. These include:

- The "substructure" problem; CDM over-predicts by almost an order of magnitude the number of satellite galaxies observed in the Local Group (Klypin et al. 1999; Moore et al. 1999a; Hayashi et al. 2002).
- The "angular momentum" problem; Hydro-dynamical simulations of disk galaxy formation transfer too much angular momentum from the disk to the halo, resulting in disks that are a factor ~ 10 smaller than observed (Navarro & Steinmetz 1997; van den Bosch, Burkert, & Swaters 2001).
- The "density profile" problem; N-body simulations generate dark matter (DM) halos with central density cusps, ($\rho \propto r^{-1}$: Navarro, Frenk, & White 1996, 1997,

hereafter NFW, or $\rho \propto r^{-1.5}$: Moore et al. 1999b; Ghigna et al. 2000, hereafter MOORE), while a large number of rotation curves (RCs) of dwarf[1] and low surface brightness (LSB[2]) galaxies can only be modeled with halos with central density cores or shallower central density cusps (e.g. Flores & Primack 1994; Moore 1994; McGaugh & de Blok 1998; de Blok, McGaugh, & Rubin 2001a; Swaters et al. 2003).

There have been many theoretical attempts to explain these discrepancies, such as incorporating astrophysical processes into the models (stellar feedback, cooling, bars), numerical effects in the simulations and alterations of the CDM paradigm itself (self-interacting or warm dark matter), yet the discrepancies remain largely unresolved. For a review of the current status of the CDM paradigm, see Primack (2002).

These apparent discrepancies between CDM predictions and current observations occur on scales where baryonic processes become significant. Note, however, that the NFW and MOORE N-body simulations only included dark matter particles, leaving out baryons altogether. More recent cosmological simulations of galaxies including gas modeled with smoothed particle hydrodynamics (SPH) have at most $\sim 10^6$ particles within the virial radius, so modeling galaxies of $10^{11} - 10^{12}\mathrm{M}_\odot$ involves particle masses of $\sim 10^5\mathrm{M}_\odot$ (e.g. Valenzuela & Klypin 2002). Thus the treatment of star formation, stellar feedback, and stellar dynamics is necessarily oversimplified, and care must be taken when interpreting the results. Until the effects of baryonic processes on the distribution of DM in galaxies are understood and the resolution of N-body simulations is significantly improved, placing definitive constraints on CDM with observations on galaxy scales may

[1] Dwarf spiral galaxies are usually defined as having a maximum rotation velocity $v_{\max} < 100\,\mathrm{km\,s^{-1}}$ and/or a total magnitude $M_\mathrm{B} \geq -18$

[2] A LSB galaxy is usually defined as a disk galaxy with an extrapolated central disk surface brightness μ_0^B roughly 2 mag arcsec^{-2} fainter than the typical value for high surface brightness (HSB) galaxies of $\mu_0^\mathrm{B} = 21.65$ (Freeman 1970).

not be justified.

1.2 History of Rotation Curve Mass Modeling

The most convincing evidence of DM in galaxies is the existence of flat rotation curves whose nature can only be explained by a non-baryonic component. Mass modeling of the rotation curves of spiral galaxies provides an estimate of the dark mass fraction in galaxies, though other techniques can also be applied (e.g. gravitational lensing, velocity dispersions, and flaring of the HI disk). The contributions of the stellar disk and bulge to the observed rotation curve in spiral galaxies can often be scaled with mass-to-light ratios, $(M/L)_{\rm disk}$ and $(M/L)_{\rm bulge}$ respectively, to explain most of the inner parts of the rotation curve, the so-called "maximum-disk" hypothesis[3] (van Albada & Sancisi 1986). The rotation velocity for many spirals stays roughly constant out to a large radii rather than declining, as would be expected if the visible stars and gas provided all the gravitational mass.

The flatness of spiral galaxy rotation curves was established through extended optical rotation curves (e.g. Rubin, Thonnard, & Ford 1978, 1980) and more securely from extended HI rotation curves (Bosma 1978, 1981). HI observations have the advantage that the gaseous disk extends much further out than the optical disk, so the missing mass discrepancy, which increases with radius, is more pronounced. For example, in the spiral galaxy NGC 3198, a local stellar M/L ratio of at least 6000 $\mathrm{M}_{\odot}/\mathrm{L}_{\odot}^{\mathrm{B}}$ is required to explain the observed rotation at a radius of 11 disk scale lengths, which is 1400 times as large as the central M/L assuming a pure maximum disk (van Albada & Sancisi 1986).

Mass models based on extended HI rotation curves, with dark halos modeled as a pseudo-isothermal (ISO) sphere (which has a central density core), indicated that large

[3]We define a maximum disk as supplying more than 75 % of the disk to total velocity of a galaxy at 2.2 exponential scale lengths (the peak velocity of an exponential disk).

amounts of dark matter are required to explain the outer parts of rotation curves (van Albada et al. 1985; Begeman 1987; Broeils 1992). Typically 90% of the mass of spiral galaxies must be in dark form. Without an independent measurement of the stellar M/L ratios, however, the scaling of the bulge and disk components introduces uncertainties in the derived dark matter properties. This degeneracy can be partially lifted by limiting the sample to late-type, bulge-less, spiral galaxies, as these galaxies have little or no bulge, though the unknown value of $(M/L)_{\rm disk}$ remains a major source of uncertainty. It is often possible to obtain equally well fitting mass models from both maximum and minimum disks, leading to a wide range of dark halo parameters (Broeils & Courteau 1997; Swaters 1999; Courteau & Rix 1999).

It is believed that dwarf and LSB galaxies are dark matter dominated at all radii, and that therefore the analysis of their rotation curves can yield reliable information about the properties and distribution of their associated dark matter halos (de Blok & McGaugh 1997; Verheijen 1997; Swaters 1999). It has been found that rotation curves of dwarf and LSB galaxies rise less steeply than predicted by numerical simulations based on the CDM paradigm (Moore 1994[4]; Flores & Primack 1994[5]; de Blok & McGaugh 1997; McGaugh & de Blok 1998). These rotation curves show a nearly solid-body rise consistent with a mass distribution dominated by a central density core, which is inconsistent with the CDM predictions.

Early studies of dwarf and LSB rotation curves relied on HI 21 cm data, obtained at the VLA and WRST radio synthesis telescopes (e.g. van der Hulst et al. 1993; de Blok, McGaugh & van der Hulst 1996), which may suffer from angular resolution effects. Beam smearing results in an underestimation of the rotation velocity in the rising part of the rotation curve, and hence biases to shallower density profiles. This effect can

[4]NGC 3109, DDO 105, DDO 154, DDO 170
[5]DDO 154, DDO 168

be partially corrected for (Bosma 1981; Begeman 1987; Swaters 1999), though van den Bosch & Swaters (2002) conclude that the current HI data (typical beam size of $15'' - 50''$) are not of high enough resolution to support or challenge the NFW hypothesis. Higher resolution data are necessary to constrain the slope of the rising part of the rotation curve and hence the inner density profile of the DM halo. These can be obtained from optical emission lines, such as Hα(6563Å) or [NII], or molecular CO if present at 2.6 mm. The greater radial coverage of HI rotation curves is still needed to further constrain the halo parameters. Studies based on Hα alone fail to distinguish between cusps and cores (e.g. Jimenez, Verde, & Oh 2002).

Swaters, Madore & Trewhella (2000) obtained supplementary Hα data for five LSB galaxies[6] previously observed in HI by de Blok et al. (1996), and concluded that the effect of beam smearing on the HI curves was severe enough to question earlier conclusions regarding dark matter content and rotation curve shape of LSB galaxies. McGaugh, Rubin & de Blok (2001) and de Blok, McGaugh & Rubin (2001a) reanalyzed the Swaters et al. (2000) data to show that the discrepancy between Hα and HI data is only significant for one of the five galaxies; thus the conclusions of de Blok et al. (1996) are apparently still valid. In a comparison of ISO and NFW halo models using HI and high-resolution Hα rotation curves for a further 29 LSB galaxies, de Blok et al. (2001a) showed that the NFW halo profile is not a good description of the data: the observed rotation curves generally show linear solid-body rise in the inner parts, which is inconsistent with the steeper NFW density profile. Rather, the rotation curve decompositions favor a core dominated halo model, such as ISO.

A different approach was taken by de Blok et al. (2001b); who fitted mass density profiles to the rotation curves of *all* LSB galaxies measured thus far by assuming a spherical halo and that the galaxies are dark matter dominated. They find that; "Mass

[6] D563-02, F568-01, F568-03, F568-V01, F574-01

density profiles of LSB galaxies exhibit inner slopes that are best described by a power-law $\rho(r) \propto r^{-\alpha}$ with $\alpha = 0.2 \pm 0.2$." Their analysis is based on zero-disk models, so we expect this to be an upper limit on α. Furthermore, the steep slopes found for some LSB galaxies arise when the innermost data point samples the transition region between the core and the outer $\alpha = 2$ isothermal region, not the core itself. This illustrates the need for rotation curves of the highest possible resolution.

Other studies also indicate that the steep rotation curves implied by CDM can hardly be reconciled with the observed shallow rotation curves of dwarf galaxies (Blais-Ouellette 2000; Blais-Ouellette, Amram & Carignan 2001; Côté, Carignan & Freeman 2000; Marchesini et al. 2002).

1.3 Research Goals

Cold Dark Matter models and observations conflict mostly where both simulations and data are least trustworthy: the inner few kpc of dwarf and LSB galaxies. The major observational uncertainties on these scales are the poorly determined dynamics and the unknown contribution of stars and gas to the rotation curve. Close to the centre of galaxies, effects of slit position error, non-circular motions (e.g. bars, spiral arms, intrinsic velocity dispersion), and extinction from dust are potentially significant. It is generally believed that HSBs may be consistent with NFW halos, but their mass modeling is also hindered by a more prominent stellar component, which can mimic the presence of a cuspy halo. The unknown value of the stellar M/L makes it hard to discriminate between cusps (e.g. NFW) and cores (e.g. ISO) in these bright galaxies. Lower M/L usually favor cuspy profiles, while high M/L favor cores.

To address these issues, S. Courteau (UBC) and R. de Jong (STSCI) obtained high-resolution long-slit (LS) Hα rotation curves and multi-band (BVRIJHK) imaging at

Steward Observatory for a sample of spiral galaxies with existing HI rotation curves (mostly from Broeils 1992). This sample includes dwarf, LSB and HSB galaxies. The Hα spectra provide highly-resolved rotation curves and the infrared imaging yields the tightest M/L estimates, free from the effects of dust extinction.

Surface photometry of rotation curve galaxies in the past has relied mostly on optical band passes which do not sample the stellar mass distribution accurately, but are sensitive to young stellar populations and dust extinction. However, infrared (IR) bands sample most of the galaxy light from the old stars that dominate the underlying stellar mass. The effects of dust extinction are typically 10 times less at K-band than at B-band. Most of the dust extinction occurs in the central regions of galaxies, precisely where rotation curve fitting is so sensitive. Furthermore, M/L^{K} ratios of stellar populations can only take a limited range of values. By combining infrared and optical photometry we can constrain M/L^{K} even further (Bell & de Jong 2001).

Few mass modeling studies of late-type galaxies have used a combination of optical and radio rotation curves (e.g. de Blok et al. 2001a; Blais-Ouellette 2000; Swaters et al. 2000), and none have exploited infrared imaging, which is pivotal for the determination of realistic stellar mass distributions. This is one of the key new features of our ongoing study.

A number of practical issues must be addressed before we can fully achieve our goals, which are described below.

1.4 This Thesis

In order to test our mass decomposition algorithm, we used 6 galaxy mass modeling standards previously studied by Blais-Ouellette (2000) and Blais-Ouellette et al. (2001). Our mass models are described in §2. Their components include a thin gaseous disk, a thick stellar disk and a dark halo. All previous rotation curve studies have assumed a spherical dark halo but this may be an over- simplification. CDM simulations suggest triaxial shapes for collapsed structures that are asymmetric so that halos are asymmetric even in the plane of the disk, with typical axis ratios $c/a = 0.5 - 0.7$, and $b/a = 0.7 - 0.9$ (Dubinski & Carlberg 1991; Jing & Suto 2002; Tinker & Ryden 2002, see Figs 1.1−1.3). The dissipative infall of gas in non-baryonic dark halos suppresses triaxial structures leading to halos with an oblate shape (Katz & Gunn 1991; Dubinski 1994). This agrees with HI observations that find axially symmetric disks with a very low upper limit for the eccentricity: below 0.1 with the isophote shape versus HI velocity widths (Merrifield 2002), or even less than 0.045, when using near-infrared data to avoid extinction (Rix & Zaritsky 1995). The axisymmetric shape of galactic halos is confirmed by the low scatter in the Tully-Fisher relation (Eisentein & Loeb 1996). The flattening of the halo is harder to measure but various techniques, including the flaring of HI disks, polar rings around spiral galaxies, and X-ray isophotes of elliptical galaxies, find oblate halos with axis ratio, $q = c/a$, from 0.1 to 0.9. Thus, we are compelled to study the effects of axially symmetric dark halos ($b/a = 1$) in our mass models with a conservative range of axis ratios $0 < q < 1.5$.

The radial density profile of pure CDM halos may also be altered by the dissipative infall of gas, and stellar feedback from the subsequent star formation. These two processes should have the opposite effect; infall of baryons will cause the halo to contract (Blumenthal et al. 1986), while the expulsion of gas via supernovae winds will cause the disk and halo to expand (Gnedin & Zhao 2002). It was initially postulated that feedback could substantially reduce the cuspiness of DM halos (Navarro, Eke & Frenk 1996), though more recent models suggest that gas heating and winds play an insignificant role for halos of greater than $10^7 M_\odot$ (Mac Low & Ferrera 1999; Navarro & Steinmetz 2000). We describe the adiabatic contraction model in §2.4, but ignore the (small) effect of halo expansion due to stellar feedback.

The galaxy mass modeling standards upon which our tests are based are presented in §3. The data consist of 2D HI and Hα rotation curves, HI surface densities, and B and/or R band surface photometry. The galaxies have a range of central surface brightnesses from HSB to LSB [$21.9 \le \mu_0^{\rm B} \le 23.4$][7] and rotation curve shapes. In §4 we describe our numerical methods for computing the mass models, and the non-linear optimization method we use to fit our mass models to the observed rotation curve. We present our rotation curve fits in §5 and compare our derived parameters with those of Blais-Ouellette et al. (2001) in §5.1. Next, we discuss the effect of systematic errors on the decompositions including: photometry parameters, distance estimate, and rotation curve error bars. In §5.3, we present the results of a two-parameter halo fit with a range of halo shapes and $(M/L)_{\rm disk}$ for both adiabatically contracted and non-contracted halos. In §5.4 we use constraints from Tully-Fisher and lensing arguments for bright galaxies in an attempt to break the mass modeling degeneracies. Conclusions are presented in §6, and derivations of fundamental relations and formulae for rotation curves are given in Appendices A–E.

[7]From Blais-Ouellette (2000), corrected for inclination and extinction.

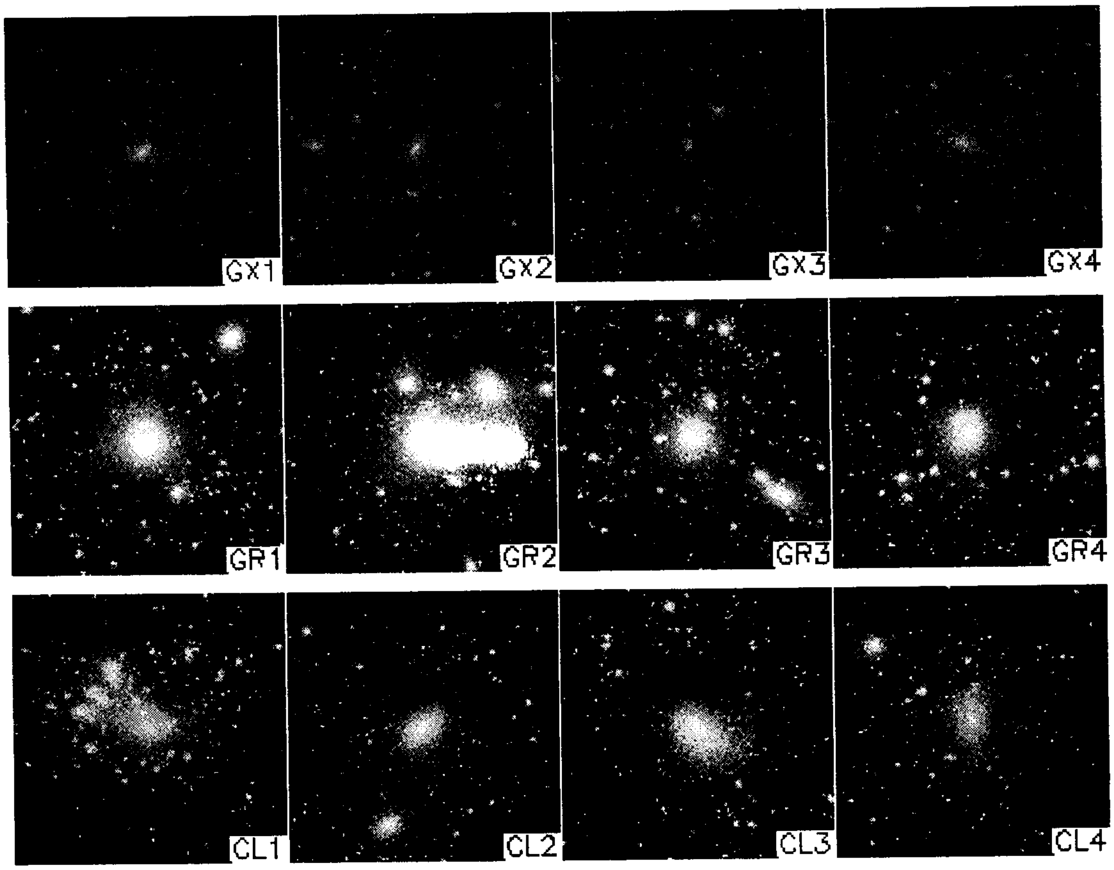

Figure 1.1: Snapshots of simulated halos at $z = 0$. Top, centre, and bottom panels display the halos of galaxy, group, and cluster masses respectively. The size of each panel corresponds to $2r_{\rm vir}$ of each halo (from Jing & Suto 2000).

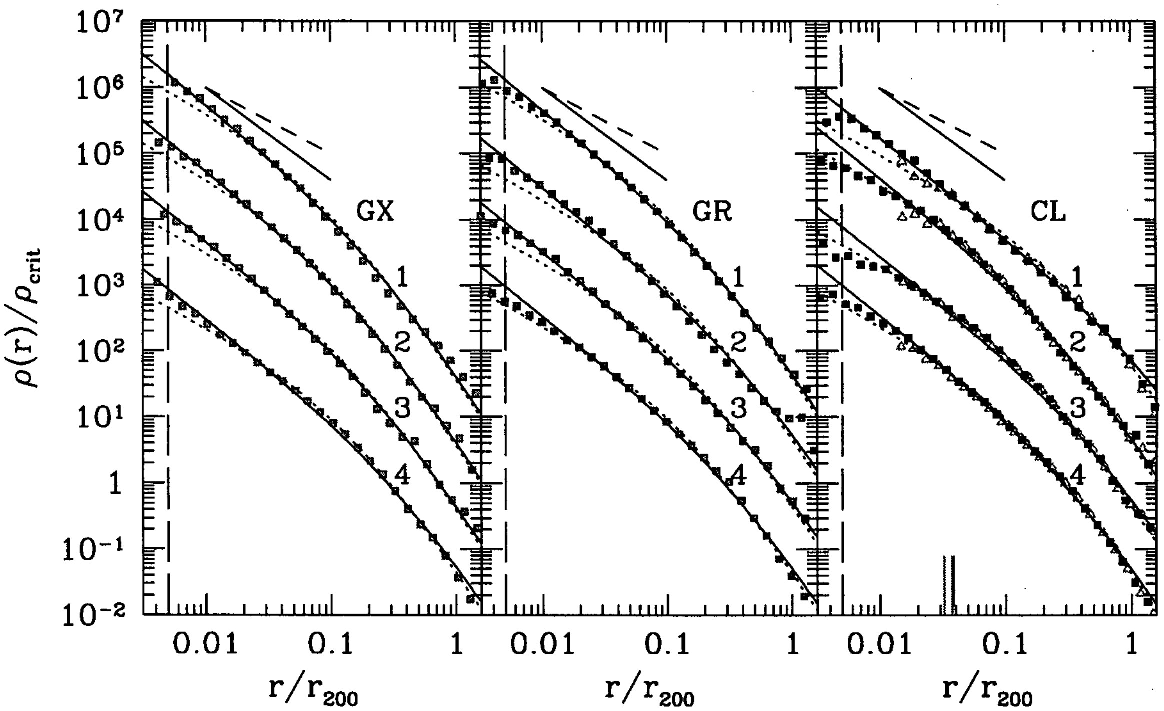

Figure 1.2: Spherically averaged radial density profiles of the simulated halos of galaxy (left), group (middle), and cluster (right) masses from Fig. 1. The solid and dotted curves represent fits of $\alpha = 1.5$ and $\alpha = 1.0$ respectively. For reference $\rho(r) \propto r^{-1}$ and $r^{-1.5}$ for the dashed and solid lines, respectively (from Jing & Suto 2000).

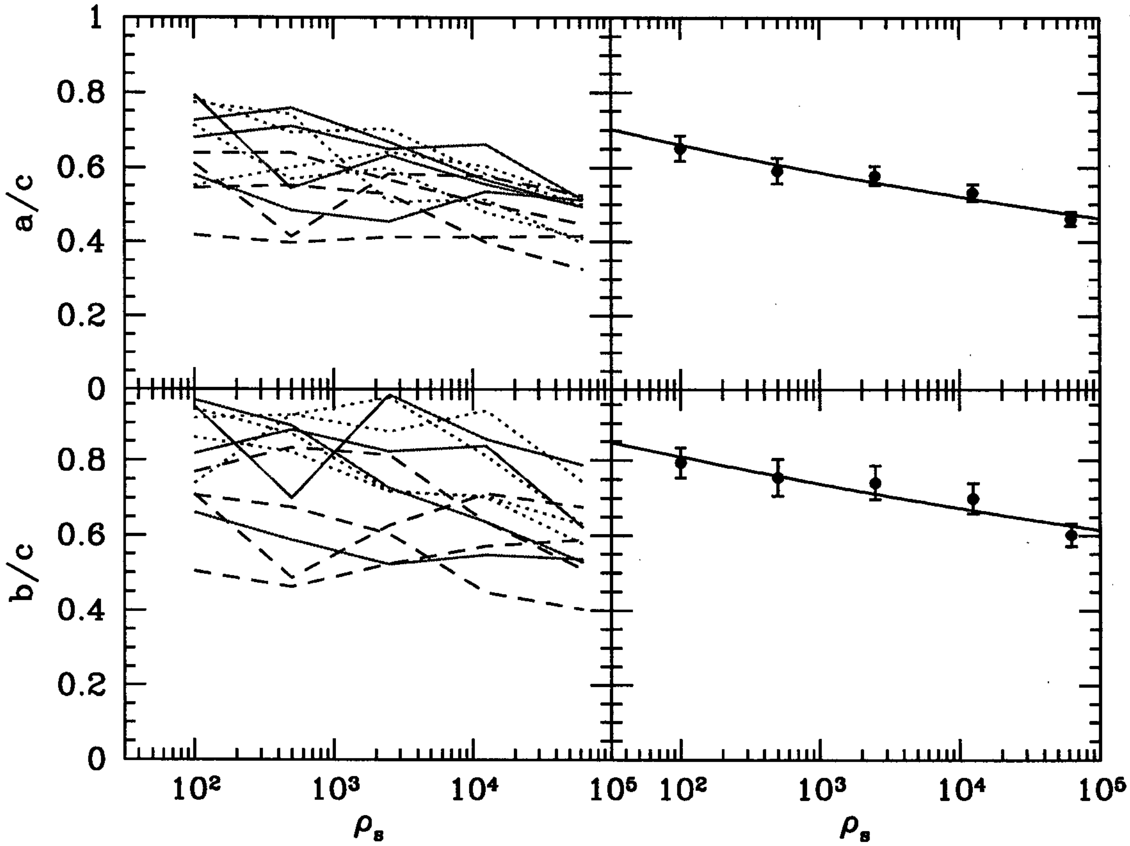

Figure 1.3: Axis ratios for the triaxial model fits of 12 halos in Fig. 1.1. *Left*: results for individual halos. The dashed, dotted and solid lines correspond to cluster, group, and galactic halos, respectively. *Right*: solid circles indicate the mean and its one-sigma error from the halo simulations, while the solid lines show a single power-law fit. The upper and lower panels show a/c and b/c, respectively (from Jing & Suto 2002).

Chapter 2

Mass Models

Our mass models assume three main components for each spiral galaxy: an infinitesimally thin gas disk (hereafter the "gas"), a thick stellar disk (hereafter the "disk"), and an oblate/prolate dark halo (hereafter the "halo"). None of the galaxies in our sample have a significant bulge (by selection), and we therefore ignore this component for our modeling exercise. Our models also assume that the matter distribution is axially symmetric and is in virial equilibrium. Thus material will follow circular orbits, with velocity in the plane of the disk at radius R given by

$$v_{\mathrm{rot}}^2(R) = -RF_R = R\frac{\partial\Phi}{\partial R}, \tag{2.1}$$

where F_R is the radial force, and Φ the gravitational potential. The gravitational potential of a galaxy is the sum of the gravitational potentials of the individual mass components. Expressed in velocities, this sum becomes

$$v_{\mathrm{rot}}^2 = v_{\mathrm{gas}}^2 + v_{\mathrm{disk}}^2 + v_{\mathrm{halo}}^2, \tag{2.2}$$

at each radius R. To compute the contributions from the gas and disk in the $z = 0$ plane, we use the formulation of Casertano (1983; see App. A for a derivation):

$$v^2(R, z=0) = -R\,4\pi G \int_0^\infty du \int_{-\infty}^{\infty} d\zeta\, \frac{1}{\pi}\sqrt{\frac{u}{Rp}}\,[\mathcal{K}(p) - \mathcal{E}(p)]\,\frac{\partial}{\partial u}[\rho(u,\zeta)] \tag{2.3}$$

$$p = x - \sqrt{x^2 - 1} \quad , \quad x = \frac{R^2 + u^2 + \zeta^2}{2\,R\,u}, \tag{2.4}$$

where (R, z) are cylindrical polar coordinates, (u, ζ) are the corresponding integration variables, $\mathcal{K}$ and $\mathcal{E}$ are complete elliptic integrals of the first and second kinds respectively, and $\rho(R, z)$ is the mass density. For a disk of zero thickness the density reduces to

$$\rho(R, z) = \delta(z)\, \Sigma(R), \tag{2.5}$$

where $\delta(z)$ is the Dirac delta function, and $\Sigma(R)$ is the radial surface density.

For an axially symmetric halo, with axis ratio $q = c/a$ and eccentricity $e = \sqrt{1 - q^2}$, the circular velocity in the $z = 0$ plane is given by (Binney & Tremaine, 1987; Eq. 2.91)

$$v_{\text{halo}}^2(r) = \frac{G}{r} \int_0^r \frac{\rho(u)}{\sqrt{1 - e^2 \frac{u^2}{r^2}}} 4\pi\, q\, u^2 du, \tag{2.6}$$

where r is the elliptical radius defined by

$$r^2 = R^2 + \frac{z^2}{q^2}, \tag{2.7}$$

and u is the corresponding integration variable. When $q = 1$, r reduces to the spherical radius and the integrand in Eq.(2.6) reduces to the mass within radius r

$$M_{\text{halo}}(r) = \int_0^r \rho(u) 4\pi\, q\, u^2 du \tag{2.8}$$

and

$$v_{\text{halo}}^2(r) = \frac{G\, M_{\text{halo}}(r)}{r}. \tag{2.9}$$

To compute the integrals in Eqs. (2.3) and (2.6), we need to know the mass density of each component. How we do this is explained below.

2.1 Gaseous Disk

The surface density of neutral hydrogen is obtained from the HI 21 cm observations, once the orientation parameters are known. Assuming the neutral gas to be optically thin, the column density of HI is given by (Begeman 1987)

$$N_{\rm HI} = \frac{4.6 \times 10^{18}\, T\, \sigma\, I_0}{I_{\rm C}}, \tag{2.10}$$

where T is the temperature of the neutral hydrogen, σ is its velocity dispersion, I_0 the maximum absorption, and $I_{\rm C}$ the continuum flux density. The column density can be converted into a surface density via

$$\Sigma_{\rm HI}\ [\,{\rm M_\odot\,pc^{-2}}\,] = 0.802 \times 10^{-20}\,{\rm N_{HI}}\ [\,{\rm atoms\,cm^{-2}}\,], \tag{2.11}$$

where we have used the mass of hydrogen $m_{\rm H} = 1.674 \times 10^{27}\,$kg, the mass of the Sun $\rm M_\odot = 1.989 \times 10^{30}\,$kg, and 1 pc $= 3.086 \times 10^{18}\,$cm. To take into account the presence of helium, we divide the HI surface density by the fraction of gas in HI, $f_{\rm HI}$, which we take to be 0.75 (e.g. Blais-Ouellette et al. 2001). Other authors take $0.71 \leq f_{\rm HI} \leq 0.77$, though the exact value is not critical, especially considering the relatively small contribution of the gaseous disk to the rotation curve. Thus, assuming a thin disk, the gas density expressed in cylindrical polar coordinates (R, z) is given by

$$\rho_{\rm gas}(R, z) = \delta(z)\, \Sigma_{\rm HI}\ (R)/f_{\rm HI}\ . \tag{2.12}$$

Some spiral galaxies show a central depression in the HI density, likely due to the gas being present in a different form (ionized or molecular) and/or partial or complete consumption in previous episodes of star formation. A central depression and hence a positive radial density gradient results in an outward radial force or negative v^2. We represent this as negative velocity on the gaseous component of the rotation curve.

2.2 Stellar Disk

We obtain the radial mass distribution from the observed surface brightness profile, $\mu^\lambda(R)$, where λ is the band pass. The surface brightness is a logarithm of the intensity expressed in observational units of $[\,{\rm mag\,arcsec^{-2}}\,]$ and which can be converted into physical units of $[\mathrm{L}_\odot\,\mathrm{pc}^{-2}]$ (see App. B for the derivation) via,

$$I(R) = 206265^2\,10^{(\mathrm{M}^\lambda_\odot - 5 - \mu^\lambda(\mathrm{R}))/2.5} \tag{2.13}$$

where $\mathrm{M}^\lambda_\odot$ is the absolute specific magnitude of the Sun. The intensity or surface brightness can then be converted into a surface density by multiplying by a mass-to-light ratio

$$\Upsilon^\lambda_{\mathrm{disk}} = \frac{M(R)}{L^\lambda(R)}, \tag{2.14}$$

with mass and luminosity in solar units. In general $\Upsilon^\lambda_{\mathrm{disk}}$ can be a function of radius though it is usually set to be constant. This can be justified if the radial colour gradients are small and the disk vertical scale height does not change appreciably with radius. Thus,

$$\Sigma(R) = \Upsilon^\lambda_{\mathrm{disk}}\,206265^2\,10^{(\mathrm{M}^\lambda_\odot - 5 - \mu^\lambda(\mathrm{R}))/2.5}. \tag{2.15}$$

2.2.1 Radial Luminosity Profile

To a first approximation, the stellar disk can be modeled with a radial exponential profile of zero thickness

$$\Sigma(R) = \Sigma_0\,e^{-R/R_{\mathrm{d}}}, \tag{2.16}$$

which has mass

$$M_{\mathrm{disk}}(R) = 2\,\pi\,\Sigma_0\,R_{\mathrm{d}}^2\left\{1 - \left(1 + \frac{R}{R_{\mathrm{d}}}\right)\,e^{-R/R_{\mathrm{d}}}\right\}, \tag{2.17}$$

where R_{d} is the scale length of the disk and Σ_0 is the central surface density. These parameters are obtained from a linear fit to the surface brightness profile,

$$\mu^\lambda(R) = \mu^\lambda_0 + 1.0857\frac{R}{R_{\mathrm{d}}}, \tag{2.18}$$

where μ^λ_0 is the central surface brightness and can be converted into a central surface density via Eq. (2.15). The rotation velocity of an exponential disk is given by (Freeman

1970; see App. C for a derivation)

$$v_{\rm disk}^2(R) = 4\,\pi\,G\,\Sigma_0\,R_{\rm d}^2\,[I_0(y)K_0(y) - I_1(y)K_1(y)], \tag{2.19}$$

where I_n and K_n are modified Bessel functions of order n of the first and second kinds respectively, and $y = \frac{R}{2R_{\rm d}}$. Note that the exponential disk has a peak velocity at 2.15 disk scale lengths given by

$$v_{\rm disk}^{\rm max}(2.15\,R_{\rm d}) = 0.88\,\sqrt{\pi\,G\,\Sigma_0\,R_{\rm d}}. \tag{2.20}$$

Luminosity profiles often deviate significantly from the idealized exponential (Courteau 1996) thus, for the purpose of measuring disk masses, we use the radial surface density computed directly from the measured radial surface brightness profile with Eq. (2.15).

2.2.2 Vertical Luminosity Profile

From observations of the surface brightness distributions of edge-on disk galaxies, van der Kruit & Searle (1981a,b; 1982a,b) proposed the self-gravitating isothermal[1] sheet (Spitzer 1942) as a model for the description of the vertical light distribution:

$$L(z) = L_0\,\mathrm{sech}^2(z/z_0), \tag{2.21}$$

where L_0 is the surface luminosity in the plane of the galaxy, z is the distance from the galaxy plane, and z_0 is the vertical scale height. Van der Kruit & Searle also found that the disk has an intrinsic thickness $q_0 \equiv z_0/R_{\rm d}$ of $\sim 1/6$. More recent studies using near-IR observations of a much larger sample of galaxies find $q \simeq 0.25$ and an excess of light over the isothermal sheet at small distances from the galaxy planes, where optical photometry is strongly affected by dust extinction. This excess can be better fitted with

[1] An isothermal sheet is defined by the condition that the vertical velocity dispersion, $\langle v_z^2\rangle^{1/2}$, is independent of z

an exponential distribution,

$$L(z) = L_0 \exp(-z/h_z) \tag{2.22}$$

where h_z is the vertical scale length. At large z, the isothermal sheet reduces to the exponential model with $z_0 = 2h_z$. Though at small z the exponential distribution often over predicts the luminosity, leading to the proposal by van der Kruit (1988) of the following family of density laws for stellar disks,

$$L(z) = 2^{-2/n} \frac{L_0}{2\, z_0} \operatorname{sech}^{2/n}(nz/z_0)\,,\ (n > 0) \tag{2.23}$$

where the isothermal model is at the $n = 1$ extreme and the exponential is the other extreme for $n = \infty$. De Grijs, Peletier, & van der Kruit (1997) found a mean value for $2/n$ in the K' band of 0.538 ± 0.198 ($n = 3.72^{+2.17}_{-1.00}$) which rules out the isothermal sheet. However, in practice the differences in the rotation curves between different values of n are small, as is shown in Fig. (2.1) for an exponential disk.

Kregel, van der Kruit & de Grijs (2002) analyzed I-band brightness profiles for 34 edge-on late-type galaxies, fitting an exponential vertical profile to a region $|z| > 1.5\, h_z$, finding a range of radial to vertical scale lengths of $4 < R_d/h_z < 20$ with a mean value of $R_d/h_z = 8.5 \pm 2.9$. If we restrict the galaxies to $v_{max} < 160\,\mathrm{km\,s^{-1}}$ as the representative range for the galaxies studied here, we find $R_d/h_z = 7.9 \pm 1.7$, corresponding to an intrinsic disk thickness $q_0 = 0.25 \pm 0.05$. The exact value of q_0 for mass modeling is not critical as is shown in Fig. (2.2) where we display the rotation curve for a radial exponential disk with a sech^2 vertical profile and $q_0 = 0, 0.1, 0.2$ and 0.3.

2.2.3 Radial Truncation

Kregel et al. (2002) show that the light distribution in at least 20 out of 34 studied galaxies is radially truncated, finding a tight correlation between truncation radius R_{max} and disc scale length R_d with an average $R_{max}/R_d = 3.6 \pm 0.6$. This is consistent with previous similar studies. The effect of radial truncation on the rotation curve of an exponential disk is illustrated in Fig. (2.3), and can significantly reduce the rotation velocity of the disk. However, the effect on mass models is usually not significant due to the dominating contribution of the halo at the (large) truncation radii of spiral galaxy disks.

2.2.4 Adopted Disk Density Profile

In summary, we model the stellar disk with a radial density distribution derived directly from the surface brightness profile (Eq. 2.15), and adopt a vertical sech^2 light profile (Eq. 2.21) with an intrinsic thickness $q_0 = z_0/R_\mathrm{d} = 0.25$, such that,

$$\rho_\mathrm{disk}(R, z) = \frac{\Sigma(R)\,\mathrm{sech}^2(z/z_0)}{2z_0} \tag{2.24}$$

2.3 Dark Halo

In some cases the contribution from stars and gas can be scaled to explain the inner parts of galaxy rotation curves (the maximum-disk hypothesis), though no realistic scaling of the disk can explain the flat outer rotation curves observed in most HSB galaxies. One way to resolve this discrepancy is to assume that galaxies are embedded in dark matter halos.

2.3.1 Isothermal Density Profiles

Early work assumed the dark matter density profile of disk galaxies was described by a pseudo-isothermal (ISO) sphere (Bosma 1981; van Albada et al. 1985; Begeman 1987) with

$$\rho_\mathrm{ISO}(r) = \frac{\rho_0}{1 + (r/r_\mathrm{c})^2}, \tag{2.25}$$

where ρ_0 is the central density, and r_c is the core radius. Although this specific density profile has no physical motivation, the density profile

$$\rho(r) = \rho_0 \, r^{-2}, \tag{2.26}$$

known as a singular-isothermal (SISO) sphere, is the power-law solution for the hydrostatic balance of a self-gravitating isothermal[2] ideal gas (Binney & Tremaine 1987; Eq. 4.115a)

$$\frac{dp}{dr} = \frac{k_B T}{m}\frac{d\rho}{dr} = -\rho \frac{G\,M(r)}{r^2}, \tag{2.27}$$

with $\rho_0 = \frac{2\,k_B\,T}{4\,\pi\,G\,m}$. Here k_B is Boltzmann's constant, p and T are the pressure and temperature of the gas, and m is the mass per particle. $M(r)$ is the total mass interior to radius r, which increases linearly with radius for SISO, and hence the rotation velocity is independent of radius, in agreement with observations of flat outer rotation curves. A core radius is included in the model to account for the solid body rise of observed rotation curves due to the presence of baryons.

The rotation curve of a pseudo-isothermal sphere is,

$$v_{\mathrm{ISO}}^2(r) = 4\,\pi\,G\,\rho_0\,r_c^2 \left\{1 + \frac{r_c}{r} \arctan(r/r_c)\right\}, \tag{2.28}$$

with an asymptotic velocity

$$v_\infty^2 = 4\,\pi\,G\,\rho_0\,r_c^2. \tag{2.29}$$

2.3.2 CDM Density Profiles

In a CDM universe structure builds up hierarchically, with small scales collapsing first. This can be modeled analytically in the regime where matter perturbations are linear, or weakly non-linear (Press & Schechter 1974; Cole et al. 1993), but the formation

[2] The structure of an isothermal self-gravitating sphere of gas is identical with the structure of a collisionless system of stars with a Maxwellian velocity distribution.

of galaxies is highly non-linear and direct computation through N-body simulations is required (see Fig. 2.4 for a time sequence of galaxy formation from an N-body simulation of a cluster of galaxies by Moore 2000). These simulations generate collapsed halos of dark matter that have steep central density profiles, and cannot therefore be modeled with ISO. NFW proposed a universal density profile (i.e. one that is independent of the mass and redshift of the system), based on simulations with virial masses between $3 \times 10^{11} M_\odot$ to $3 \times 10^{15} M_\odot$ and having $\sim 5000 - 10000$ particles within the virial radius:

$$\rho_{\rm NFW} = \frac{\delta_{\rm c}\,\rho_{\rm crit}}{(r/r_{\rm s})(1 + r/r_{\rm s})^2}. \tag{2.30}$$

This density profile has an inner logarithmic slope of -1 and an outer slope of -3, $r_{\rm s}$ is the scale radius where the slope is -2, $\delta_{\rm c}$ is the characteristic over-density of the halo, and $\rho_{\rm crit}$ is the critical density of the universe for $\Omega = 1$. The critical density is:

$$\rho_{\rm crit} = \frac{3H^2}{8\pi G} = 2.78\,h^2 \times 10^{-7}\,{\rm M}_\odot\,{\rm pc}^{-3}, \tag{2.31}$$

where $H = 100h\,{\rm km\,s^{-1}\,Mpc^{-1}}$ is the current value of the Hubble constant[3]. We use $h = 0.75$. Specifying the halo density by $\delta_{\rm c}$ and $r_{\rm s}$, the circular velocity for NFW is,

$$v^2_{\rm NFW} = 4\,\pi\,G\,\delta_{\rm c}\,\rho_{\rm crit}\,r_{\rm s}^2 \left\{-\frac{1}{1+x} + \frac{\ln(1+x)}{x}\right\}, \tag{2.32}$$

where $x \equiv r/r_{\rm c}$. Alternatively, the halo density can be specified in terms of a concentration parameter, c, and a radius, r_{200}, where the mean density of the halo is 200 times the critical density,

$$200\,\rho_{\rm crit} = \frac{M(r_{200})}{\frac{4}{3}\,\pi\,r_{200}^3}, \tag{2.33}$$

note that there is ambiguity here, because some authors use different definitions, e.g. $200\,\Omega_{\rm M}\,\rho_{\rm crit}$. The concentration parameter is defined as

$$c \equiv \frac{r_{200}}{r_s}. \tag{2.34}$$

[3] $H_0 = 72 \pm 8\,{\rm km\,s^{-1}\,Mpc^{-1}}$ (HST H_0 key project: Freedman et al. 2001).

In a CDM cosmology, r_{200} is approximately the virial radius[4], though in the currently favored ΛCDM cosmology with $\Omega_{\rm m} \equiv 1 - \Omega_\Lambda = 0.3$, the virial radius is about 30% larger (Klypin 2000). The mass enclosed within a radius r is given by,

$$M(r) = 4\,\pi\,\delta_{\rm c}\,\rho_{\rm crit}\,r_{\rm s}^3 \left\{ -\frac{x}{1+x} + \ln(1+x) \right\}. \tag{2.35}$$

At r_{200}, $x = c$, and substituting Eq. (2.35) into Eq. (2.33) gives

$$\delta_{\rm c} = \frac{200}{3} \frac{c^3}{\ln(1+c) - c/(1+c)}. \tag{2.36}$$

Thus the virial mass is specified (roughly) by r_{200} and is given by

$$M_{200} = \frac{800\,\pi}{3}\,\rho_{\rm crit}\,r_{200}^3 = 2.32 \times 10^5\,h^2\,r_{200}^3 \tag{2.37}$$

with M_{200} and r_{200} in $M_\odot$ and kpc respectively, and the virial velocity is

$$v_{200}^2 = \frac{G\,M_{200}}{r_{200}} = 100\,H_0^2\,r_{200}^2 \Rightarrow v_{200}\,[\,{\rm km\,s^{-1}}\,] = h\,r_{200}\,[\,{\rm kpc}\,]. \tag{2.38}$$

This equation holds for all spherical halos. The circular velocity (Eq. 2.32) can be expressed in terms of c and v_{200}

$$v_{\rm NFW}^2(r) = v_{200}^2\,c\,\frac{\ln(1+x) - x/(1+x)}{\ln(1+c) - c/(1+c)}. \tag{2.39}$$

The adequacy of the NFW profile has been confirmed by a number of subsequent studies with higher resolution (Cole & Lacey 1996; Huss, Jain & Steinmetz 1999; Jing & Suto 2000), although there is some disagreement for the innermost value of the logarithmic slope, $-\alpha$ (perhaps due to resolution effects). Moore et al. (1998,1999b), Ghigna et al. (2000), and Fukushige & Makino (1997, 2001) have argued that $\alpha \simeq 1.5$ (hereafter refered to as the MOORE profile). Despite these differences, there is a general consensus

[4]The virial radius is the location where cosmological perturbations turn around and separate from the universal expansion for the first time.

that the density profile can be generalized by a double power law profile of the form (hereafter ALP):

$$\rho_\alpha(r) = \frac{\rho_0}{x^\alpha(1+x)^{3-\alpha}}\,, \quad x = \frac{r}{r_{\rm s}}, \quad \rho_0 = \delta_{\rm c}\,\rho_{\rm crit}. \tag{2.40}$$

This density profile has a logarithmic slope

$$\beta(x) = \frac{d\,\ln(\rho)}{d\,\ln(x)} = \frac{x}{\rho}\frac{d\rho}{dx} = -\alpha + (\alpha-3)\frac{x}{1+x} = -\frac{\alpha+3x}{1+x}, \tag{2.41}$$

thus

$$\rho(r) = \rho(r_{\rm s})\,\exp\left\{\int_1^{r/r_{\rm s}} \frac{\beta(x)}{x}dx\right\}. \tag{2.42}$$

The scale radius $r_{\rm s}$ corresponds to the radius where the density slope is

$$\beta(1) = -\frac{1}{2}(\alpha+3). \tag{2.43}$$

For comparsion, the ISO and Burkert (Burkert 1995) profiles have the following density slopes

$$\beta(x)_{\rm ISO} = -\frac{2x^2}{1+x^2}, \tag{2.44}$$

$$\beta(x)_{\rm BUR} = -\frac{2x^2}{1+x^2} - \frac{x}{1+x}. \tag{2.45}$$

The differences between the NFW and MOORE profiles are only apparent at small radii where effects of resolution are most conspicuous. At these scales the density contrast exceeds $\sim 10^6$ and N-body realizations must be able to track particles accurately for several thousand orbits. Few cosmological N-body codes have been tested in a systematic way under such circumstances. Extreme care is thus needed to separate numerical artifacts from true predictions of the CDM model. Furthermore, there are *no* simulations with adequate resolution of dark matter halos having the masses and densities of dwarf and LSB galaxies, where the disagreement between theory and observation is most evident (Navarro 2001). It will take a few more years before N-body simulations achieve the required resolution to accurately determine the central slope of these halos.

2.3.3 Taylor-Navarro Halo Density Profile

As an alternative to direct computation, Taylor & Navarro (2001), exploit the similarity between the phase space density profile of CDM halos (defined as the ratio of density to velocity dispersion cubed, ρ/σ^3, measured in spherical shells) and the self-similar solution for spherical collapse in an expanding universe (Bertschinger 1985). Over more than two decades in radius, the phase-space density profile is well approximated by a power-law of slope $-15/8$.

Density profiles consistent with this result can be obtained by assuming hydrostatic equilibrium (see App. D). The critical solution asymptotically approaches $\alpha = 0.75$ as r tends to 0. Taylor & Navarro (2001) give the following fitting formula for the slope of the "critical" density profile,

$$\beta(x) = \frac{d \ln \rho}{d \ln x} = -\frac{0.75 + 2.625\, x^{1/2}}{1 + 0.5\, x^{1/2}}, \tag{2.46}$$

which is accurate to 3% for $x = r/r_0 < 4$. Here r_0 is the radius where the logarithmic slope of the density profile equals -2.25 and $r_0 = (5/3)r_s$, where r_s is the NFW scale radius. We integrate this slope to obtain the Taylor-Navarro density profile (hereafter TN),

$$\rho(r)_{\rm TN} = \frac{\delta_{\rm c}\, \rho_{\rm crit}}{x^{3/4}(\frac{2}{3} + \frac{\sqrt{x}}{3})^9}. \tag{2.47}$$

2.3.4 Comparison Between Density Profiles

In Figs. 2.5 – 2.7, we show the logarithmic density slopes, density profiles, and rotation curves, respectively, for the ISO, Burkert, $\alpha = 0, 0.5, 0.75, 1.0, 1.5$, and TN halo models. Analytic derivations of the rotation curves for these halos are given in App. E. Recall that $\alpha = 1$ and $\alpha = 1.5$ are the NFW and MOORE profiles respectively. There is very little difference between the rotation curves for the TN and NFW density profiles or between the rotation curves for the $\alpha = 0$ and Burkert density profiles. Thus, for ease of analysis, our models use the ALP density profile parameterization (Eq. 2.40). Fig. (2.8) shows the rotation curves of core (ISO, α=0) and cusp (NFW, MOORE) dominated density profiles for a range of core radii and concentrations. This figure shows the degeneracy between the concentration, c, and the steepness of the central density profile, α: it is possible to produce similar halo rotation curves by increasing α while lowering c.

2.3.5 Oblate/Prolate Density Profiles

Since we expect DM halos to be oblate (§1.3), we generalize the profile further to an axially symmetric ellipsoid by redefining the radius as

$$r^2 = R^2 + z^2/q^2. \tag{2.48}$$

The volume of an ellipsoid defined by fixed R is proportional to the axis ratio q, and we choose to keep the mass within this ellipsoid to be independent of q. Thus we renormalize the density by dividing by q. For arbitrary q and α, the density profile must be integrated numerically, which requires ρ_0 and r_s to be specified. If we parameterize the halo in terms of c and v_{200}, this gives us r_{200} via Eq. (2.38), and r_s via Eq. (2.34). With r_s, we can compute $M(r_{200})/\rho_0$ (which is independent of ρ_0), and then obtain ρ_0 by rearranging Eq. (2.37):

$$\rho_0 = \frac{200\,\rho_{\rm crit}\,\frac{4}{3}\,\pi\,r_{200}^3}{M(r_{200})/\rho_0}. \tag{2.49}$$

We choose this definition so that r_{200} is independent of q. If we were to take into account the reduced volume of a flattened ellipsoid r_{200} would be larger. With ρ_0 and r_s, the density profile is specified and we can compute the circular velocity via Eq. (2.6). As shown in Fig. 2.9, oblate ($q < 1$) halos result in steeper rotation curves, while prolate ($q > 1$) halos result in more slowly rising rotation curves than those from spherical ($q = 1$) halos. However, variations are relatively small ($\sim 10\%$) for reasonable values of q, as is shown in Fig. 2.9.

2.4 Adiabatic Contraction

The main assumption in comparing N-body dark matter profiles to real galaxies is that radiative processes do not alter the density profile of the dark matter. In the hierarchical clustering model, structure forms around peaks of primordial dark matter density fluctuations. The baryonic matter, which can dissipate energy through radiation, cools and falls into the middle of its surrounding dark halo. Blumenthal et al. (1986) give an analytic model for the response of a dissipationless halo to the in-fall of a small dissipational fraction of its mass. This model uses the fact that, for periodic orbits, the action integral

$$\oint p\, dq \tag{2.50}$$

is an adiabatic invariant where p is the conjugate momentum of the coordinate q, (which is not to be confused with the q on the previous page). If the matter distribution is spherically symmetric and particles move on circular orbits, then the adiabatic invariant is simply the angular momentum,

$$L = mvr, \tag{2.51}$$

where m is the mass of the particle, r is the orbital radius and v is the circular velocity:

$$v^2(r) = \frac{GM(r)}{r}. \tag{2.52}$$

Then the adiabatic invariant is

$$r\, M(r) = \text{constant}. \tag{2.53}$$

Expressing this in terms of the baryonic matter and dark matter distributions, M_{B} and M_{DM} respectively, at the initial r_{i} and final r_{f} radii we obtain

$$r_{\mathrm{f}}\, [M_{\mathrm{B}}(r_{\mathrm{f}}) + M_{\mathrm{DM}}(r_{\mathrm{f}})] = r_{\mathrm{i}}[M_{\mathrm{B}}(r_{\mathrm{i}}) + M_{\mathrm{DM}}(r_{\mathrm{i}})]. \tag{2.54}$$

Given the *initial* dark halo distribution $M_{\rm DM}(r_{\rm i})$ (e.g. NFW or ISO), we can obtain the initial baryonic matter distributions $M_{\rm B}(r_{\rm i})$ by assuming the baryons are initially mixed with the dark matter:

$$M_{\rm B}(r_{\rm i}) = \frac{f_{\rm B}}{1 - f_{\rm B}} M_{\rm DM}(r_{\rm i}), \tag{2.55}$$

where the baryon fraction is given by

$$f_{\rm B} \equiv \frac{M_{\rm B}}{M_{\rm B} + M_{\rm DM}}. \tag{2.56}$$

The baryonic mass can be obtained from the observations of stars and gas in the disk, assuming we know the distance of the galaxy, $(M/L)_{\rm disk}$, and assuming that the fraction of baryons in the halo is negligible. The mass of the halo is more problematic, as in all halo models the mass diverges either linearly ($\rho \propto r^{-2}$) or logarithmically ($\rho \propto r^{-3}$). A natural truncation radius (to avoid divergences) is the virial radius of the halo, $r_{\rm vir} \simeq r_{200}$, which is convenient as r_{200} is one of our model parameters and thus does not need to be computed. Substituting this into Eq. (2.54) gives

$$r_{\rm f} \left[M_{\rm B}(r_{\rm f}) + M_{\rm DM}(r_{\rm f}) \right] = r_{\rm i} M_{\rm DM}(r_{\rm i}) \frac{1}{1 - f_{\rm B}}. \tag{2.57}$$

If we further assume that the dark matter particles do not cross orbits, then

$$M_{\rm DM}(r_{\rm f}) = M_{\rm DM}(r_{\rm i}), \tag{2.58}$$

and we can choose a single fixed mass and solve for $r_{\rm f}$ in terms of $r_{\rm i}$:

$$r_{\rm f} = r_{\rm i} \frac{M_{\rm DM}(r_{\rm i})/(1 - f_{\rm b})}{M_{\rm B}(r_{\rm f}) + M_{\rm DM}(r_{\rm i})}. \tag{2.59}$$

This must be solved iteratively, starting with $r_{\rm i} = r_0$ and thus

$$r_{j+1} = r_0 \frac{M_{\rm DM}(r_0)/(1 - f_{\rm B})}{M_{\rm B}(r_j) + M_{\rm DM}(r_0)}. \tag{2.60}$$

Note that the adiabatic approximation is strictly valid only if the initial mass distribution is spherically symmetric, and the orbits of the dark matter are circular and do not cross. These conditions may be violated in realistic situations, though the validity of the adiabatic approximation under such conditions has been confirmed (down to $10^{-2}r_s$) by Jesseit et al. (2002), by studying the response of a dark matter halo to the growth of an exponential disk in high-resolution N-body simulations.

For the adiabatic approximation to hold, the baryon mass fraction must be sufficiently small. A problem that often occurs if the initial halo is too concentrated, (since we assume the baryons are initially mixed with the dark matter), is that the initial baryon distribution can be more concentrated than the final baryon distribution, resulting in an (artificial) expansion of the halo.

In fact, this assumption that the baryons and dark matter start with the same angular momentum distribution (based on the idea that angular momentum from large-scale tidal torques will be similar across the entire halo) has recently come into question. If the baryons have the same angular momentum distribution as the dark matter, this implies that there is too much baryonic material with low angular momentum to form the observed rotationally supported exponential disks (Bullock et al. 2000, van den Bosch et al. 2001a). A key implication of the new picture of angular momentum growth by merging (e.g. Vitvitska et al. 2002) is that the DM and baryons will develop different angular momentum distributions (see Primack 2002).

Nevertheless we still apply the adiabatic contraction formalism of Blumenthal et al. (1986) to our halo models (§5.3), though we remind the reader to interpret the results cautiously. Adiabatic contraction has been widely used in estimating rotation curves in semi-analytical galaxy models (Ryden & Gunn 1987; Ryden 1988, 1991; Flores et al. 1993; Mo, Mao & White 1998), in investigations of the origin of the Tully-Fisher relation (Courteau & Rix 1999), and in analyses of the core structure of dark matter halos (van den Bosch & Swaters 2001; Marchesini et al. 2002; Jimenez et al. 2002).

2.5 Constraints to Mass Models

It can be shown (§5.4) that the combination of an unknown $(M/L)_{\rm disk}$ and at least 2 halo parameters yields families of mass models that are degenerate. Thus any prior constraints we can place on the model parameters will be useful.

2.5.1 Stellar Population Synthesis Models

Stellar Population Synthesis (SPS) models can be used to place constraints on M/L, provided infrared photometry is available (Bell & de Jong 2001). The gradient of M/L vs. colour is fairly independent of the initial mass function (IMF) and star formation (SF) history. It is also smaller in the K-band than in the B-band (Fig. 2.10), though the zero point of the colour M/L relation is itself very sensitive to the IMF (Fig. 2.11). However, constraints can be placed on an assumed IMF by comparing the maximum disk M/L with those from SPS models. The dotted lines in Fig. (2.11) have IMFs chosen to match these constraints. In our future study we will use these models to construct colour corrected disk surface density profiles.

2.5.2 Evidence for Sub-Maximal Disks

More physical means exist for constraining $(M/L)_{\rm disk}$. By combining the equation for the vertical velocity dispersion of an isolated[5] isothermal disk,

$$\left\langle v_z^2 \right\rangle_{R=0}^{1/2} = \sqrt{\pi\, G\, \Sigma_0\, z_0}, \tag{2.61}$$

with the maximum rotational velocity of an exponential disk,

$$v_{\rm disk}^{\rm max} = 0.88\sqrt{\pi\, G\, \Sigma_0\, R_{\rm d}}, \tag{2.62}$$

[5]There is a small correction for a disk embedded in a dark matter halo (Bottema 1993).

we obtain

$$v_{\rm disk}^{\rm max} = 0.88 \left\langle v_z^2 \right\rangle_{R=0}^{1/2} \sqrt{\frac{R_{\rm d}}{z_0}}. \tag{2.63}$$

Thus if we know the velocity dispersion and intrinsic thickness of the disk, we can compute the peak stellar disk velocity and therefore obtain a measure of $(M/L)_{\rm disk}$. Stellar kinematic measurements in 12 spiral galaxies (with $v_{\rm max} > 100\,{\rm km\,s^{-1}}$) by Bottema (1993) have revealed that more massive spirals have larger velocity dispersions, with the correlation,

$$\left\langle v_z^2 \right\rangle_{R=0}^{1/2} = (0.29 \pm 0.10)\, v_{\rm tot}^{\rm max}. \tag{2.64}$$

Substituting this into Eq. (2.63) gives

$$v_{\rm disk}^{\rm max}/v_{\rm tot}^{\rm max} = (0.26 \pm 0.09)\sqrt{\frac{R_{\rm d}}{z_0}}. \tag{2.65}$$

Taking the intrinsic thickness $R_{\rm d}/z_0 = 8.5 \pm 2.9$ (Kregel et al. 2002) yields

$$v_{\rm disk}^{\rm max}/v_{\rm tot}^{\rm max} = 0.54 \pm 0.2 \tag{2.66}$$

at 2.15 disk scale lengths, or equivalently

$$M_{\rm disk}/M_{\rm tot} = 0.30 \pm 0.05. \tag{2.67}$$

Numerical and semi-analytical models of disk formation in a dissipationless DM halo also predict, for realistic universal baryon mass fractions, that dark matter dominates even the inner galactic kinematics (e.g. Dalcanton et al. 1997; Mo, Mao & White 1998). Courteau & Rix (1999) have shown that sub-maximal disks must be invoked to explain the surface brightness independence of the Tully-Fisher relation, and find that, on average, bright galaxies have $v_{\rm disk}^{\rm max}/v_{\rm tot}^{\rm max} \simeq 0.6 \pm 0.1$. Lensing of quasars by individual spiral galaxies (Maller et al. 2000; Trott & Webster 2002) yields $v_{\rm disk}^{\rm max}/v_{\rm tot}^{\rm max} \simeq 0.57 \pm 0.03$.

It is remarkable that the three fully independent techniques reported above, all subject to their own systematic errors, yield nearly the same result,

$$v_{\rm disk}^{\rm max}/v_{\rm tot}^{\rm max} \simeq 0.55, \tag{2.68}$$

for bright galaxies (those with $v_{\max} \geq 100\,\mathrm{km\,s^{-1}}$).

2.5.3 Lensing Constraints on v_{200}

The combined analysis of galaxy-galaxy lensing from the Sloan Digital Sky Survey (SDSS) and the Tully-Fisher relation led Seljak (2002) to postulate that the rotation velocity of early and late-type $\sim L^*$ galaxies decreases significantly from its peak value at the optical radius to the virial radius r_{200}, with

$$v_{\mathrm{tot}}^{\max} / \, v_{\mathrm{tot}}(r_{200}) \simeq 1.8. \tag{2.69}$$

This relation has a 2σ lower limit of 1.4. Combining this constraint with the above evidence for sub-maximal disks, we get the interesting result that the total velocity at the virial radius is approximately equal to the peak velocity of the disk,

$$v_{\mathrm{disk}}^{\max} \simeq v_{\mathrm{tot}}(r_{200}) \simeq v_{\mathrm{halo}}(r_{200}) = v_{200}. \tag{2.70}$$

Applying this constraint reduces the mass modeling exercise to only one free parameter; c, the concentration of the halo. We will use relation (2.70) from lensing and sub-maximal disk analyses to reduce mass modeling of galaxies with $v^{\max} > 100\,\mathrm{km\,s^{-1}}$ to obtain non-degenerate solutions.

2.5.4 Halo Concentration Parameter

Cosmological simulations suggest a correlation between c and v_{200}, such that galaxies with higher v_{200} tend to have lower c. This is because halos with smaller masses collapse earlier, when the Universe has a higher density. Table (2.1) gives the mean concentration with approximate 2σ limits for v_{200} of 50, 100 and 200 $\mathrm{km\,s^{-1}}$. By setting an upper limit on v_{200} of 200 $\mathrm{km\,s^{-1}}$, which is conservative given that the maximum observed velocities of the 6 galaxies we study here are between 67 and 157 $\mathrm{km\,s^{-1}}$, we can place a lower limit on c of 3.

v_{200}	c	-2σ	$+2\sigma$
50	10	4.5	23
100	8.5	4	20
200	7	3	18

Table 2.1: Concentration parameter vs. v_{200}, adapted from Swaters et al. (2002).

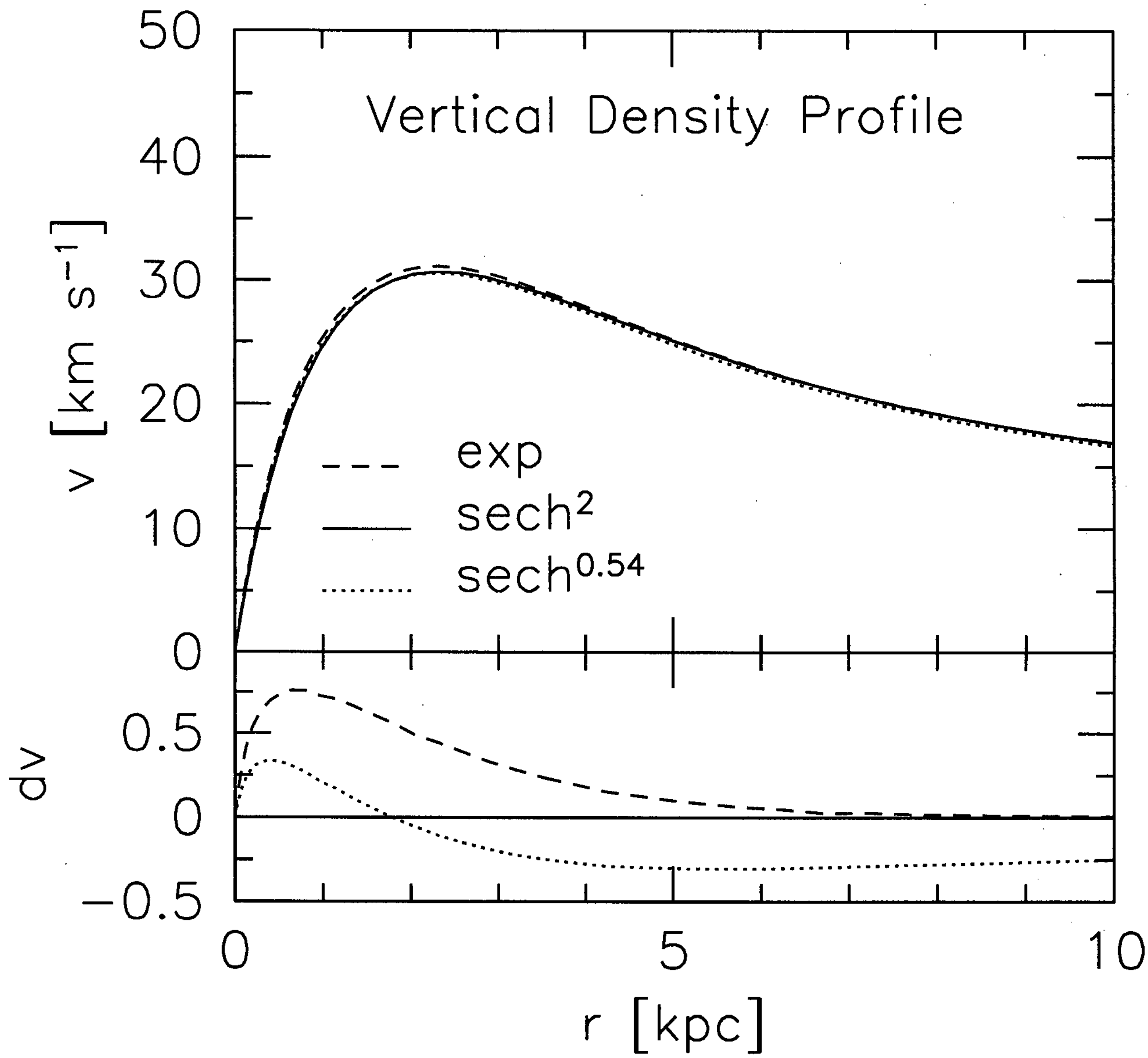

Figure 2.1: Comparison of rotation curves for an exponential disk with exponential (dashed), sech^2 (solid), and sech$^{0.54}$ (dotted) vertical density profiles. All disks have $\Sigma_0 = 100\,\mathrm{M}_\odot\,\mathrm{pc}^{-2}$, and $R_\mathrm{d} = 1\,\mathrm{kpc}$. The lower panel shows the comparison with the sech^2 profile.

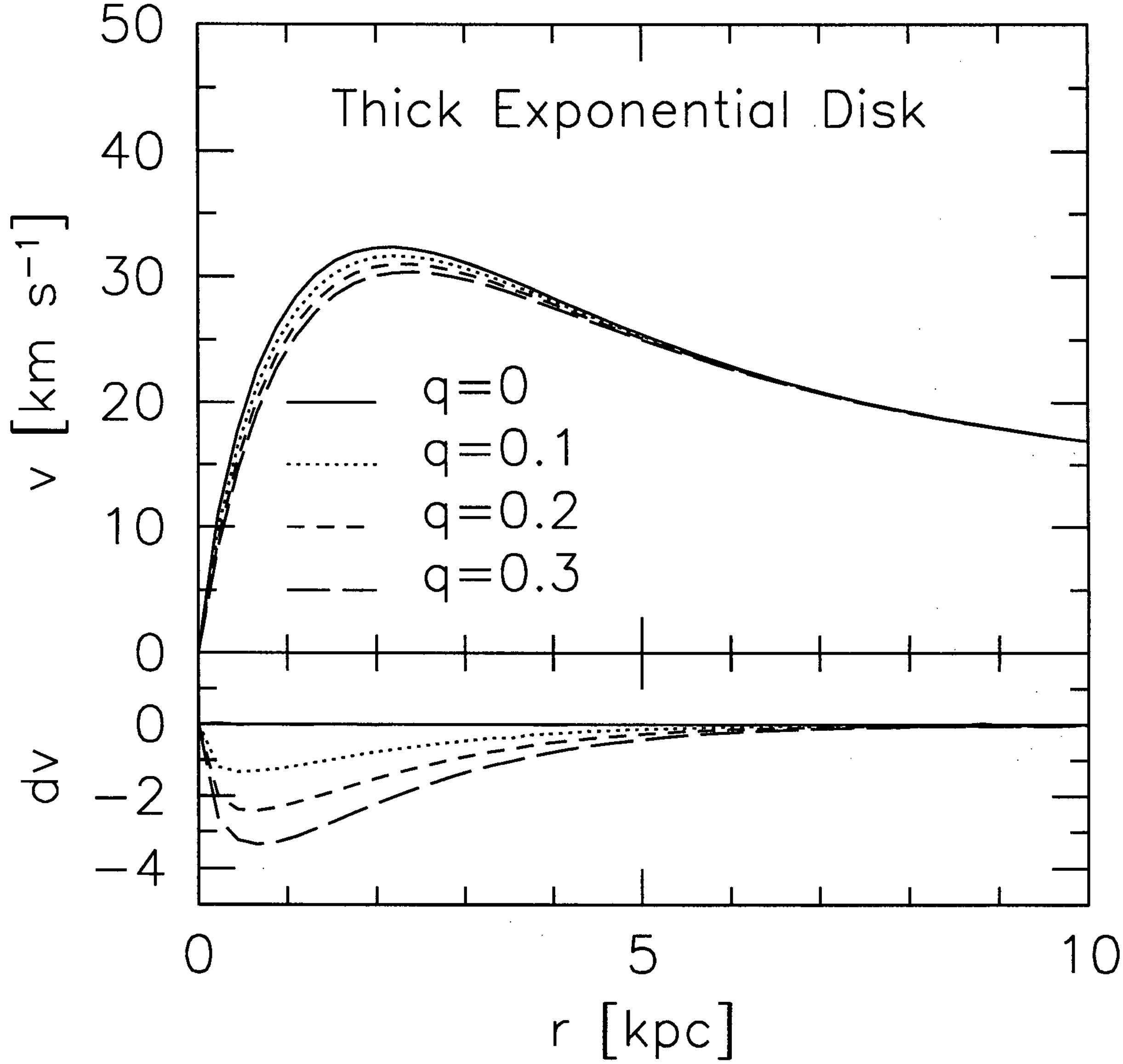

Figure 2.2: Rotation velocity for a thick exponential disk with intrinsic thicknesses $z_0/R_\mathrm{d} = 0$ (solid), 0.1 (long dashed), 0.2 (short dashed), and 0.3 (dotted). All disks have $\Sigma_0 = 100\,\mathrm{M_\odot\,pc^{-2}}$, and $R_\mathrm{d} = 1\,\mathrm{kpc}$. The zero thickness disk is computed using Eqs. (2.3) and (2.19).

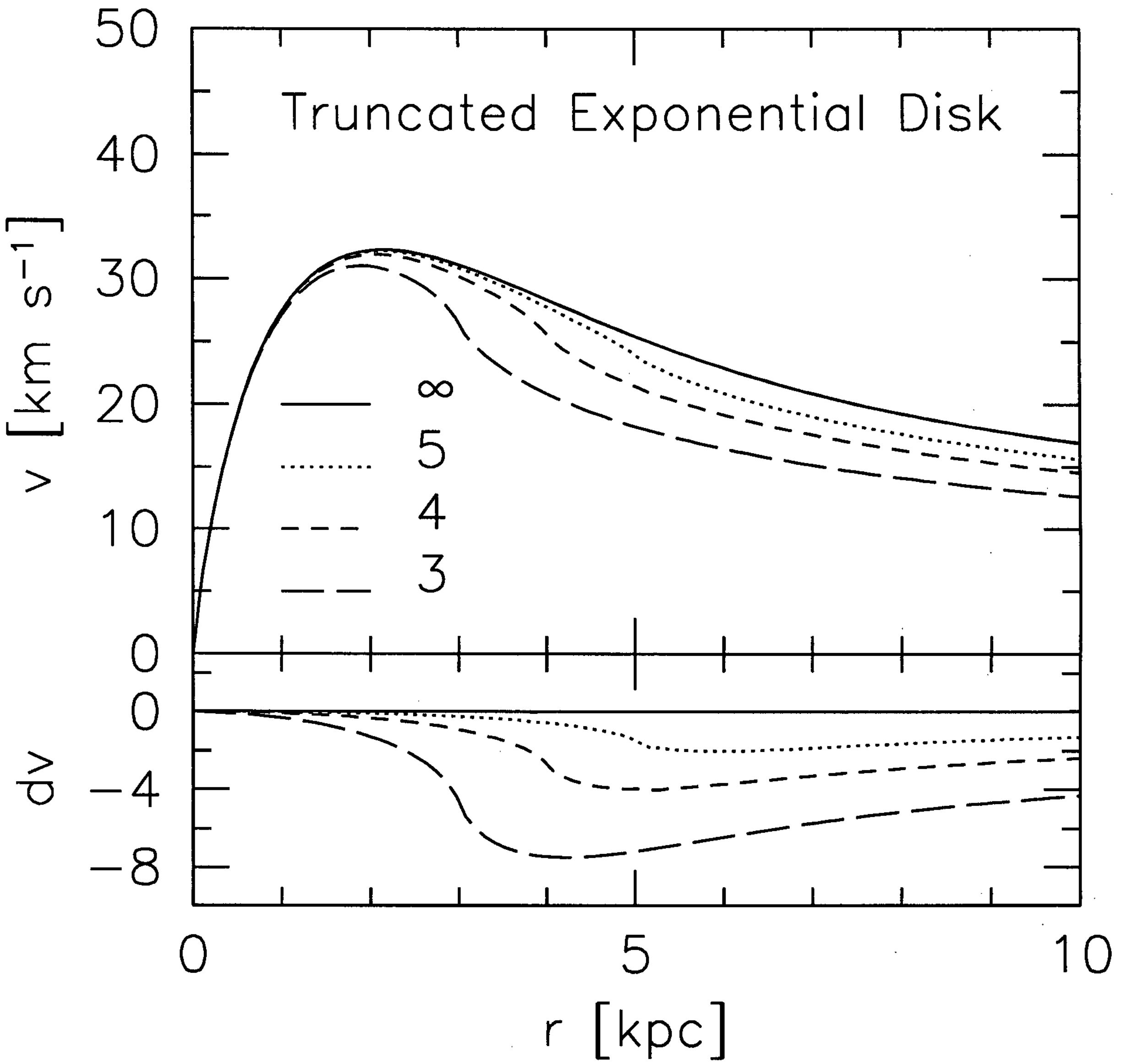

Figure 2.3: Rotation velocity for a truncated exponential disk with $R_{\rm max} = 3$, 4, and $5R_{\rm d}$. All disks have $\Sigma_0 = 100\,{\rm M}_\odot\,{\rm pc}^{-2}$, and $R_{\rm d} = 1\,{\rm kpc}$.

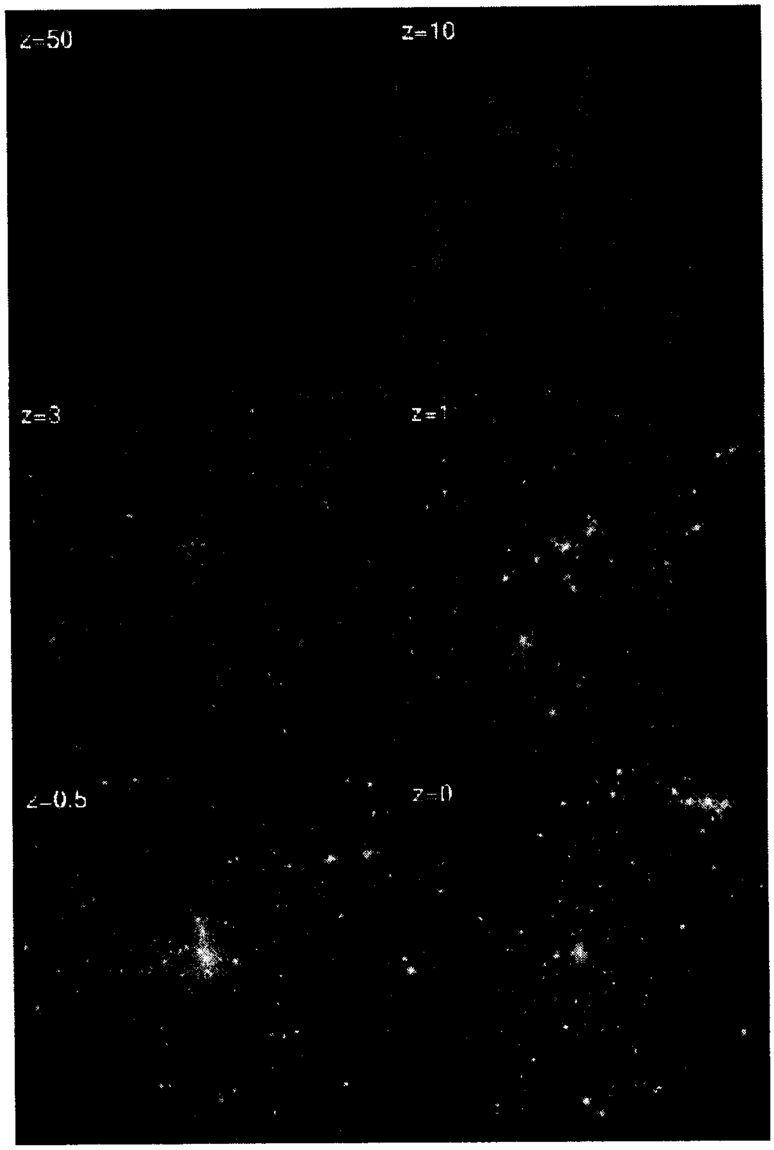

Figure 2.4: The hierarchical evolution of a galaxy cluster in a CDM universe. Small fluctuations in the mass distribution are present but barely visible at early epochs. These grow by gravitational instability, merging and mass accretion, eventually collapsing into virialised quasi-spherical dark matter halos. This plot shows a time sequence of 6 frames of a region of the Universe that evolves into a cluster of galaxies. The local density of dark matter is plotted using a logarithmic grey scale. Linear and non-linear over-densities of a million times the mean background are plotted as black and white, respectively. Each box is 10 Mpc on a side and the final cluster virial radius is 2 Mpc (from Moore 2000).

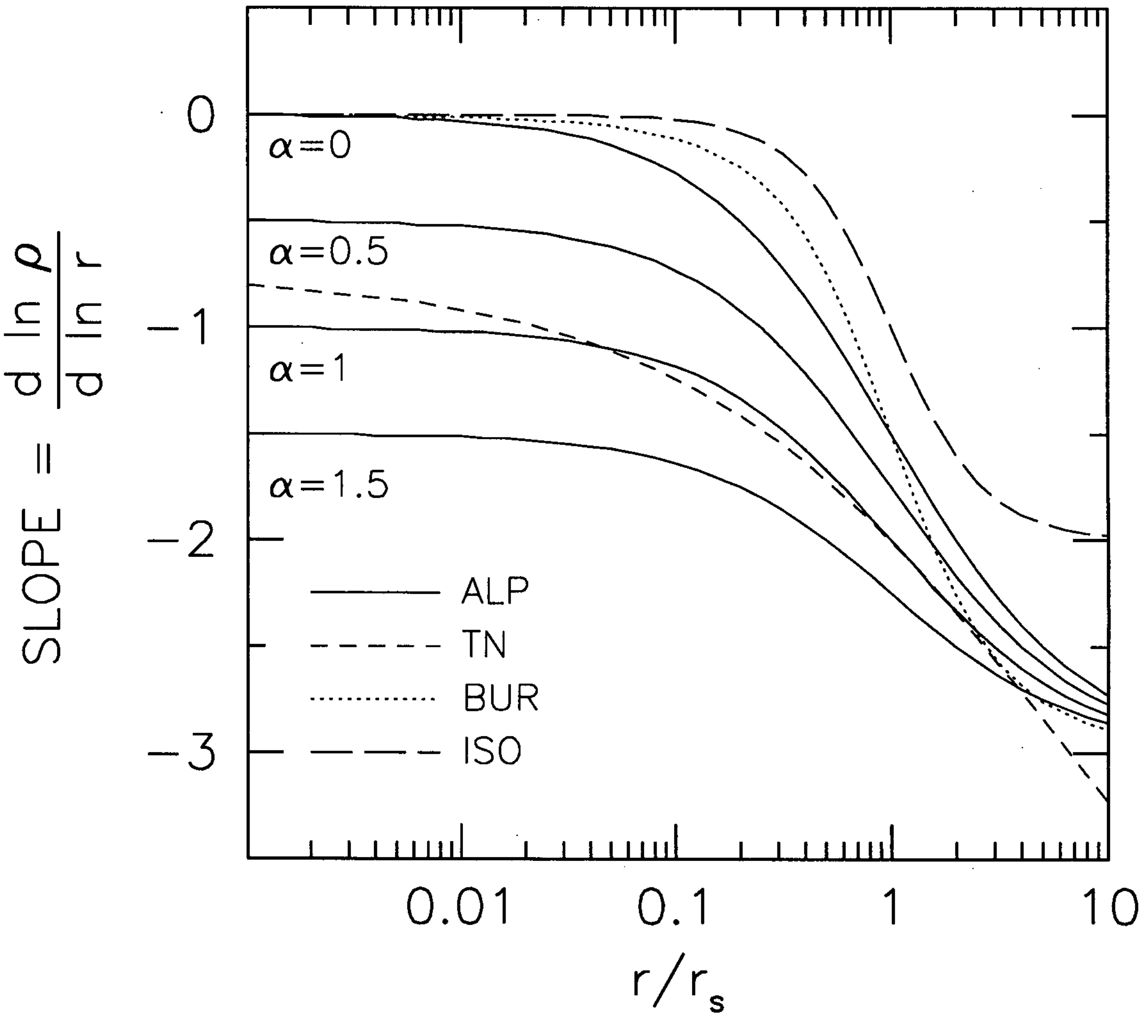

Figure 2.5: Logarithmic slope for dark halo models as a function of radius: α = 0, 0.5, 1.0, 1.5 (solid), TN (short dashed), BUR (dotted), and ISO (long dashed).

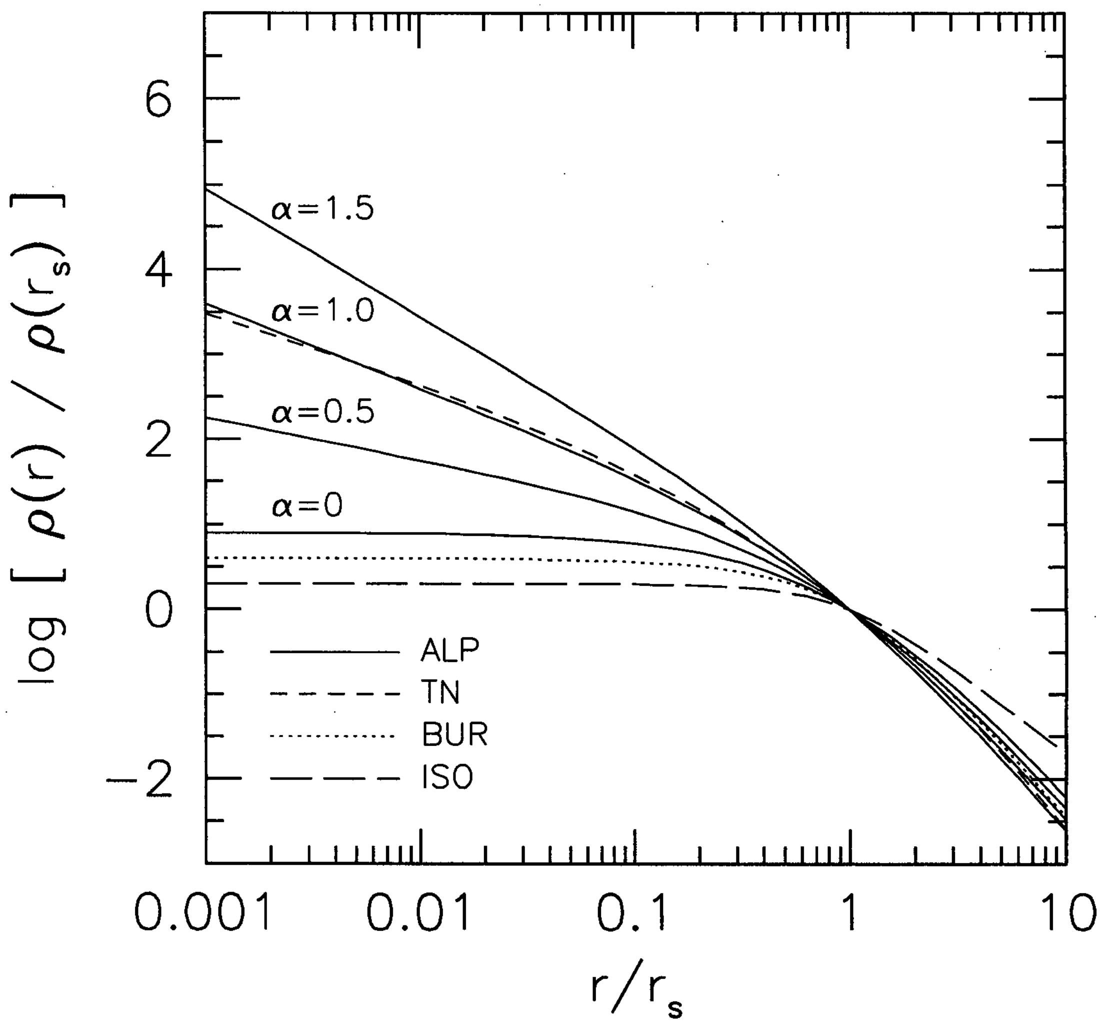

Figure 2.6: Density profiles for the halo models normalized to the density at the scale radius: α = 0, 0.5, 1.0, 1.5 (solid), TN (short dashed), BUR (dotted), and ISO (long dashed).

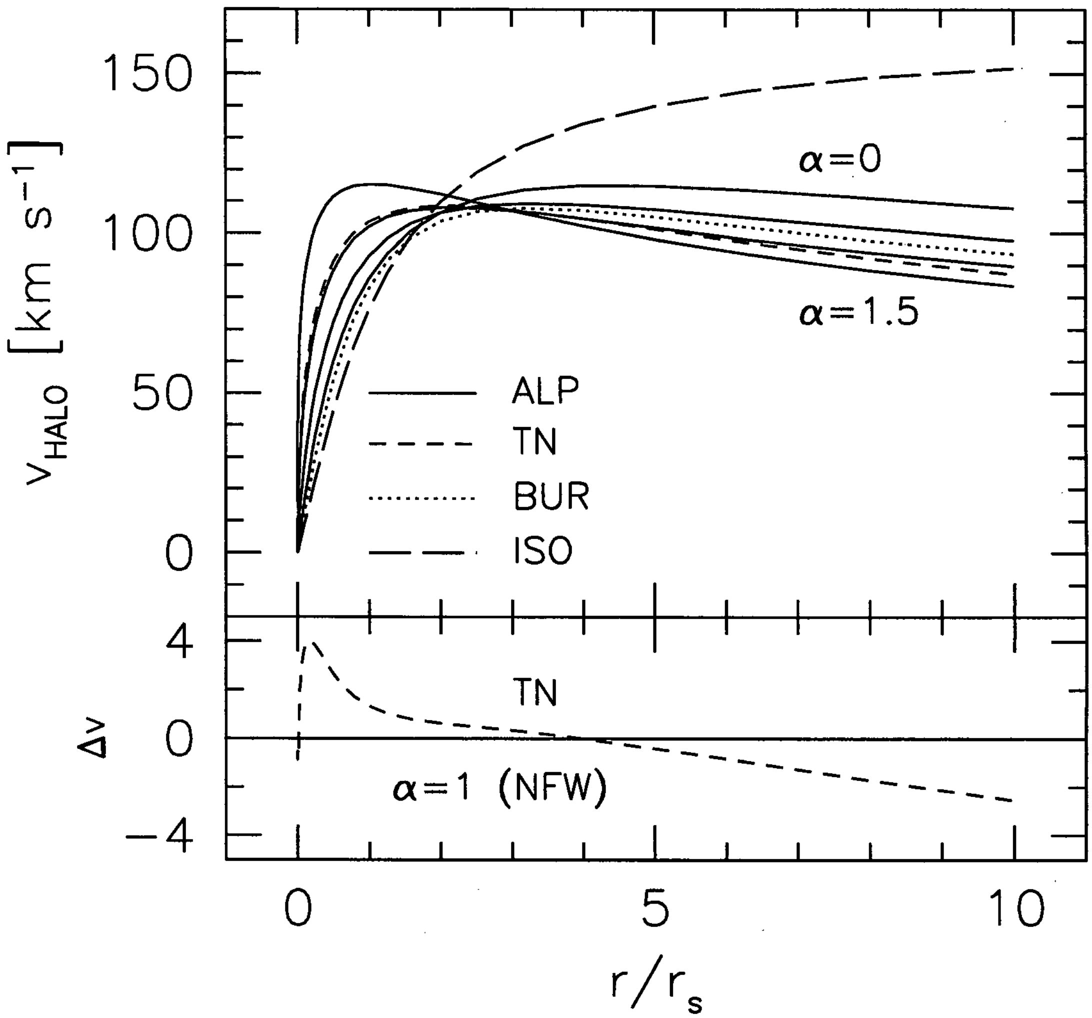

Figure 2.7: Rotation curves for the halo density profiles in Fig. 2.6. The line types are as in Figs. 2.5 – 2.6.

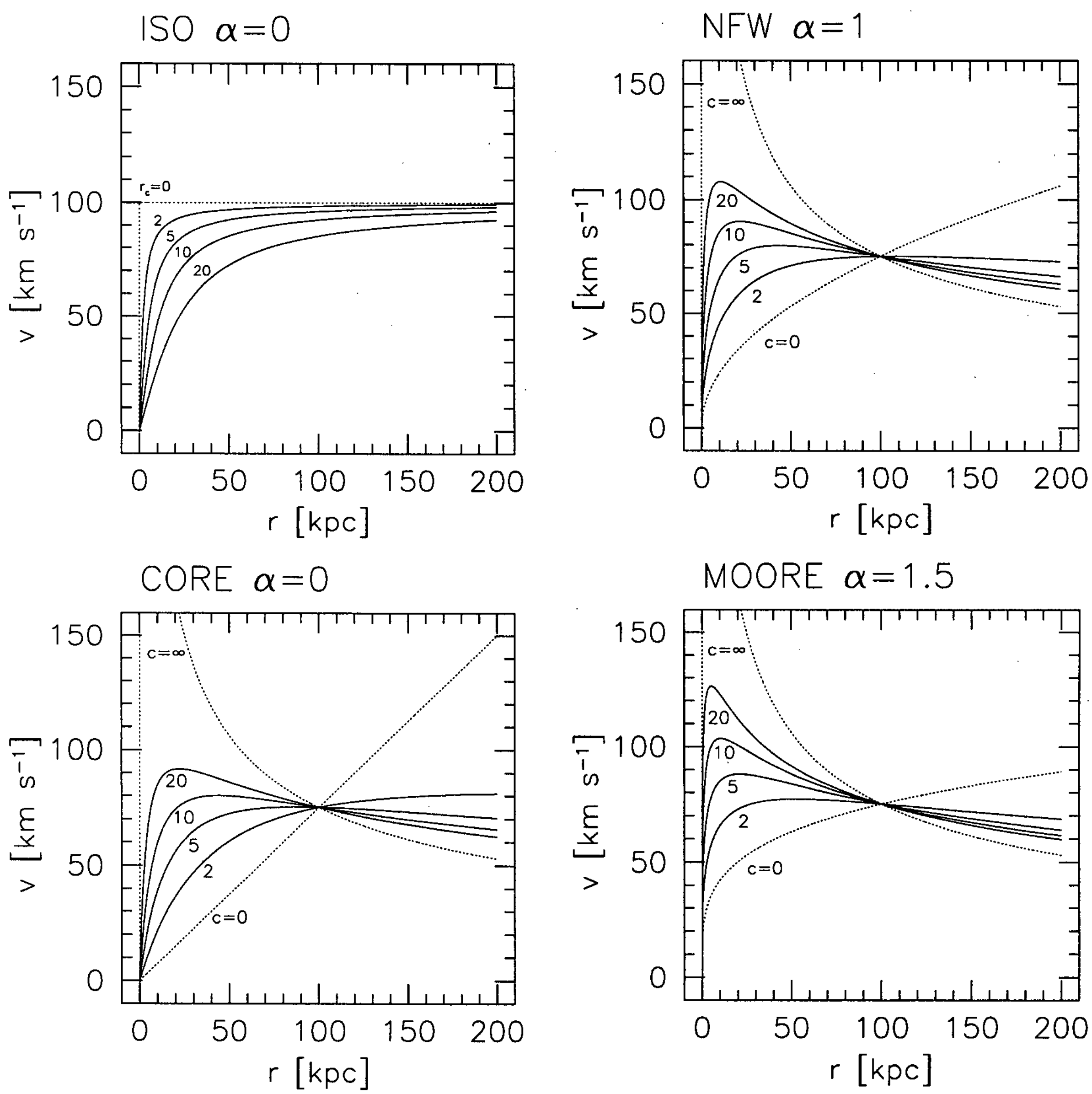

Figure 2.8: Effect of scale parameter on rotation curves of core dominated halos (left) and cusp dominated halos (right), with $v_\infty/r_{200} = 100$. The range of r_c/c is 2, 5, 10, & 20. The dotted lines represent the asymptotic limit of $r_c = 0$ (ISO) and $c = 0, \infty$ (ALP)

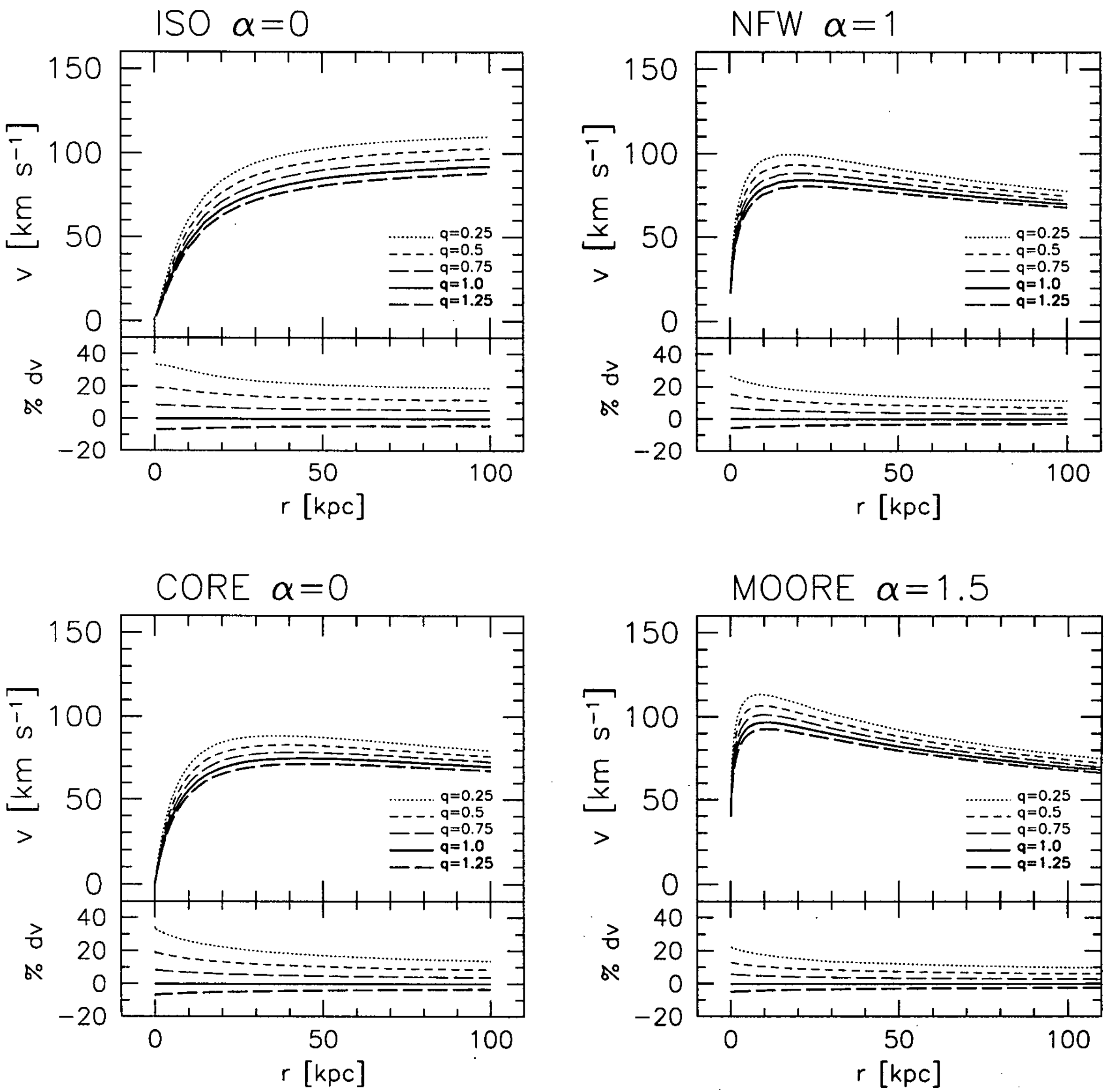

Figure 2.9: Effect of the flattening parameter q on rotation curves of core dominated halos (left) and cusp dominated halos (right). The spherical case $q = 1$ is the thick solid line.

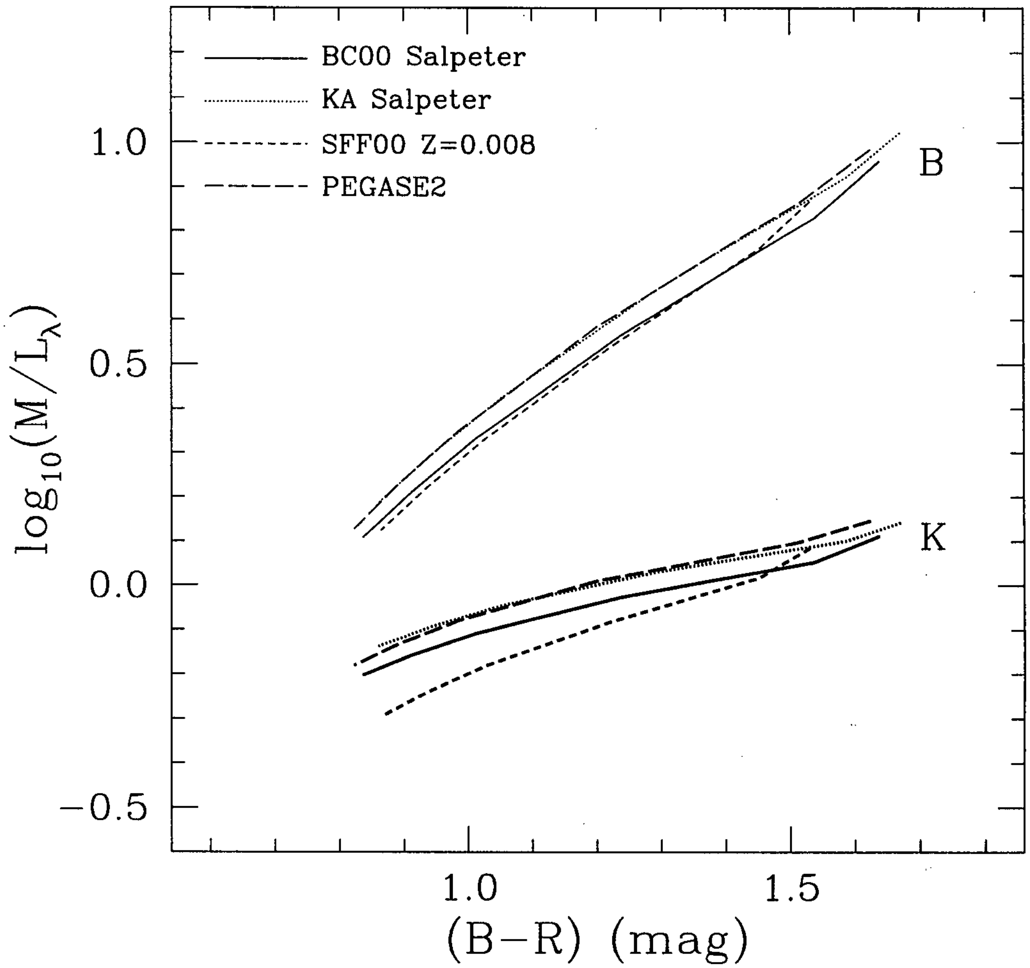

Figure 2.10: Comparison of the colour-M/L relation for a sequence of exponentially declining star formation models of age 12 Gyr using a variety of SPS models. The red ends of the lines represent a short burst of star formation, and the blue end represents a constant star formation rate model. The thin lines are for M/L_{B}, the thicker for M/L_{K}. The different models used are: Bruzual & Charlot (2001, solid), Kodama & Arimoto (1997, dotted), Schulz et al. (2001, dashed) and updated PEGASE models of Fioc & Rocca-Volmerange (2001, long dashed) all with Salpeter IMF. All models have solar metallicity except for the Schulz et al. (2001) models which have 1/3 solar metallicity. (From Bell & de Jong 2001).

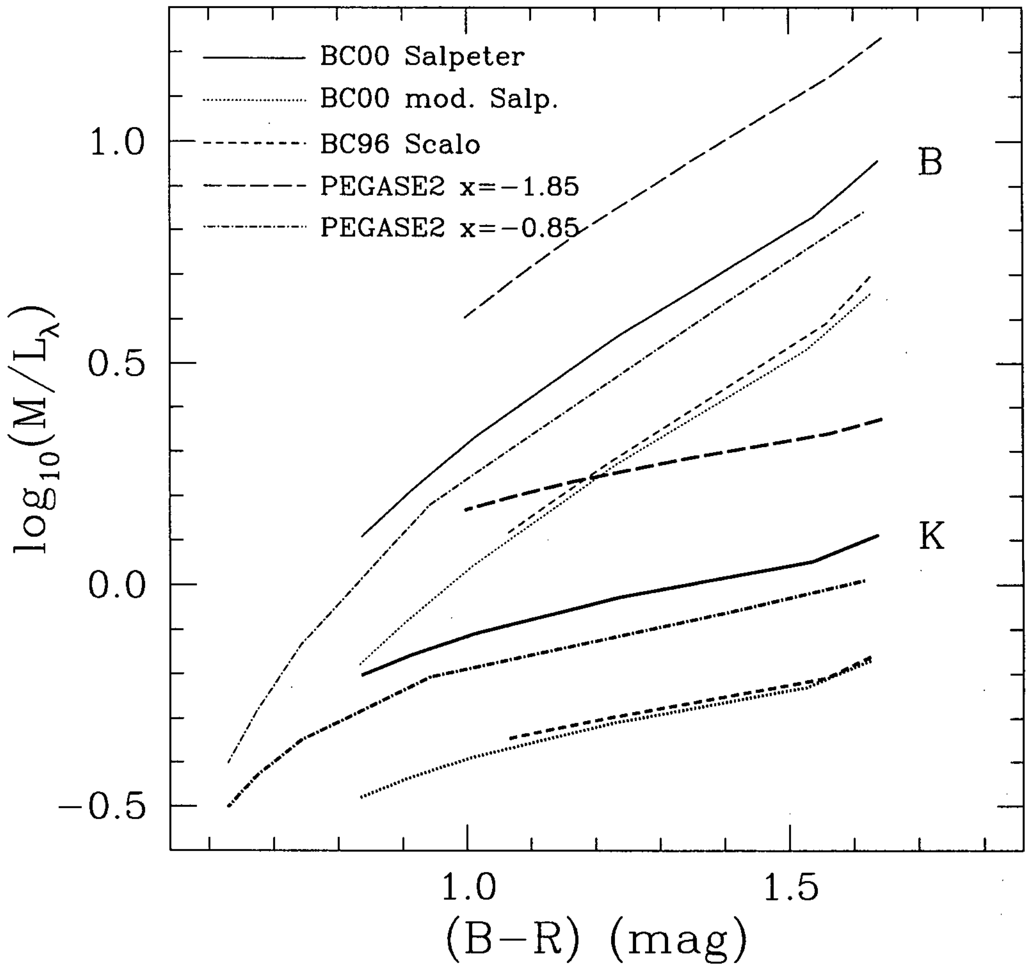

Figure 2.11: Comparison of the colour-M/L relation for a sequence of exponentially declining star formation models of age 12 Gyr using a variety of IMFs. As in Fig 2.10, the thin lines are for M/L_{B}, the thicker lines are for M/L_{K}. The different models and IMFs used are: Bruzual & Charlot (2001) models with a Salpeter $x = -1.35$ IMF (solid), a Salpeter IMF with $x = 0$ for $M < 0.6\mathrm{M}_{\odot}$ (dotted), and Scalo (1986) IMF (dashed); and the updated PEGASE models of Fioc & Rocca-Volmerange (2001) with steeper $x = -1.85$ IMF (long dashed) and a flatter $x = -0.85$ IMF (dot-dashed). All models have solar metallicity. (From Bell & de Jong 2001).

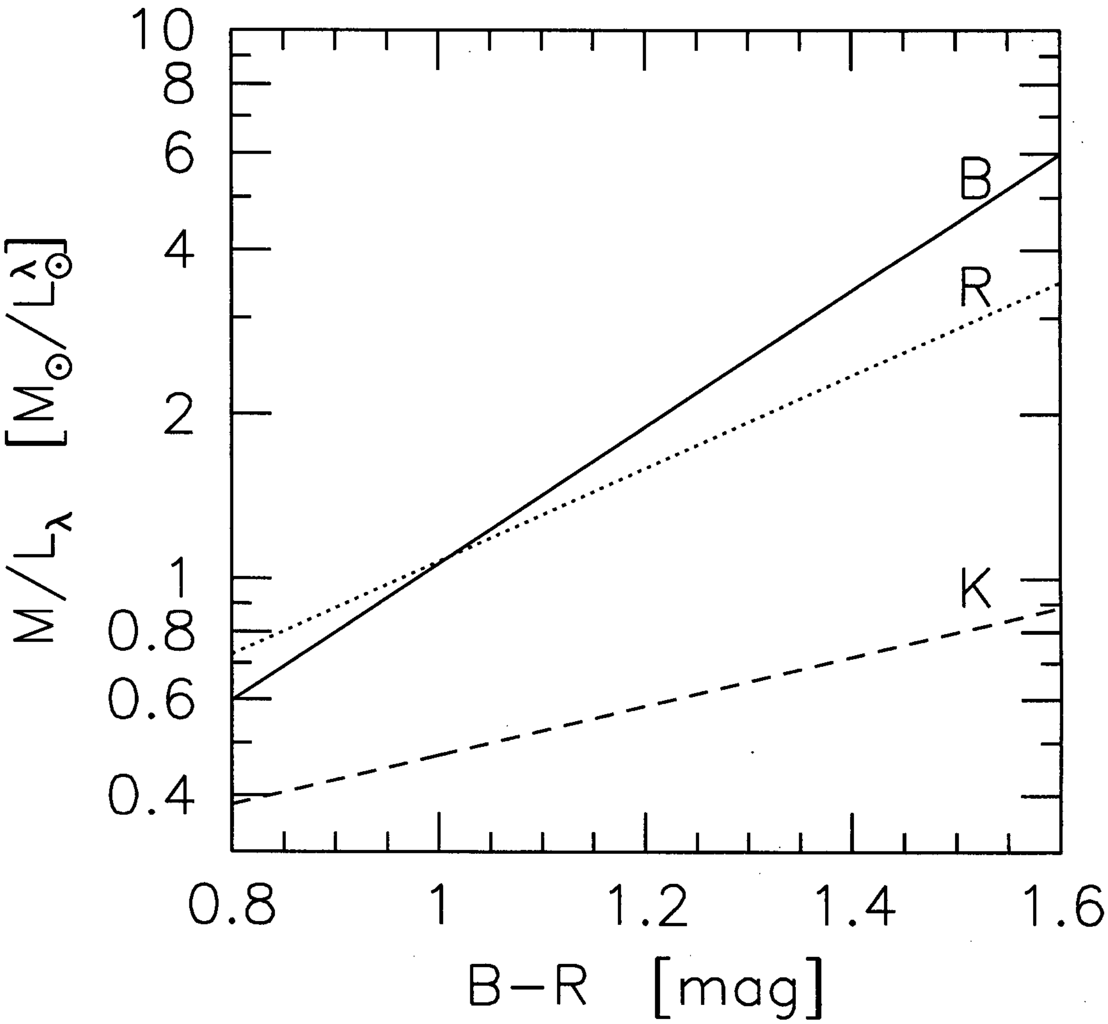

Figure 2.12: Colour$-M/L$ relation for a scaled down Salpeter IMF using $\log_{10}(M/L) = a_\lambda + b_\lambda(B-R)$ with $\lambda : (a,b) = B : (-1.224, 1.251)$,$R : (-0.820, 0.851)$,$K : (-0.776, 0.452)$. (From Bell & de Jong 2001).

Chapter 3

The Data

Before we tackle mass modeling decompositions with the new Hα and optical/infrared photometry of Courteau & de Jong, we first test our models with similar data from Blais-Ouellette (2000). These data consists of HI and Fabry-Perot Hα rotation curves, HI surface density, and B/R-band surface brightness profiles (near-IR photometry is not available for these galaxies). Table 3.1 below gives the optical parameters and references for the 6 galaxies studied here, optical images of the galaxies are shown in Fig. (3.1), and the data are plotted in Figs. (3.2–3.4).

3.1 Rotation Curves

The observed rotation curve $v(R)$ as a function of radius R from the centre of a galaxy is the projection of the galaxy's velocity field in the plane of the sky. The observed velocity can be separated into systemic, $v_\odot$, rotational, $v_{\rm rot}$, and expansive, $v_{\rm exp}$, components as follows:

$$v(x,y) = v_\odot + v_{\rm rot}(R)\,\sin(i)\,\cos(\theta) + v_{\rm exp}(R)\,\sin(i)\,\sin(\theta), \tag{3.1}$$

where (R,θ) are polar coordinates measured in the plane of the galaxy, and are related to the coordinates on the plane of the sky by

$$\cos(\theta) = \frac{-(x-x_0)\,\sin(\phi_0) + (y-y_0)\,\cos(\phi_0)}{R}, \tag{3.2}$$

$$\sin(\theta) = \frac{-(x-x_0)\,\cos(\phi_0) - (y-y_0)\,\sin(\phi_0)}{R\,\cos(i)}, \tag{3.3}$$

where ϕ_0 is the position angle of the major axis of the receding side, $v > v_\odot$, of the galaxy major axis, measured counter-clockwise from the North.

If the radial velocity field is fully sampled (e.g. for HI or Fabry-Perot interferometers or integral field spectrographs, IFS), the rotation curve can be derived from the velocity field by fitting a tilted-ring model (Begeman 1989). This assumes the velocity field can be described by a set of concentric rings. For circular orbits $v_{\rm exp} = 0$, and there are 6 free parameters for each ring:

- The sky coordinates, (x_0, y_0), of the rotation centre of the galaxy;
- The systemic velocity, $v_\odot$, of the centre of the galaxy with respect to the Sun;
- The circular velocity, $v_{\rm rot}$, at distance R from the galaxy centre;
- The inclination angle, i, between the normal to the plane of the galaxy and the line-of-sight, where 90° corresponds to edge-on, while 0° is face-on;
- The position angle, ϕ_0, of the receding side of the galaxy.

The tilted-ring fit has 6 free parameters per ring, which makes finding a unique solution difficult. In practice one first determines $v_\odot$, x_0, and y_0, for each ring, as these parameters should be the same for all rings. When the residual velocity field shows no systematic effects, the best estimates for $v_\odot$, x_0 and y_0 are obtained by taking the mean over all rings. An estimate of the uncertainty in these is obtained by dividing the standard deviation from the mean by the square root of the number of rings. Next the parameters $v_{\rm rot}$, i, and ϕ_0 are fitted for the receding and approaching sides of the galaxy separately, which provides a check on the symmetry of the velocity field.

For long-slit observations, only the major axis of the velocity field is sampled, $\cos(\theta) = 1$, and the derivation of a rotation curve is greatly simplified. Once $v_{\rm rot}(R)$ has been determined, the remaining parameters are i, and $v_{\odot}$. The inclination can be measured from photometry, but this can be hard to estimate for dwarf and LSB galaxies. Moreover, kinematic and photometric inclinations often differ by many degrees (e.g. Courteau et al. 2003), and it is thus safer to use values obtained from the HI kinematics, if available.

3.2 Systematic Rotation Curve Errors

Various sources of observational error contribute to underestimating the amplitude of rotation curves and hence the inner density slope of disk galaxies. The most significant are: resolution, slit-position error, and extinction from dust.

For radio data, beam smearing is significant due to the relatively low angular resolution ($15'' - 50''$) of typical 21cm spectral maps. Hα observations usually achieve much higher resolution and beam smearing is no longer a critical issue. However, most Hα rotation curves are obtained by placing a long slit across the major axis of the galaxy, and misplacement of the slit either by missing the kinematical centre, which is not always the photometric centre, or having the wrong position angle, will lead to an underestimation of the rotation velocities. The presence of a bar or non-circular motions due to spiral arms or other substructure is hard if not impossible to detect from 1D sampling of the velocity field. Many of these uncertainties can be reduced by observing 2-D velocity fields (e.g. Courteau et al. 2003). In optical bands this can be achieved with Fabry-Perot interferometers or integral field spectrographs.

Extinction from dust can also be an issue for optical rotation curves, especially with moderately inclined galaxies, where extinction effects are more severe. Surprisingly, a comparison of the Hα rotation curve with that obtained from CO interferometry, which is unaffected by extinction, yields excellent agreement for the dwarf galaxy NGC 4605, which has an inclination of $\simeq 68°$ (Bolatto et al. 2002). Courteau & Faber (1988) showed that extinction effects are most conspicuous at $i > 82°$. The 6 galaxies considered in this study have inclinations in the range $40° < i < 80°$ and we tentatively conclude that dust effects are only be minimal. Nonetheless, confirmation with our K-Band data will be instrumental to address this issue conclusively.

To date, no convention on how to represent the errors on rotation curves exists in the literature (e.g. random vs. systematic). Error bars are often simply given as the velocity dispersion in the ring (2D) or velocity channel (1D) at each radius. However, the hot HII gas is more sensitive to its environment than the cold HI gas. Its dispersion is increased by turbulence, local density variations, and winds from stars and supernovae of the young stellar forming regions in which the ionized gas is found. Having only a few data points (as in long-slit observations) can thus artificially bias the dispersion low and error bars are therefore underestimated. Another estimate of the uncertainties on the measured potential, based on the assumption of symmetry, uses the velocity difference between the approaching and receding sides of the galaxy, weighted by the number of points on each side.

However, both these methods can give unrealistically small errors ($< 1\,\mathrm{km\,s^{-1}}$), e.g. in the case of high signal-to-noise data for bright HII regions, or if the two sides of the rotation curve have cross-over points. Another problem one must be aware of, especially for HI rotation curves, is the correlation of radial velocities recorded in adjacent channels, i.e. for separations less than beam size of the telescope. Because the number of sampling points is larger than the number of independent beams this will result in an underestimate of the formal errors in the parameters. Such small error bars can easily dominate any model minimization and would severely bias χ^2 values. To prevent this we place minimum error bars on the rotation curve as discussed in §5.2. We will discuss the definition of rigourous error bars in our next investigation, based on Steward Observatory data.

3.2.1 Comparison between Hα and HI Rotation Curves

We now look at a comparison between observed optical and radio rotation curves (RCs) in Fig. (3.2). Agreement between Hα and HI rotation curves is usually excellent, though the Hα data points show more scatter (the HI data have been (Hanning) smoothed). We now discuss the data quality for each galaxy in turn:

- IC 2574 is quite disrupted and has a patchy Hα velocity field, making a determination of a reliable rotation curve with an iterative method (based on velocity dispersion in annuli) impossible. The HI RC is asymmetric in places, leading to large error bars on a few data points. The RC is still rising at the last measured data point.

- NGC 3109 is close enough ($D = 1.36$ Mpc) that its HI RC is well sampled. The addition of Hα data confirms the negligible effect of beam smearing. The HI RC is still rising at the last measured data point.

- UGC 2259 has a poorly resolved HI RC with only 8 data points, starting at ~ 1 kpc. The Hα data provide 6 additional points interior to 1 kpc. Note some discrepancy between the last few Hα and HI data points around 3 kpc. The HI RC still rises slowly at the last measured data point.

- NGC 5585 has a moderate resolution HI RC that agrees broadly with the Hα data. The HI RC levels off at large radii.

- NGC 2403 has a steeply rising RC which is best sampled at Hα. The Hα RC shows signs of spiral structure (large amplitude wiggles) and large scatter in the last few data points. The HI RC is flat at large radii.

- NGC 3198 has a steeply rising RC which is best sampled at Hα. There is a lot of scatter in the inner Hα RC because the two sides were not folded and averaged. The HI RC is flat at large radii.

3.3 Photometry

There are two major sources of uncertainty in converting observed surface brightness profiles into luminosity profiles in the plane of the galaxy: inclination and extinction effects. Let us briefly review the effects of dust on the surface brightness, which is defined as the magnitude per solid angle, Ω, on the sky:

$$\mu = m + 2.5\ \log(\Omega). \tag{3.4}$$

Expressing this in terms of luminosity and area,

$$\mu = -2.5\ \log(L) + 2.5\ \log(A) + \text{const.} \tag{3.5}$$

Assuming the disk is optically thin, if the disk has zero thickness, then an observed unit area will be a factor of $b/a = \cos(i)$ smaller than the unit area in the plane of the galaxy. Here, a and b are the major and minor axes in the plane of the sky, and i is the inclination angle. Thus the intensity (luminosity per unit area) in the plane of the sky will be higher by a factor of a/b than the face-on case. For an inclination of 60°, this difference would be a factor 2! In magnitude units, the observed surface brightness will be $2.5\log(b/a)$ greater than the face-on surface brightness. Since b/a is less than 1, the observed surface brightness increases with inclination, as

$$\mu_{\text{obs}} = \mu_{\text{gal}} + 2.5\ \log(b/a). \tag{3.6}$$

In the case of a thick disk the observed radial profile will be modified as a line of sight through the galaxy intercepts light from different radii. This effect will increase with inclination, and with disks of larger intrinsic thickness.

If there is dust, some of the light will be scattered or absorbed, resulting in less transmitted light and a redder color. If we define the ratio of observed to emitted luminosity to be C, so that $C = 0$ and 1 for the optically thick and thin cases respectively, then the observed intensity will be

$$I_{\rm obs} = C\, I_{\rm gal}, \tag{3.7}$$

where $I_{\rm gal}$ is the face-on intensity. Expressing this in surface brightness:

$$\mu_{\rm obs} = \mu_{\rm gal} - 2.5\ \log(C). \tag{3.8}$$

For the case of an optically thick screen of dust in the $z = 0$ plane, only half of the galaxy light would be seen, and the galaxy would appear 0.75 mag arcsec^{-2} fainter.

The effect of extinction from dust is hard if not impossible to model accurately. If dust affects light uniformly across the galaxy, then $(M/L)_{\rm disk}$ can just be scaled, but it also loses its physical meaning and SPS constraints are no longer applicable. However, in the more realistic scenario that extinction is not uniform, using a constant $(M/L)_{\rm disk}$ may result in an incorrect stellar mass and hence stellar velocity profile. Inclination and extinction by dust have opposite effects on the surface brightness profile (the former leads to an under-estimate of the M/L ratio, while the latter causes an over-estimate) though due to the uncertainties in modeling these effects we leave our surface brightness profiles uncorrected. Thus the advantage of using K-band observations over optical band passes to model the disk cannot be overemphasized.

3.4 Galaxy Distances

In order to compute the relative contribution of the stars and gas to the rotation curve we need to know the distance to the galaxy. The contribution of the stars can always be scaled with $(M/L)_{\rm disk}$, but the contribution from the gas is fixed. The mass of gas is proportional to the square of the distance to the galaxy, $M_{\rm gas}(R) \propto D^2$, and since the rotational support of each mass component at a given radius is proportional to the mass of that component within that radius, $v^2(R) \propto M(R)$, it follows that $v^2_{\rm gas}(R) \propto D^2$. Thus, if the distance of the galaxy under estimated by 30%, the rotational support of the gas will be underestimated by a factor of 2. Following Swaters (1999), we use distance indicators in the following order of preference: Cepheids, brightest stars, and Hubble flow (via redshifts). In Table (3.1), we give our adopted distance, the adopted distance from Blais-Ouellette (2000) and the heliocentric distance based on $H_0 = 75\,{\rm km\,s^{-1}\,Mpc^{-1}}$. The latter method is not especially reliable as these galaxies have heliocentric velocities, $v_\odot < 700\,{\rm km\,s^{-1}}$ and peculiar motions due to the Local Supercluster can be several hundred ${\rm km\,s^{-1}}$. Some of our adopted distances are different than those of Blais-Ouellette (2000) and we show the effect this has on the fit parameters in §5.2.

Galaxy	(Notes)	IC 2574	NGC 3109	UGC 2259	NGC 5585	NGC 2403	NGC 3198
Type	(RC3)	SAB (s) m	SB (s) m	SB (s) cd	SB (rs) c	SAB (s) cd	SB (rs) c
R.A.	(J2000)	$10^h28^m21^s.2$	$10^h03^m06^s.6$	$02^h47^m55^s.4$	$14^h19^m48^s.2$	$07^h36^m51^s.4$	$10^h19^m54^s.9$
Dec.	(J2000)	$68°24'43''$	$-26°09'32''$	$37°32'18''$	$56°43'46''$	$65°36'09''$	$45°32'59''$
i	(1)	$77° \pm 3°$	$80° \pm 2°$	$41° \pm 3°$	$53° \pm 1°$	$60°.2 \pm 1°.6$	$72°.3 \pm 1°.8$
PA	(1)	$41° \pm 6°$	$91°.5 \pm 1°$	$160° \pm 1°$	$40° \pm 1°$	$122°.5 \pm 1°.4$	$216°$
$v_{\max}$	(1)	67	67	90	92	136	157
$v_{\odot}$	(1)	57	403	583	305	131	663
D_{H_0}	h_{75}	0.76	5.4	7.8	4.1	1.7	8.8
$D_{\mathrm{B-0}}$	(2)	3.0	1.36	9.6	6.2	3.2	9.2
D_{AAD}	(3)	3.7^{b}	1.36^{c}	9.6^{h}	8.7^{b}	3.22^{c}	13.8^{c}
scale	[kpc/′]	1.07	0.395	2.79	2.53	0.936	4.01
M_{B}	(2)	-16.77	-16.35	-17.03	-17.50	-19.50	-19.90
μ_0^{B}	(4)	22.95	21.98	21.30	20.04		
μ_0^{R}	(4)	21.67		20.14	19.79	20.27	19.91
R_{d}	[kpc]	2.20	1.31	0.81	1.57	2.05	3.44
D_{25}	[′]	9.8	14.4	2.6	5.3	21.9	8.4
R_{HO}	[′]	8.6	13.3	1.9	3.6	13.0	11.9
Refs.	(5)	(B,M,M)	(B,J,J)	(B,C,K)	(B,O,O)	(B,G,K)	(I,G,K)

Table 3.1: Galaxy parameters

Notes:

1: From tilted-ring fit to HI radial velocity field, see HI reference.

2: Taken from Blais-Ouellette (2000).

3: Distance indicator: c: Cepheid; b: brightest stars; h: h_{75} corrected for Virgo-centric flow.

4: From fit to surface brightness profile, with a marked disk. Uncorrected for inclination and extinction.

5: (Hα, HI , Photom.) B: Blais-Ouellette (2000); C: Carignan et al.(1988); G: Begeman (1987); I: Corradi et al. (1991); J: Jobin et al. (1990); K: Kent (1987); M: Martimbeau et al. (1994); O: Côté et al. (1991).

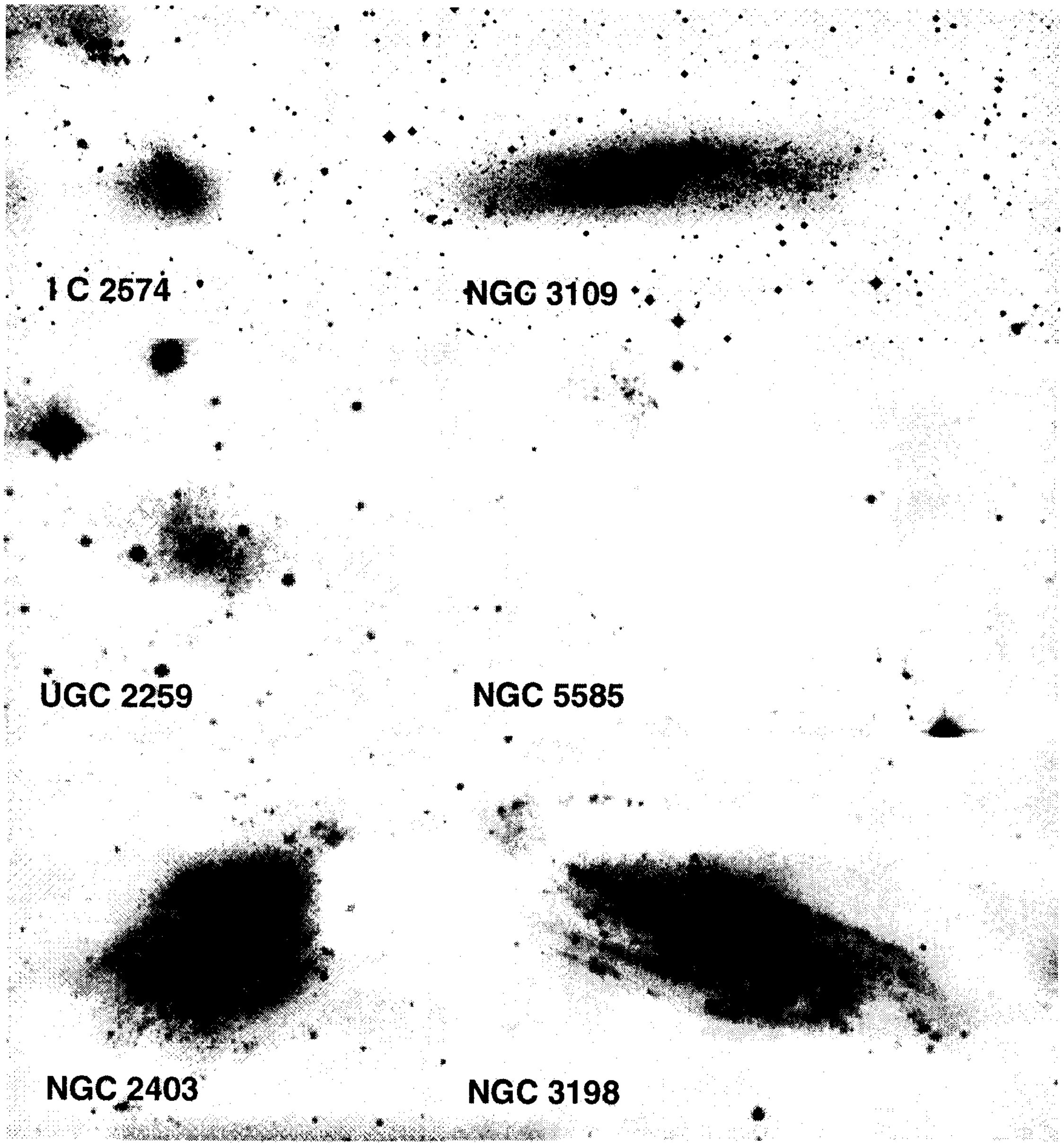

Figure 3.1: Optical images of the 6 galaxies studied here, taken from the NASA/IPAC Extragalaxtic Database: http://nedwww.ipac.caltech.edu/.

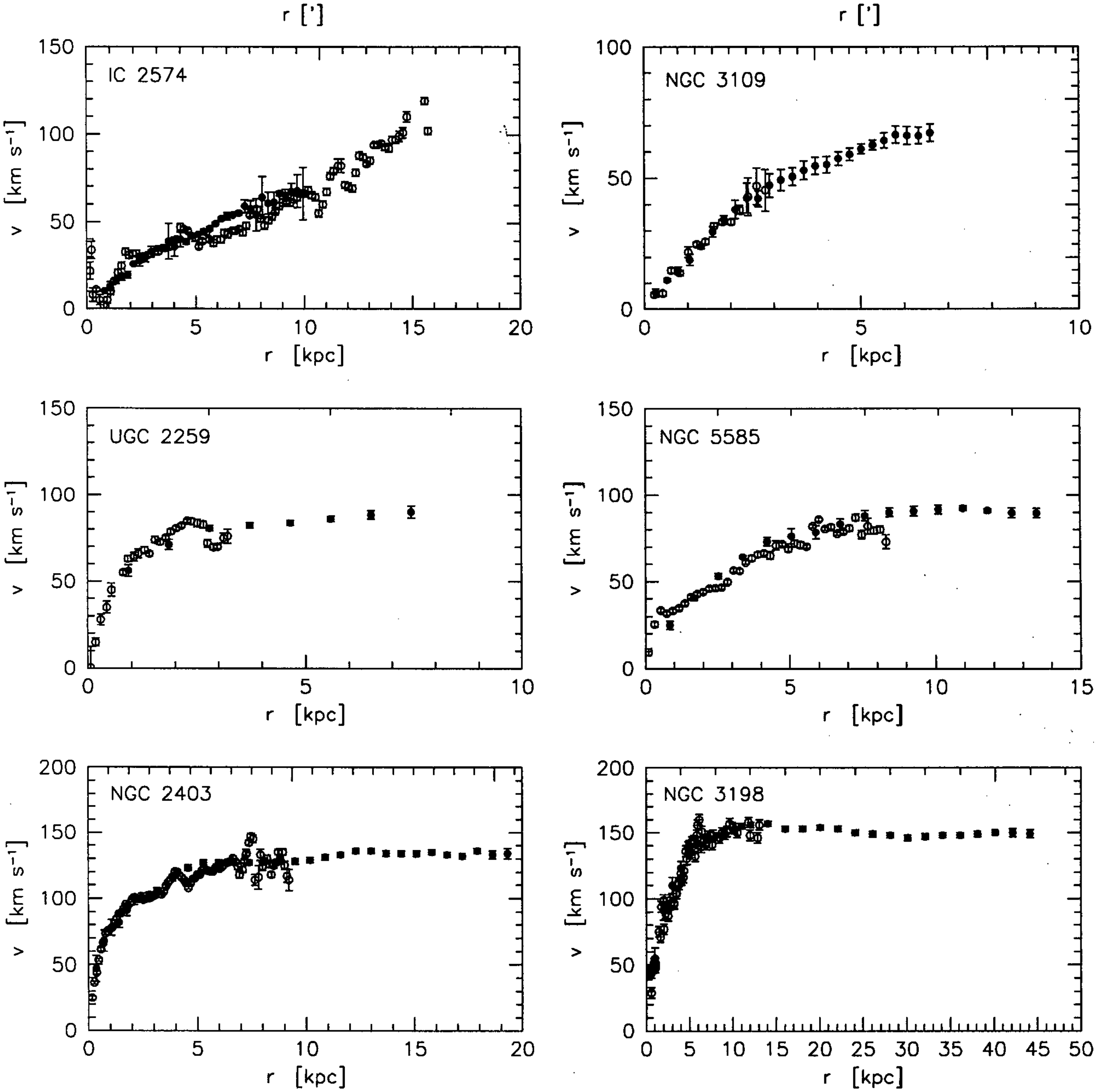

Figure 3.2: Rotation curves from HI (solid circles) and Hα (open circles) data plotted against radius in kpc (lower axes) and arcminutes (upper axes, tick marks at $1'$ intervals). See Table 3.1 for references.

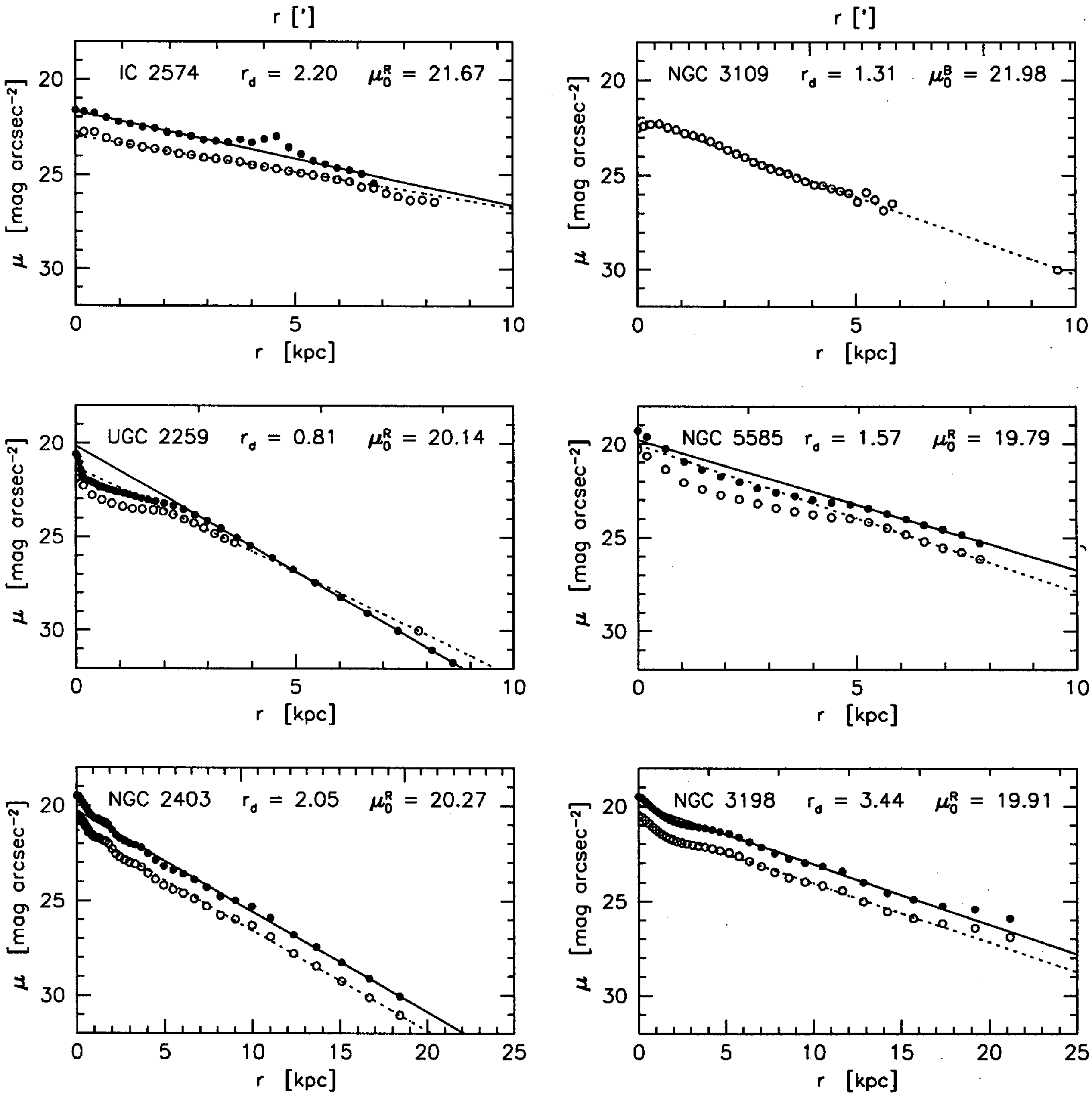

Figure 3.3: Surface brightness profiles in R-band (filled circles) and B-band (open circles) plotted against radius in kpc (lower axes) and arcminutes (upper axes, tick marks at 1′ intervals), with exponential fits to the disk in R-band (solid line) and B-band (dashed line). Note that most of the disks have been extrapolated and the last reliable measured data points are at $\mu^{B} \simeq 26$. See Table 3.1 for references, error bars are not available.

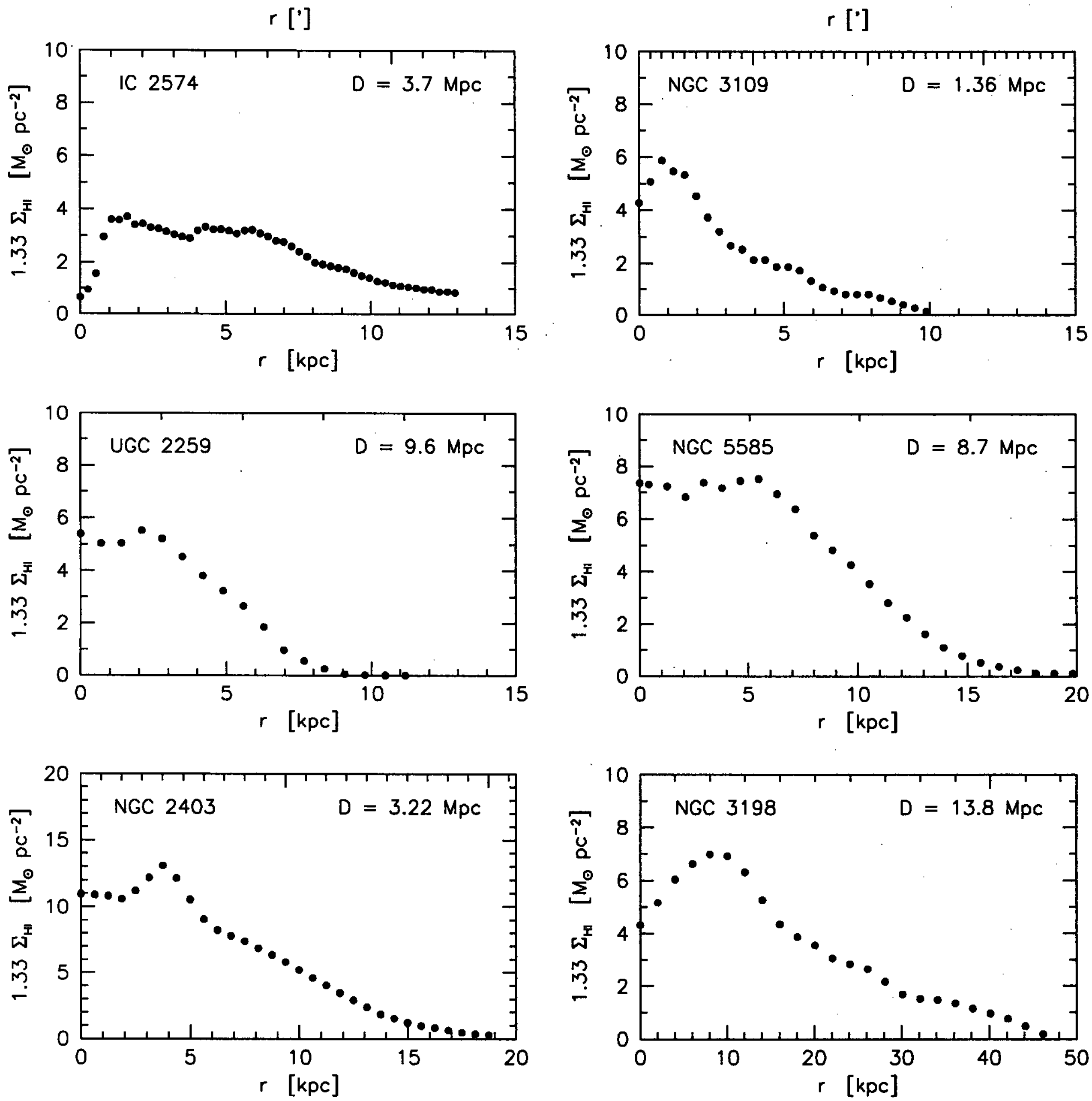

Figure 3.4: HI surface density in $M_\odot\,pc^{-2}$, multiplied by 1.33 to account for He, plotted against radius in kpc (lower axes) and arcminutes (upper axes, tick marks at 1′ intervals). See Table 3.1 for references, error bars are not available.

Chapter 4

Numerical Methods

4.1 Numerical Integration

The computation of rotation curves (Eqs. 2.3 & 2.6) and the cumulative masses for arbitrary axially symmetric density profiles requires numerical integration. We solve integrals with the Numerical Recipes subroutine *qtrap*, which evaluates the integral of a function $f(r)$ between the limits $r = a$ and $r = b$ by applying the trapezoid rule to a successively refined grid of points starting with a and b, until a specified fractional accuracy ϵ is achieved.

4.1.1 Disk

For the special case of a thin exponential disk we can compute the rotation curve with the exact analytic expression (Eq. 2.19). For a thick disk, or a more general radial density profile for the disk, we must use Eq. (2.3) which requires a numerical computation. Eq. (2.3) involves the radial derivative of the surface density, which, for an exponential disk, is given by

$$\frac{\partial \Sigma}{\partial R} = -\frac{\Sigma_0}{R_\mathrm{d}} e^{-R/R_\mathrm{d}}. \tag{4.1}$$

Using Eq. (2.3), we can easily reproduce the rotation curve of a thin exponential disk as computed from Eq. (2.19), as shown in Fig. (2.1).

For a surface density derived directly from the surface brightness or the HI column density, we need to interpolate between the observed data points, and then use a finite difference approximation (FDA)

$$\frac{\partial \Sigma(R)}{\partial R} = \frac{\Sigma(R + dR) - \Sigma(R - dR)}{2\,dR}. \tag{4.2}$$

This FDA is accurate to second order in dR. We choose to interpolate using linear interpolation, as this is more robust than a cubic spline. The choice of too small an increment dR can generate sudden changes in the derivative of the surface density at each sampled data point, resulting in a ragged rotation curve and longer integration times to achieve a given accuracy. Thus we use an increment dR equal to the mean radial spacing of the data points. Figs. (4.1 – 4.6) show surface brightness and gas surface density profiles, their radial derivatives using an FDA with a range of dR, and rotation curves for thin and thick disks calculated from Eq. (2.3) with $\epsilon = 10^{-3}$. The effect of a thick disk is to smooth out the features in the rotation curve, while slightly lowering the velocity.

4.1.2 Halo

Computation of the rotation curve for the halo requires integrating Eq. (2.6) with ϵ to be specified. For a spherical halo we have given analytic expressions for ISO (Eq. 2.26), and $\alpha = 0$, 0.5, 1.0, 1.5 (App. E) halos. As with the disk-only case above, these expressions can be used to determine the accuracy of our numerical procedures. The choice of $\epsilon = 10^{-3}$ yields rotation curves consistent with the analytic expressions to 2 or 3 decimal places.

The adiabatic contraction of the halo requires computing the mass of the gas, disk and *initial* halo. For the gas and disk this is done by integrating the interpolated surface density profiles; for the halo, we integrate the model density profile. Our adiabatic contraction calculation outputs the new radius of a given grid of input halo masses. The number of grid points does not affect the accuracy of the routine, though the prescription breaks down at very small radii, so the grid spacing cannot be too small near the centre.

To compute the rotation curve from a contracted halo we first calculate the radial derivative of the mass (using the centred FDA, as in Eq. 4.2),

$$\frac{d\,M(r)}{d\,r} = 4\,\pi\,r^2\,q\,\rho(r), \tag{4.3}$$

which is proportional to the integrand in Eq. (2.6). We then interpolate Eq. (4.3) and use *qtrap* to integrate Eq. (2.6) in order to obtain the halo rotation curve. As a test of the interpolation and integration schemes for the spherical case, we compare the rotation curves derived as above to those derived directly from the mass output from adiabatic contraction using $v^2 = GM/r$. We use this comparison to choose numerical parameters that give rotation curves consistent to 2 decimal places.

4.2 Optimization

The rotation curve model is the quadratic sum of rotation curves of the individual mass components (i.e. disk, gas, and halo). Our model has at most 6 free parameters $\vec{a}$:

$$\vec{a} = (\Upsilon_{\rm disk}, \rho_0, r_{\rm s}, \alpha, q, f_{\rm HI}\ ). \tag{4.4}$$

As discussed in §(2.3), we can specify the halo in terms of (v_{200}, c) for ALP, or $(v_\infty, r_{\rm s})$ for ISO, instead of $(\rho_0, r_{\rm s})$.

4.2.1 Non-linear χ^2 Minimization

The best fitting model is obtained by minimizing the χ^2 statistic

$$\chi^2 = \sum_{i=1}^{n} \left(\frac{v_{\rm obs}(r_i) - v_{\rm model}(r_i, \vec{a})}{\sigma^2(r_i)} \right)^2, \tag{4.5}$$

over all the data points, where $v_{\rm obs}(r_i)$ is the observed rotational velocity at position r_i, with standard deviation $\sigma(r_i)$. We use the Levenberg-Marquardt non-linear optimization method *mrqmin* from Numerical Recipes (see §15.4). This method requires the derivative of the model with respect to the model parameters:

$$\frac{\partial v}{\partial a} = \frac{1}{2\,v}\frac{\partial\, v^2}{\partial\, a}. \tag{4.6}$$

For non-contracted halos, there are simple analytic expressions for the derivatives of $\Upsilon, f_{\rm HI}\ , \rho_0, v_{200}, v_\infty$:

$$\begin{aligned}
\frac{\partial\, v^2}{\partial\, \Upsilon} &= \frac{1}{\Upsilon}\, v_{\rm disk}^2\,; && (4.7)\\
\frac{\partial\, v^2}{\partial\, f_{HI}} &= -\frac{1}{f_{HI}}\, v_{\rm gas}^2\,; && (4.8)\\
\frac{\partial\, v^2}{\partial\, \rho_0} &= \frac{1}{\rho_0}\, v_{\rm halo}^2\,; && (4.9)\\
\frac{\partial\, v^2}{\partial\, v_{200}} &= \frac{2}{v_{200}}\, v_{\rm halo}^2\,; && (4.10)\\
\frac{\partial\, v^2}{\partial\, v_\infty} &= \frac{2}{v_\infty}\, v_{\rm halo}^2\,. && (4.11)\\
& && (4.12)
\end{aligned}$$

For special spherical halo cases, we can take derivatives with respect to $r_{\rm s}$ and c of the analytic expressions of the velocity given in Eqs. (2.55 − 2.59), though for halos with arbitrary q and α we need to follow one of two courses. Firstly we can take the derivative inside the integral of Eq. (2.6) and compute the resulting integrals,

$$\begin{aligned}
\frac{\partial\, v^2}{\partial\, r_{\rm s}} &= \frac{G}{r}\int_0^r -\frac{u}{r_{\rm s}^2}\,\beta(\frac{u}{r_{\rm s}})\frac{\rho(u)}{\sqrt{1-e^2\frac{u^2}{r^2}}}\,4\pi q\, u^2 du, && (4.13)\\
\frac{\partial\, v^2}{\partial\, c} &= -\frac{c}{r_{\rm s}}\frac{\partial\, v^2}{\partial\, r_{\rm s}}, && (4.14)\\
\frac{\partial\, v^2}{\partial\, q} &= \frac{G}{r}\int_0^r \frac{-4\,q\,e\,u^2/r^2}{1-e^2\,\frac{u^2}{r^2}}\frac{\rho(u)}{\sqrt{1-e^2\frac{u^2}{r^2}}}\,4\pi q\, u^2 du, && (4.15)\\
\frac{\partial\, v^2}{\partial\, \alpha} &= \frac{G}{r}\int_0^r -\left\{\ln\left(\frac{u}{r_{\rm s}}\right)+\ln\left(1+\frac{u}{r_{\rm s}}\right)\right\}\frac{\rho(u)}{\sqrt{1-e^2\frac{u^2}{r^2}}}\,4\pi q\, u^2 du, && (4.16)
\end{aligned}$$

where $\beta(x)$ is the logarithmic slope of the density profile at x (Eq. 2.41). Secondly we could use a FDA,

$$\frac{\partial v_{\rm model}}{\partial da} = \frac{v_{\rm model}(a+da) - v_{\rm model}(a)}{a}. \tag{4.17}$$

The subroutine *mrqmin* requires initial guesses of the model parameters. The choice of initial guesses is crucial for *mrqmin* to converge to a realistic solution. The use of v_∞ (Eq. 2.27) and v_{200} (Eq. 2.38) helps constrain the range of possible values. Reasonable guesses are $\Upsilon \sim 0.5$, v_{200} or $v_\infty \sim 100$, $r_{\rm c}$, $r_{\rm s}$ or $c \sim 5$. If we fit for q or α, we initialize both of these at 1. We also initialize *mrqmin* with $\lambda < 0$, and then repeatedly call *mrqmin* until the following conditions are satisfied,

$$\begin{aligned}
\chi^2 &< \chi^2_{\rm old}, \quad \text{and} && (4.18)\\
\chi^2 - \chi^2_{\rm old} &< 10^{-3}, \quad \text{and} && (4.19)\\
\chi^2 - \chi^2_{\rm old} &< 10^{-4}\,\chi^2, \quad \text{or} && (4.20)\\
\lambda &> 10^{-8}, \quad \text{or} && (4.21)\\
\lambda &< 10^{8}, \quad \text{or} && (4.22)\\
\text{no. of iterations} &> 1000, && (4.23)
\end{aligned}$$

where $\chi^2_{\rm old}$ is the χ^2 value from the previous iteration. As changes in $\chi^2 \ll 1$ are *never* statistically significant it is wasteful and unnecessary to iterate to convergence or machine accuracy. The last condition on the number of iterations prevents a runaway, e.g. if the parameters are wandering around near the minimum, or the initial guesses are poor. In this case we modify the initial guesses and try again.

4.2.2 Covariance Matrix

Once an acceptable minimum has been found, we set $\lambda = 0$ and *mrqmin* computes the estimated covariance matrix $\mathrm{cov}(i,j)$ of the standard errors in the fitted parameters $\vec{a}$.

The standard deviation of the parameters is the square-root of the diagonal elements,

$$\sigma(a_i) = \sqrt{\mathrm{cov}(i,i)} \tag{4.24}$$

while the correlation coefficient $\mathrm{cor}(i,j)$ between two parameters a_i and a_j is defined as

$$\mathrm{cor}(i,j) = -\mathrm{cov}(i,j)/\sqrt{\mathrm{cov}(i,i)\,\mathrm{cov}(j,j)} \tag{4.25}$$

and lies between -1 and 1, inclusive. If $\mathrm{cor}(i,j) = 1$, the parameters a_i and a_j are completely correlated, i.e. increasing a_i by σ_i and a_j by σ_j results in the same χ^2. If $\mathrm{cor}(i,j) = -1$, the parameters are anti-correlated, and increasing a_i by σ_i while decreasing a_j by σ_j preserves the χ^2. If $\mathrm{cor}(i,j) = 0$, a_i and a_j are uncorrelated. The correlation of a parameter with itself is -1, as we can increase and decrease its value by the same amount and the χ^2 remains unchanged.

As the rotation curve error bars are not true 1σ errors, we can only use the covariance matrix in a relative sense.

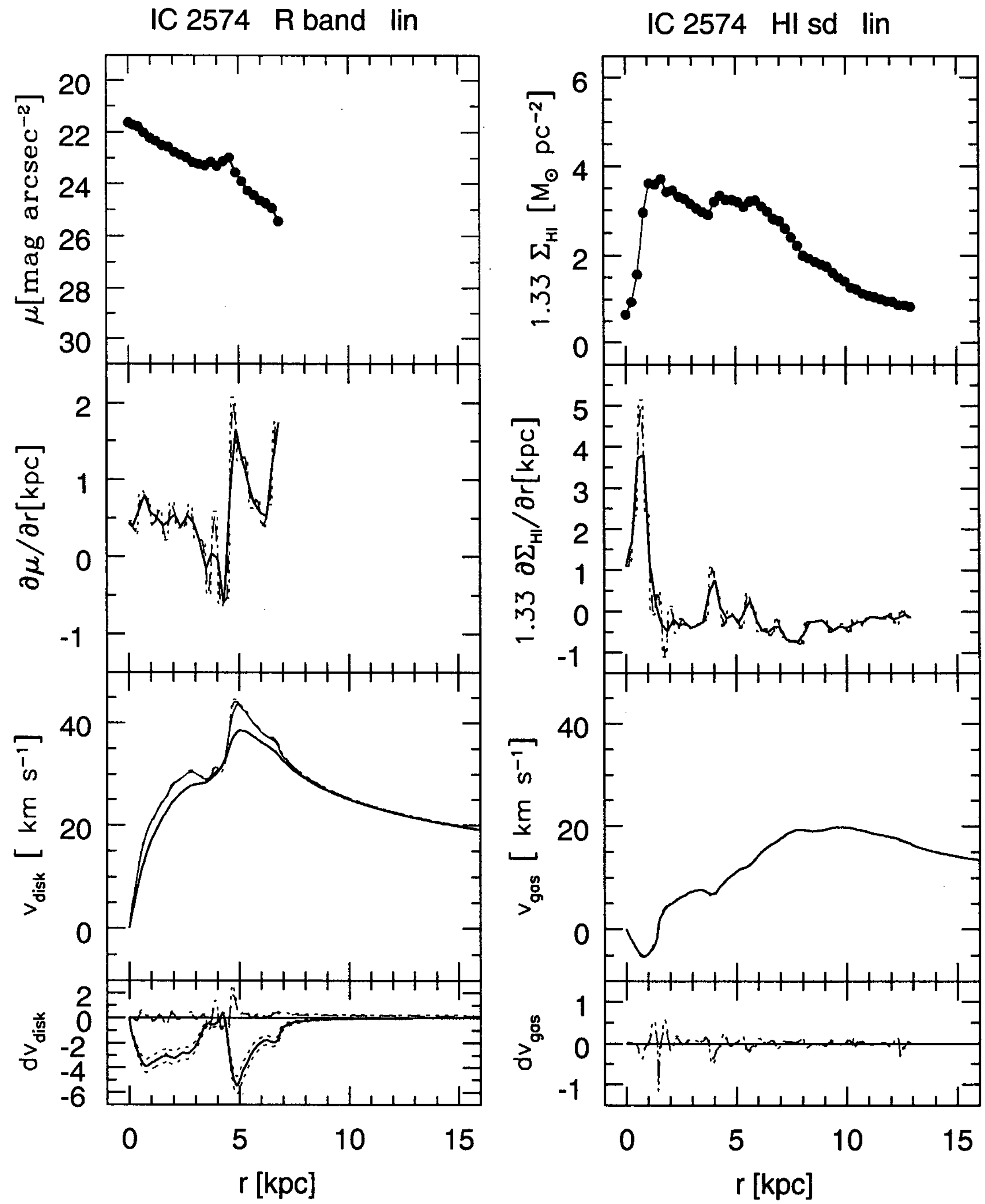

Figure 4.1: Interpolated data, radial derivatives, and rotation curves for the stellar disk (left), and gas disk (right) for IC 2574. The solid, dashed, and dotted lines in the middle panel correspond to a dR equal to the mean spacing between the data points, Δ, 0.5Δ, and 0.1Δ, respectively. The lower panel shows the rotation curves of a thin (solid) and thick (thick solid) disk with intrinsic thickness of 0.25, and the corresponding residuals. Also shown is the effect of a disk with intrinsic thickness 0.2 and 0.3 (dotted).

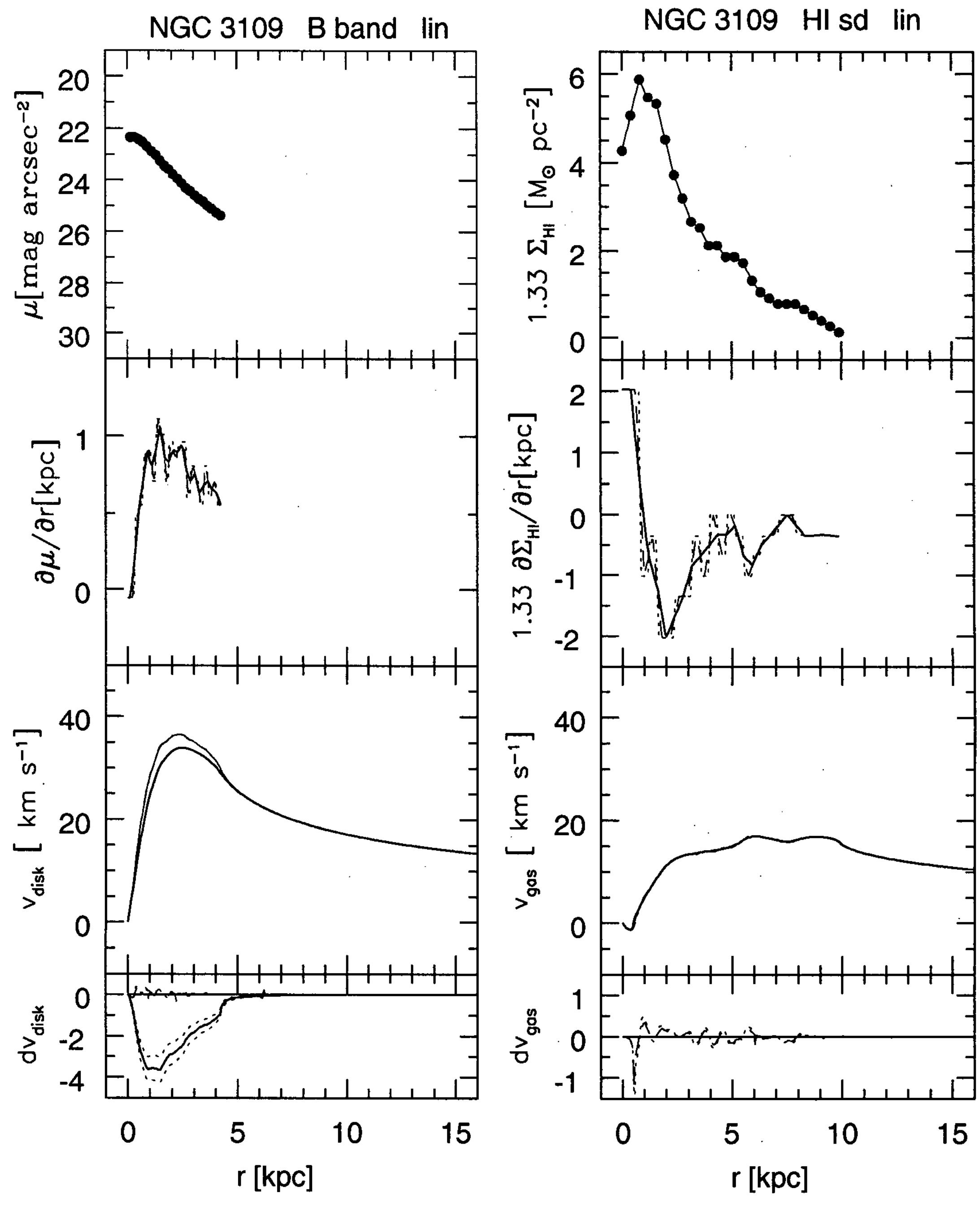

Figure 4.2: As Fig. (4.1) but for NGC 3109.

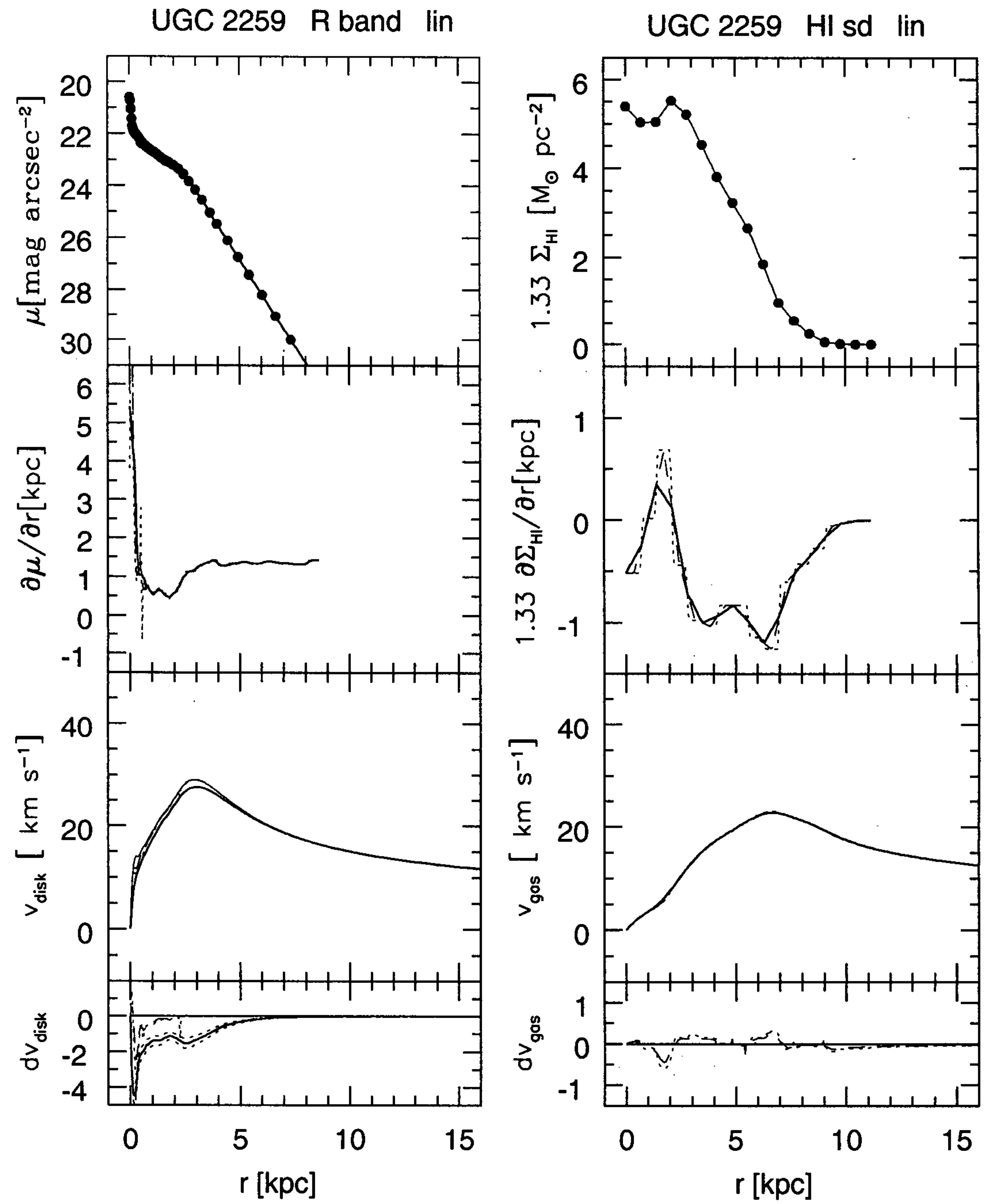

Figure 4.3: As Fig. (4.1) but for UGC 2259.

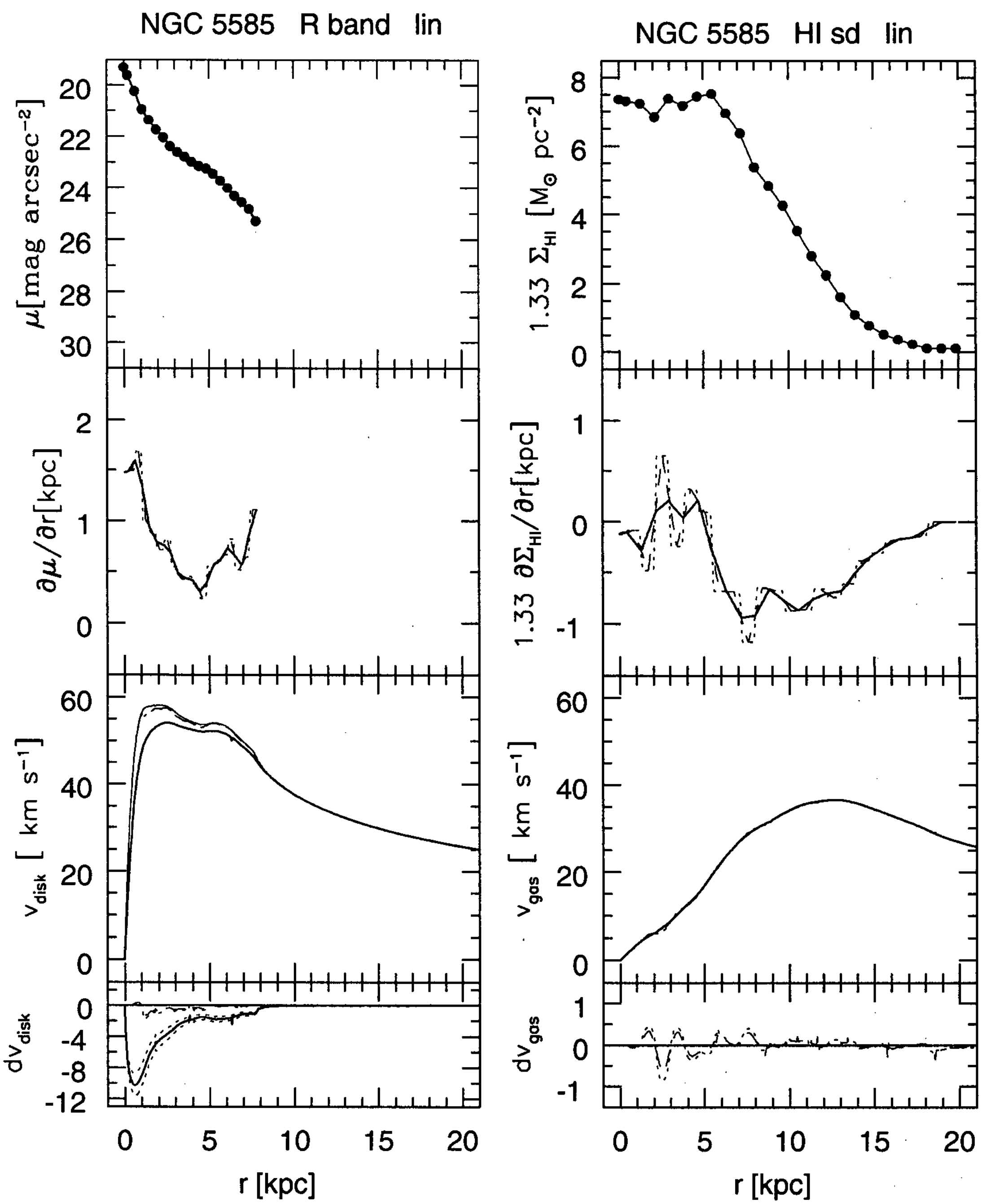

Figure 4.4: As Fig. (4.1) but for NGC 5585.

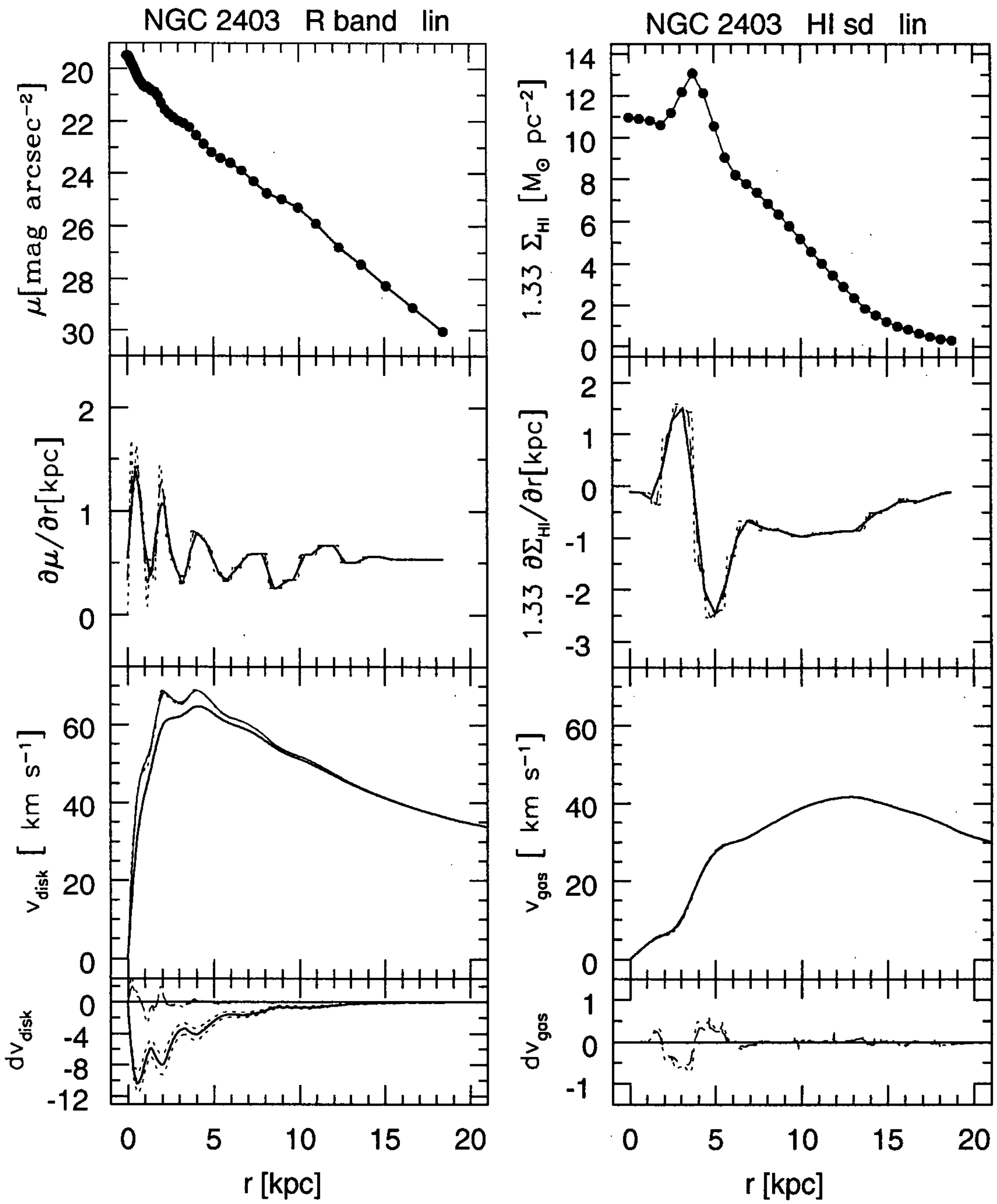

Figure 4.5: As Fig. (4.1) but for NGC 2403.

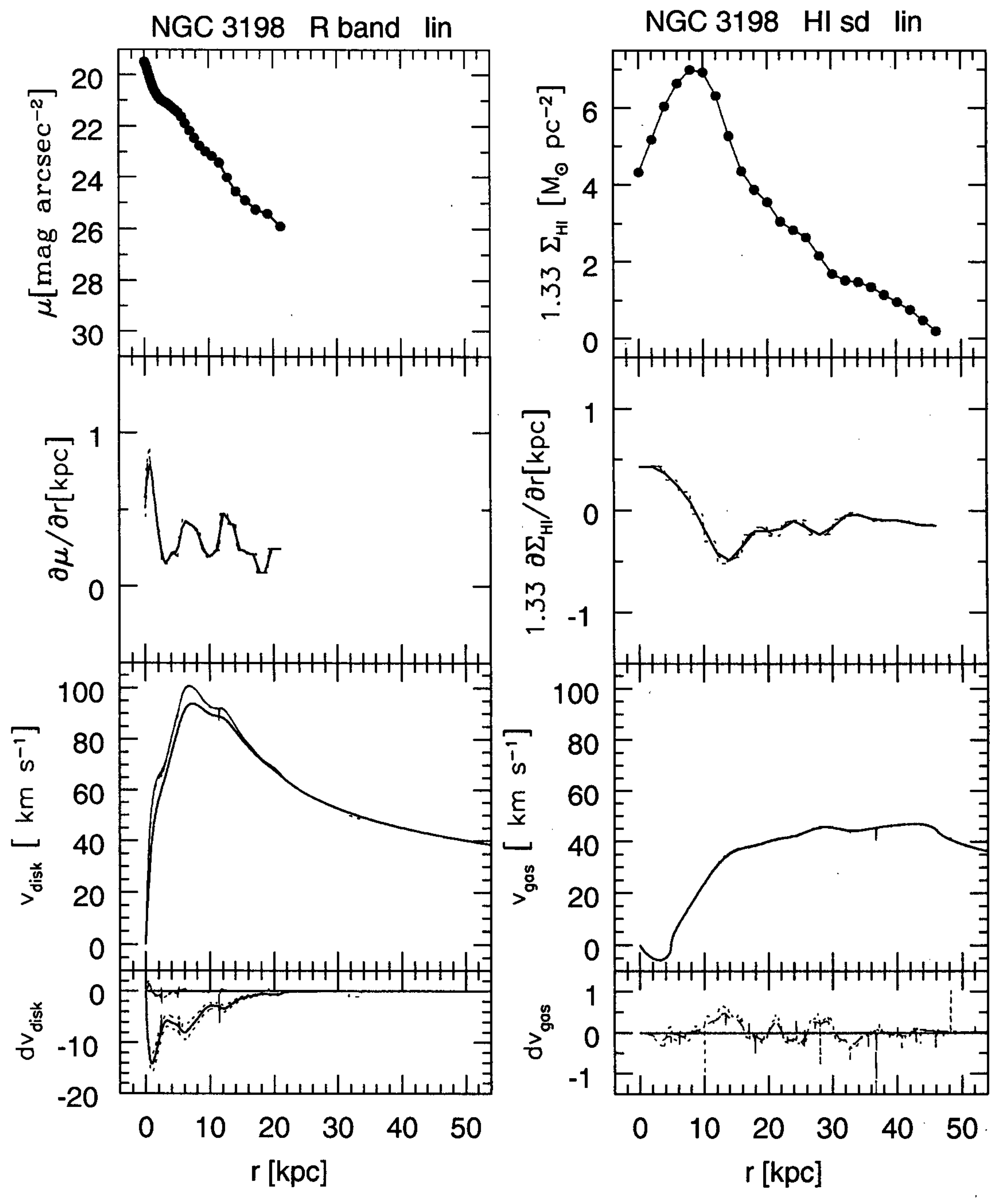

Figure 4.6: As Fig. (4.1) but for NGC 3198.

Chapter 5

Rotation Curve Fits

5.1 Comparison with Blais-Ouellette

We test our rotation curve fitting code on 6 bulge-less galaxies previously studied by Blais-Ouellette (2000 hereafter B00) using the same data and mass models. We did not consider the bulge dominated systems in B00 to avoid ambiguities in about the light profile decomposition. Electronic data files, provided by Claude Carignan, consisted of combined Hα and HI rotation curves, HI surface density profiles multiplied by $\frac{4}{3}$ to correct for helium, and B-band surface photometry. For NGC 2403 and NGC 3198 the photometry comes from the R-band data of Kent (1987) and is converted to B-band using B$-$R=1. Since $\mathrm{M}_{\odot}^{\mathrm{B}} - \mathrm{M}_{\odot}^{\mathrm{R}} = 1.02$, this conversion is roughly justified (assuming a solar composition), but nonetheless coarse.

B00 fitted 4 halo models with inner and outer density slopes specified by $(-\alpha, -\gamma)$: [ISO $(0, -2)$, Burkert $(0, -3)$, KKPB[1] $(-0.2, -3)$, and NFW $(-1, -3)$] and 3 free parameters: M/L_{B}, ρ_0, and r_{s}. For comparison purposes, we fit the ISO and NFW halos with: a 3-parameter fit, a 2-parameter halo fit with M/L_{B} fixed, a M/L_{B} fit with the halo profile fixed, and a fit with all parameters fixed at the Blais-Ouellette values. B00 did not specify the thickness of the disk, so for simplicity we assume, for our initial comparison, a zero thickness disk. We use distances provided by B00 as given in Table 3.1. The final parameters from our fits are shown in Tables 5.1 – 5.2 for ISO and NFW halos,

[1] Klypin et al. (1998). These authors later realized that their convergence tests had been inadequate. After simulating a small number of galaxy-size halos with high resolution, Klypin et al. (2001) find a range of profiles between NFW and Moore.

Galaxy Fit	χ^2_{dof}	M/L_{B} $[M_\odot/L_\odot^{\mathrm{B}}]$	ρ_0 $[10^{-3}\,\mathrm{M_\odot\,pc^{-3}}]$	r_s [kpc]	v_∞ $[\mathrm{km\,s^{-1}}]$	r_{200} [kpc]
IC 2574						
Free	3.0	0.10(0.03)	5.86(0.27)	9.3(1.2)	166	229
Fix disk	5.0	0.3	5.1(1.0)	10.3(0.9)	244	237
Fix halo	4.8	0.06(0.01)	7.5	5.0	101	140
Fix all	12.1	0.3	7.5	5.0	101	140
B01	2.7	0.3	7.5	5.0		
NGC 3109						
Free	0.43	0.00(0.27)	24.3(12.8)	2.41(0.9)	87.5	123
Fix disk	0.43	0.10	19.4(1.3)	2.85(0.2)	92.1	129
Fix halo	0.42	0.01	24	2.4	86.4	122
Fix all	0.73	0.1	24	2.4	86.4	122
B01	0.44	0.1	24	2.4		
UGC 2259						
Free	3.1	0.75(0.37)	567(67)	0.50(0.03)	87.3	125
Fix disk	3.2	0.0	677(42)	0.48(0.02)	92.2	131
Fix halo	2.9	0.24(0.06)	658	0.48	92.2	131
Fix all	3.6	0.0	658	0.48	92.2	129
B00	1.2	0.0	658	4.8		
NGC 5585						
Free	1.2	0.03(0.14)	95.4(23.3)	1.37(0.18)	98.5	140
Fix disk	5.3	0.85	23.8(1.8)	3.06(0.18)	110	154
Fix halo	2.1	0.46(0.03)	42.5	2.15	103	146
Fix all	9.2	0.85	42.5	2.15	103	146
B00	4.4	0.85	42.5	2.15		
NGC 2403						
Free	1.3	1.96(0.03)	17.2(0.8)	4.9(0.1)	150	210
Fix disk	6.3	2.5	7.1(0.1)	9.16(0.03)	179	249
Fix halo	1.4	1.98(0.02)	17	4.8	146	204
Fix all	9.9	2.5	17	4.8	146	204
B01	1.9	2.5	17	4.8		
NGC 3198						
Free	7.6	1.79(0.12)	64(14)	2.48(0.29)	146	206
Fix disk	127	4.8	2.04(0.07)	21.8(1.0)	229	310
Fix halo	9.4	2.00(0.02)	57	2.54	141	199
Fix all	318	4.8	57	2.54	141	199
B00	7.1	4.8	57	2.54		

Table 5.1: Comparison of our ISO halo fits with those of B00 and Blais-Ouellette et al. (2001; hereafter B01). The first column gives the galaxy name and the choice of model fit. The formal 1σ errors for the model parameters are given in parentheses.

Galaxy Fit	χ^2_{dof}	M/L_B $[M_\odot/L^B_\odot]$	ρ_0 $[10^{-3}\,M_\odot\,pc^{-3}]$	r_s [kpc]	v_{200} $[km\,s^{-1}]$	r_{200} [kpc]	c
IC 2574							
Free	29.7	0.00(0.20)	0.05(0.24)	298(1.3e3)	217	310	1.04
Fix disk	28.1	0.00	5.9e-3(0.7e-3)	2.5e3(0.3e3)	428	612	0.24
Fix halo	28.5	0.00(0.14)	0.05	295	214	306	1.04
Fix All	27.9	0.00	0.05	295	214	306	1.04
B01	32	0.00	0.05	295			
NGC 3109							
Free	2.1	0.00(0.15)	0.018(0.62)	14e3(460e3)	520	743	0.55
Fix disk	2.0	0.0	0.3e-3(0.2)	79e3(52e6)	903	1290	0.02
Fix halo	2.8	0.09(0.03)	0.035	605	355	508	0.84
Fix all	2.9	0.0	0.035	605	355	508	0.84
B01	9.0	0.0	0.035	605			
UGC 2259							
Free	6.4	0.84(0.46)	59.7(9.1)	3.07(1.83)	53.1	75.8	24.7
Fix disk	6.3	0.0	73.6(5.1)	2.93(0.13)	54.9	78.4	26.8
Fix halo	6.0	0.47(0.06)	57	3.3	56	80	24.2
Fix all	8.8	0.0	57	3.3	56.0	80.0	24.2
B00	4.2	0.0	57	3.3			
NGC 5585							
Free	2.9	0.00(0.17)	9.59(4.22)	8.68(2.18)	73.1	104	12.0
Fix disk	2.7	0.0	8.66(0.91)	9.27(0.64)	74.5	107	11.5
Fix halo	2.7	0.00(0.03)	7.7	10.1	77.8	111	11.0
Fix all	2.6	0.0	7.7	10.1	77.8	111	11
B00	7.9	0.0	7.7	10.1			
NGC 2403							
Free	1.1	1.22(0.12)	6.2(2.1)	14.9(2.9)	105	150	10.1
Fix disk	1.1	1.4	3.64(0.37)	20.3(1.4)	115	164	8.1
Fix halo	1.2	1.13(0.02)	9.0	11.8	96.8	138	11.7
Fix all	3.6	1.4	9.0	11.8	96.8	138	11.7
B01	1.4	1.4	9.0	11.8			
NGC 3198							
Free	9.8	1.24(0.1)	14.7(2.3)	10.5(0.7)	105	150	14.3
Fix disk	28.9	3.0	0.48(0.05)	75.6(5.6)	175	251	3.3
Fix halo	9.6	1.36(0.02)	12.7	11.2	106	151	13.5
Fix all	129	3.0	12.7	11.2	106	151	13.5
B00	44.4	3.0	12.7	11.2			

Table 5.2: Same as in Table (5.1) but using a NFW halo.

respectively. Overall we find that our fits are in good agreement with those of Blais-Ouellette. There are, however, some notable differences in the fitted values of M/L_{B} for NGC 5585, NGC 2403, and NGC 3198. This is apparent when we fix the halo at the Blais-Ouellette parameter values, and fit for M/L_{B}; the resulting disk rotation curves are then identical even though our M/L_{B} are significantly lower. These differences in M/L_{B} may be explained by adding thickness to the disk, and/or correcting the surface brightness profile for inclination (extinction effects on the other hand would bias our M/L_{B} high). Alternatively, as there are minor errors in the tables of fit parameters given in B00, and some of the mass decompositions have been corrected in B01, their fit parameters may not be reliable. However, for our present purposes the exact value of M/L is not critical, though in our future work we will need to make corrections for inclination (our K-band data should not be effected by extinction) if we are to apply SPS constraints on M/L.

We also express the halo in terms of asymptotic velocity v_∞ for ISO, and the parameters c, and v_{200} for NFW. This makes the velocity profile of the halo more apparent and enables a comparison with halos generated by N-body simulations. Several of the "best" fits listed in Table 5.1 are unphysical, with zero M/L_{B}, too small halo concentrations, or too large virial velocities. As discussed in §2.5, we expect $M/L_{\mathrm{B}} \geq 0.5$, $3 < c < 25$ and $v_{200} < 200\,\mathrm{km\,s^{-1}}$. To enable us to apply these constraints on the halo parameters, we now parameterize the halo in terms of c and v_{200} for NFW and r_{c} and v_∞ for ISO.

5.2 Systematic Modeling Errors

We consider the effects of adopted photometric parameters, distance, and rotation curve error bars, on the parameters of the best fits. The results of these tests are presented in Figs. (5.1 – 5.3), where we show the reduced χ^2 and halo parameters against M/L. For each galaxy we fix M/L and compute 2-parameter fits with ISO (upper panels) and NFW (lower panels) halos with the following in succession;

- HI $-$Hα hybrid rotation curves (rc), B-band photometry, and HI surface density data from Carignan (left panels, solid line);
- R-band photometry from the literature with disk truncated at $\mu_{\rm R} = 26$, and thickness $q_0 = 0.25$ (left panels, dashed line) replacing the B-band photometry of Carignan.
- Our adopted distance (left panels, dotted line);
- The original HI and Hα rotation curves (IA) as opposed to the hybrid rotation curves provided by Carignan (right panels, solid line);
- A minimum velocity error of 1 $\mathrm{km\,s^{-1}}$ (right panels, dashed line);
- A minimum velocity error of 4 $\mathrm{km\,s^{-1}}$ (right panels, dotted line).

In general, variations in the photometry parameters and distance do not alter the fits significantly. The exception is NGC 3198, where our adopted distance is 50% larger than Blais-Ouellette's, resulting in a larger contribution from the gas and a lower maximum disk M/L.

Changing the minimum rotation curve errors has the effect of lowering the global χ^2, though the trends in M/L and ISO vs. NFW are preserved. Given the uncertainty in the definition of rotation curve error bars, we cannot use the value of χ^2 to make absolute

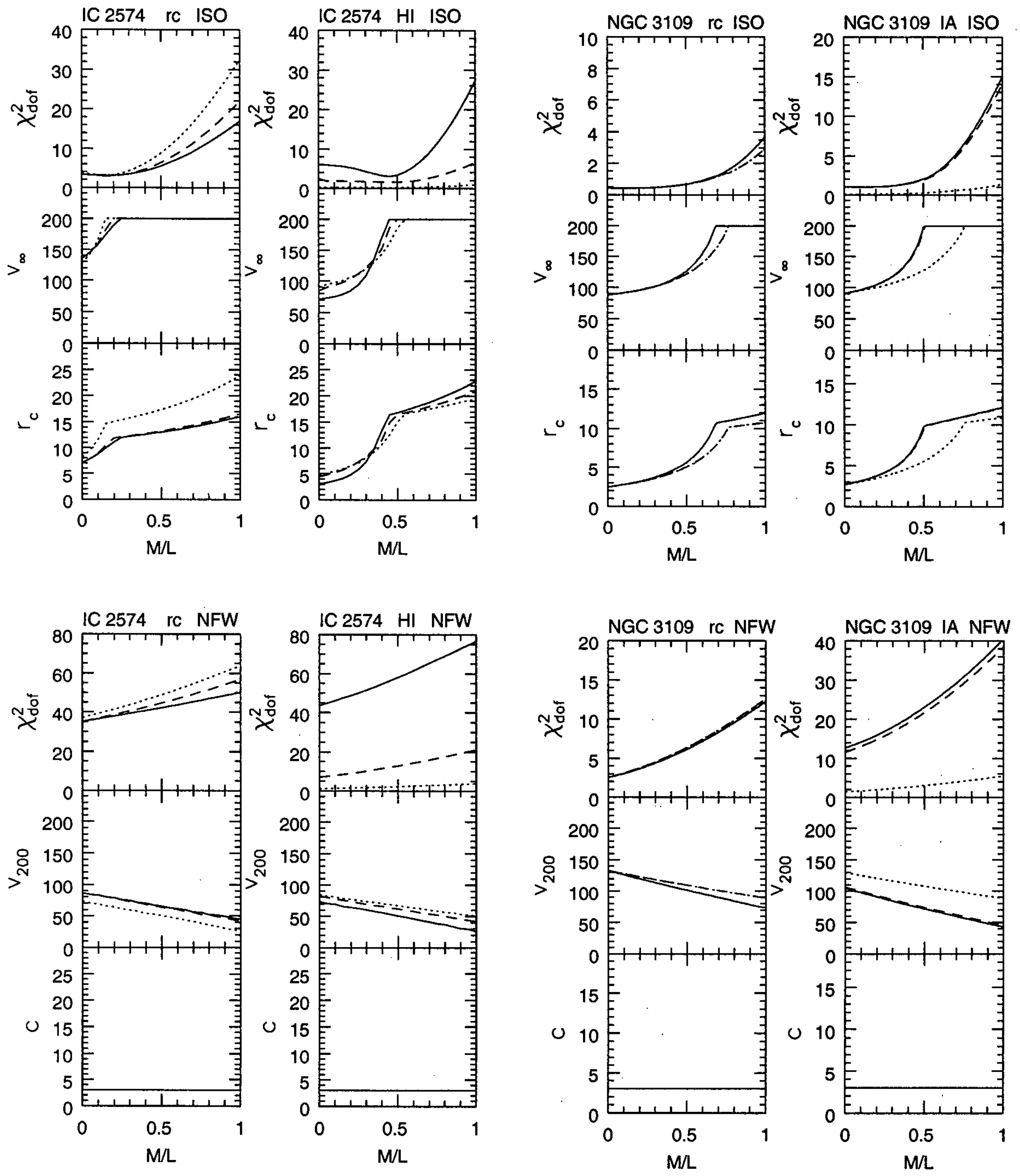

Figure 5.1: Systematic effects on rotation curve fit parameters for IC 2574 (right), and NGC 3109 (left), with M/L fixed.

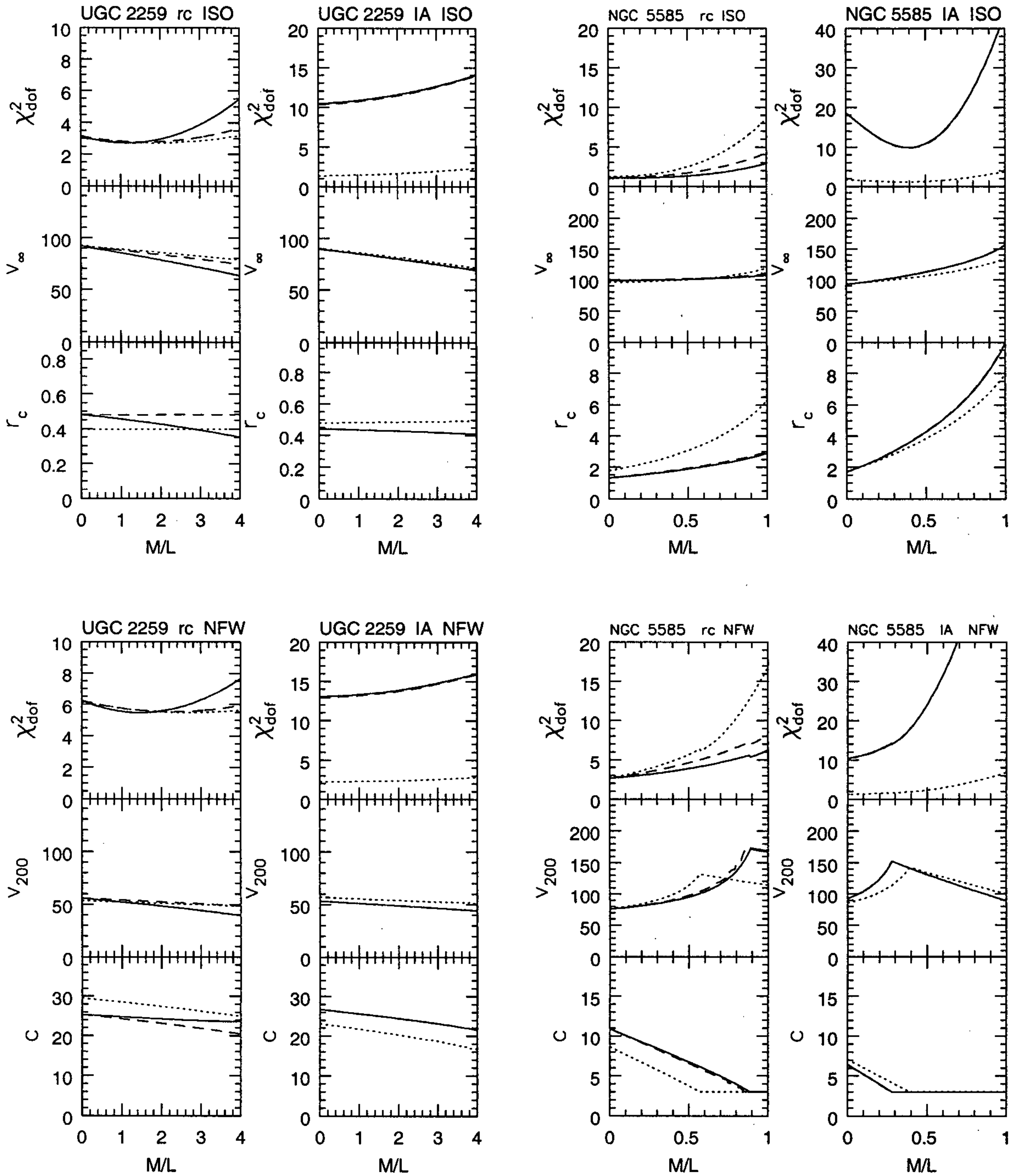

Figure 5.2: As Fig. (5.1), but for UGC 2259 (left), and NGC 5585 (right).

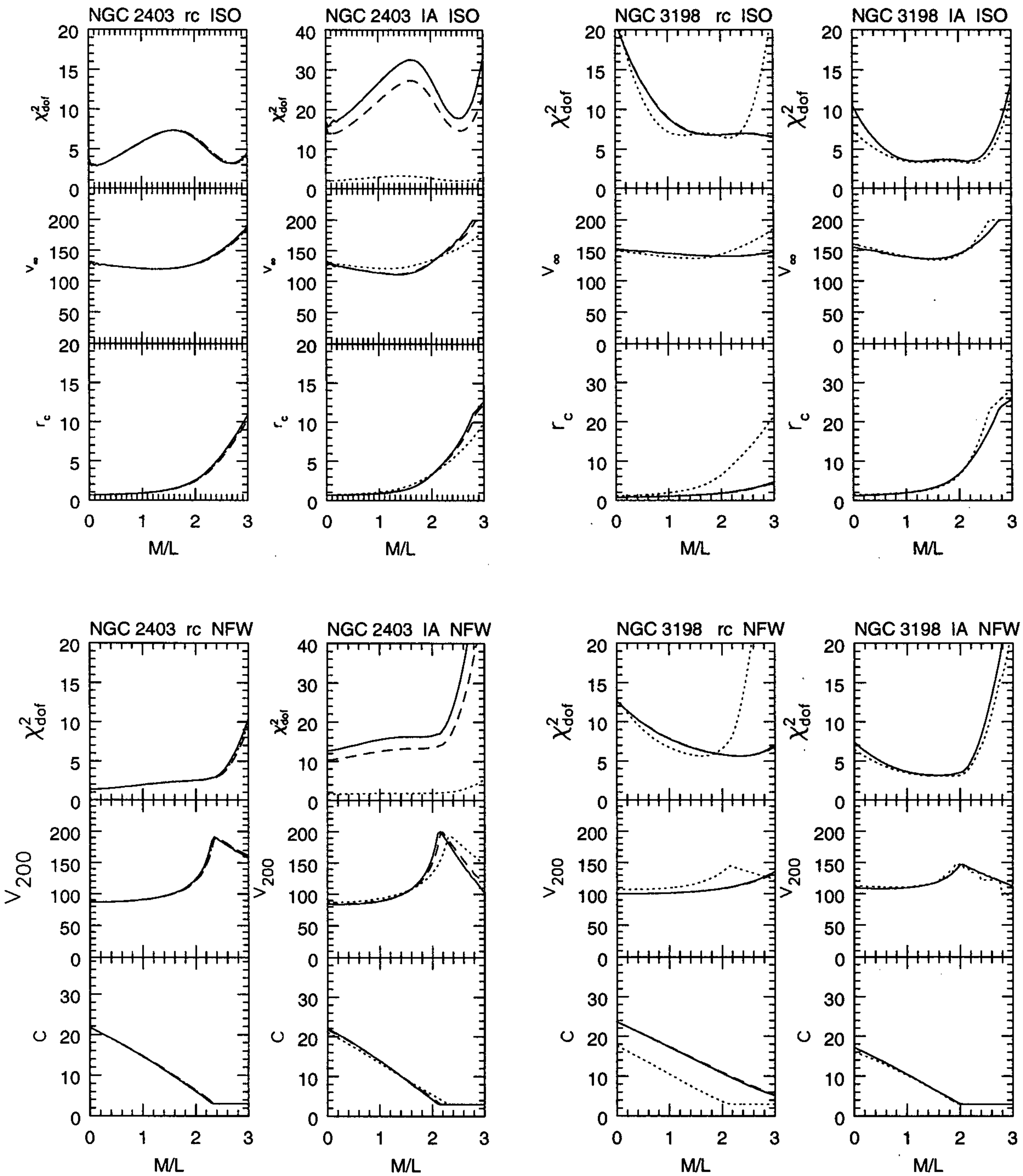

Figure 5.3: As Fig. (5.1), but for NGC 2403 (left), and NGC 3198 (right).

p / ν	1	2	3	4	5	6
68.3%	1.00	2.30	3.53	4.72	5.89	7.04
90%	2.71	4.61	6.25	7.78	9.24	10.6
95.4%	4.00	6.17	8.02	9.70	11.3	12.8
99%	6.63	9.21	11.3	13.3	15.1	16.8
99.73%	9.00	11.8	14.2	16.3	18.2	20.1
99.99%	15.1	18.4	21.1	23.5	25.7	27.8

Table 5.3: $\Delta\chi^2$ as a function of confidence level p and degrees of freedom ν (Numerical Recipes).

statements about the goodness of fit of a given model. We can however, calculate the relative goodness of fit between two or more models by imposing the condition that the "best" fitting model for each galaxy has a $\chi^2_{\mathrm{dof}} = 1$. The simplest way we can achieve this is by scaling the errors by the square root of the lowest χ^2_{dof}. Table 5.3 shows the difference in χ^2_{dof} confidence level that is associated with a given confidence level, for a given number of degrees of freedom. Most of our fits have 2 degrees of freedom, so a difference of 2.30, 6.17, or 11.8 in χ^2_{dof} corresponds to a 1, 2, or 3σ level, respectively.

However, large χ^2_{dof} values can result from a handful of data points with underestimated error bars, or for example non-circular motions that do not represent the underlying potential, such as wiggles in the rotation curve due to spiral structure. If we do not account for these, the velocity points that map the underlying potential may receive less weight than they should, and the relative difference in χ^2_{dof} between models will be reduced.

5.2.1 Comparison between ISO and NFW fits

Figs. 5.4 – 5.9 show the best fit models for ISO and NFW halos using truncated R band photometry and a thick stellar disk with a range of M/L_{R}, our adopted distances, and original HI and Hα rotation curves with a minimum error of 1 $\mathrm{km\,s^{-1}}$.

- IC 2574 & NGC 3109 ($V_{\rm max} = 67\,\mathrm{km\,s^{-1}}$): These are two classic examples of LSB galaxies which are apparently incompatible with CDM. Both are well fitted with an ISO halo for $M/L_{\rm R} \leq 0.5$, but in all NFW fits the rotation curve is over-estimated at small radii and under estimated at large radii. Further, the NFW fits all have $c = 3$; for more realistic (larger) concentrations the model discrepancy worsens.

- UGC 2259 ($V_{\rm max} = 90\,\mathrm{km\,s^{-1}}$): Both ISO and NFW halos fit well, though ISO is a better match than NFW in the inner 0.5 kpc, and the low $M/L_{\rm R}$ fits are marginally better than the higher $M/L_{\rm R}$ values. The high χ^2 values are due to a spiral arm feature at $2 - 3$ kpc.

- NGC 5585 ($V_{\rm max} = 92\,\mathrm{km\,s^{-1}}$): For $M/L_{\rm R} = 0$, NFW fits better than ISO, and as $M/L_{\rm R}$ increases, ISO becomes a better fit. At the maximum disk $M/L_{\rm R} = 0.5$, the ISO fit is much better than NFW. Good NFW fits require low c.

- NGC 2403 ($V_{\rm max} = 132\,\mathrm{km\,s^{-1}}$): Well fitted with either ISO or NFW, though the relative quality of the fit depends on $M/L_{\rm R}$. For $M/L_{\rm R} = 0$, NFW is better; for $M/L_{\rm R} = 1.5$, NFW is much better; and for a maximum disk $M/L_{\rm R} = 2.5$, ISO is preferred. This is a prime example of a degeneracy between disk and halo parameters which could be partly resolved by using a disk M/L constraint from SPS models.

- NGC 3198 ($V_{\rm max} = 157\,\mathrm{km\,s^{-1}}$): Again NFW fits better for $M/L_{\rm R} = 0$, and ISO fits better for a maximum disk. The fits are comparable for intermediate $M/L_{\rm R}$ values.

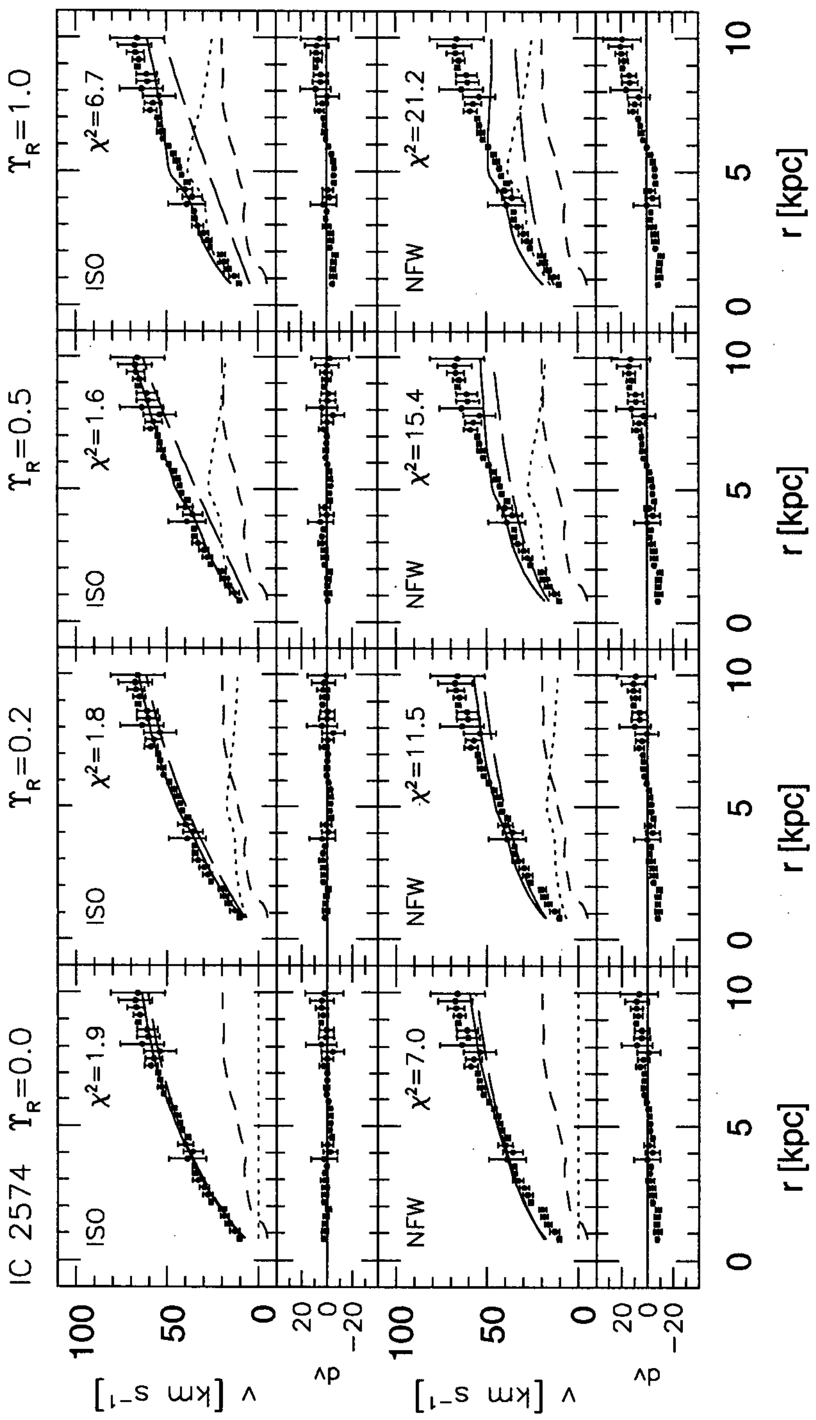

Figure 5.4: Rotation curve fits for IC 2574 with ISO and NFW halos, and a range of $M/L \equiv \Upsilon$.

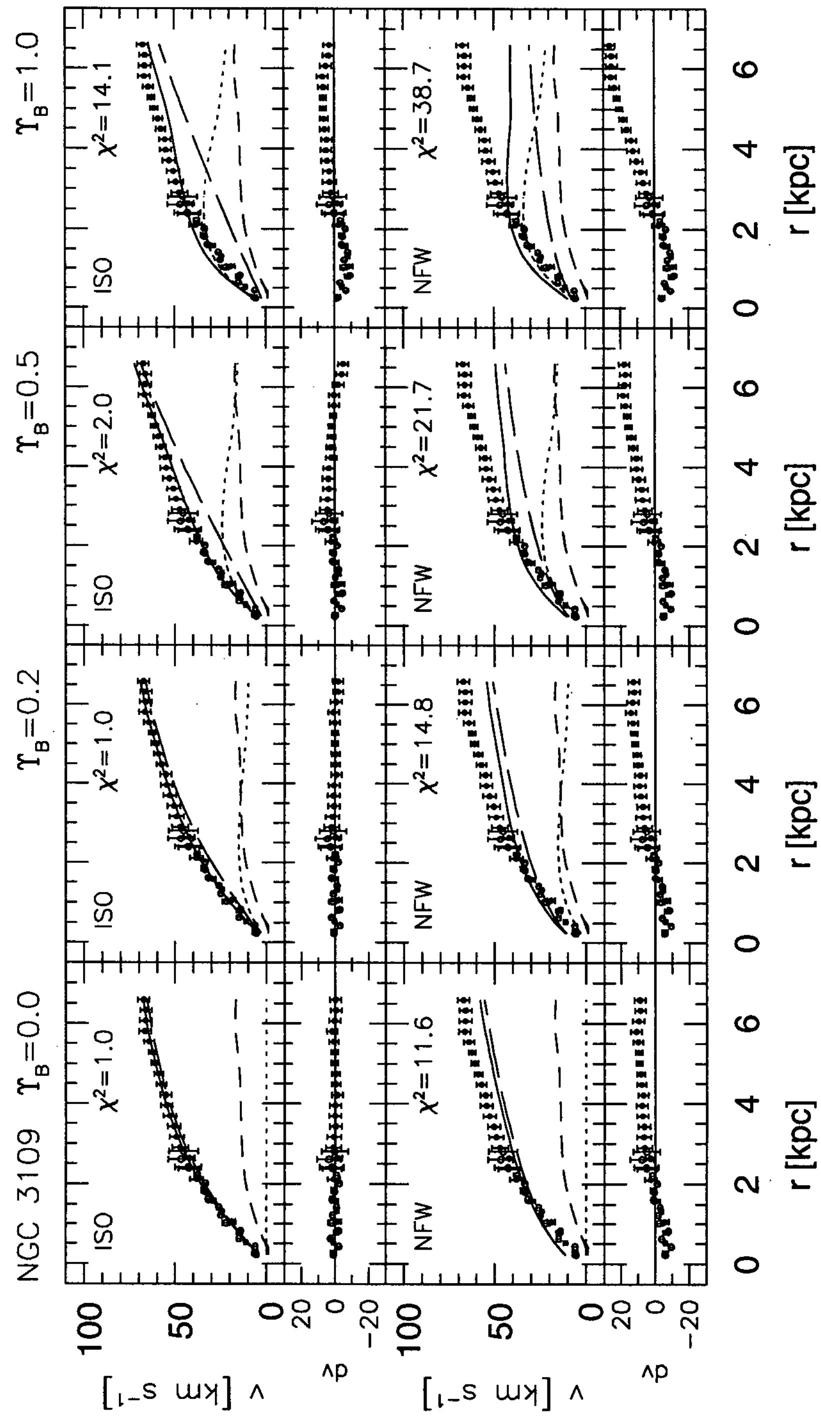

Figure 5.5: As Fig. (5.4), but for NGC 3109.

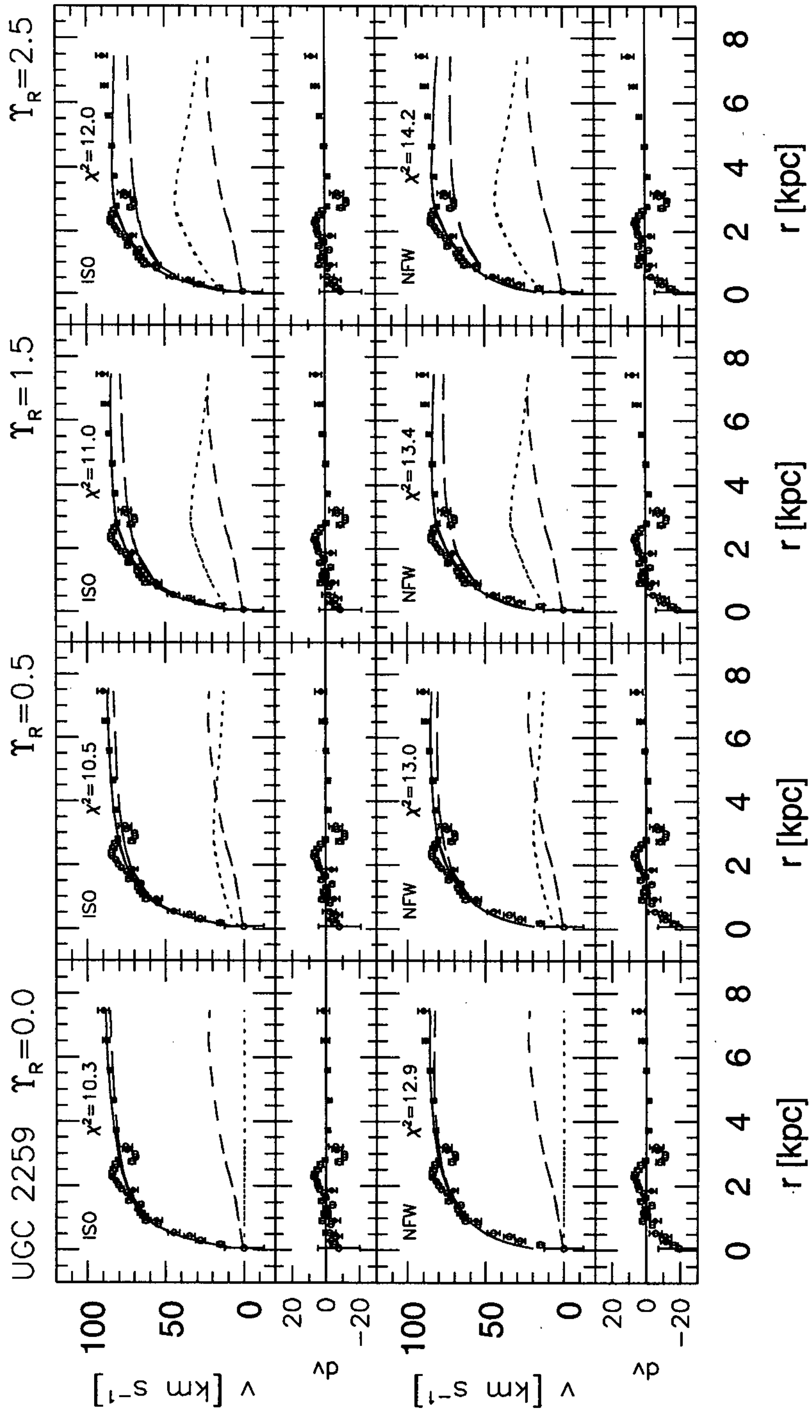

Figure 5.6: As Fig. (5.4), but for UGC 2259.

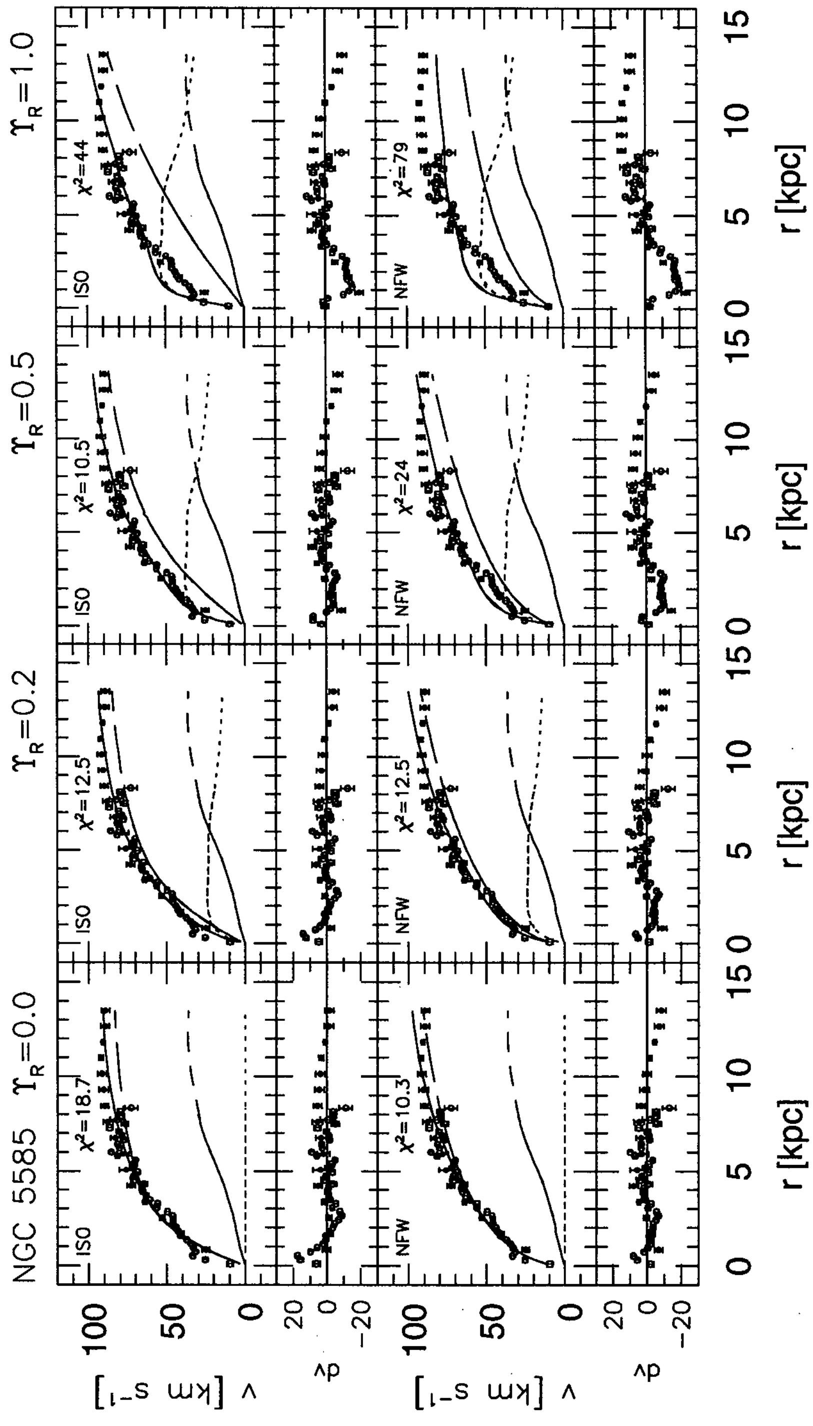

Figure 5.7: As Fig. (5.4), but for NGC 5585.

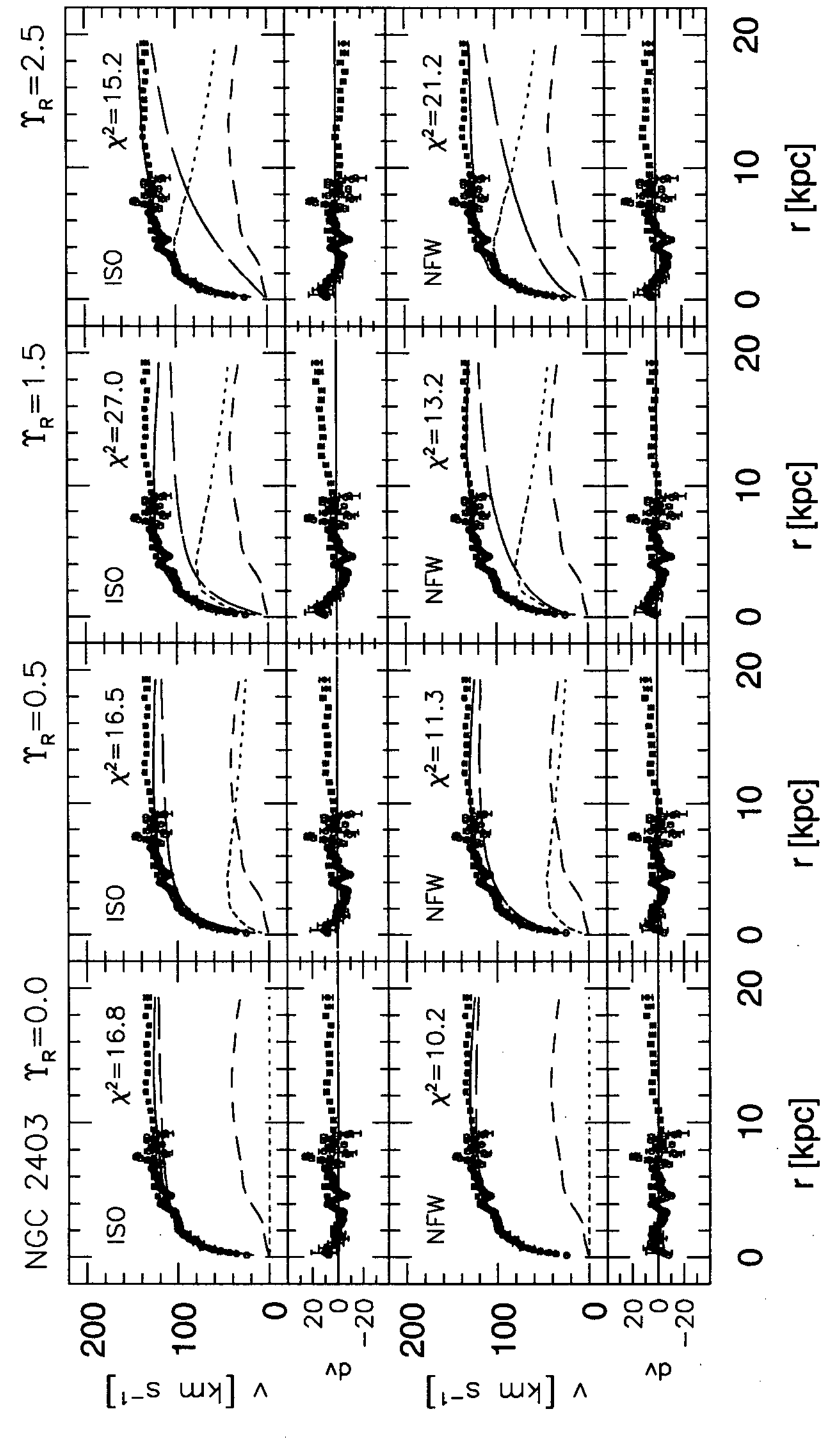

Figure 5.8: As Fig. (5.4), but for NGC 2403.

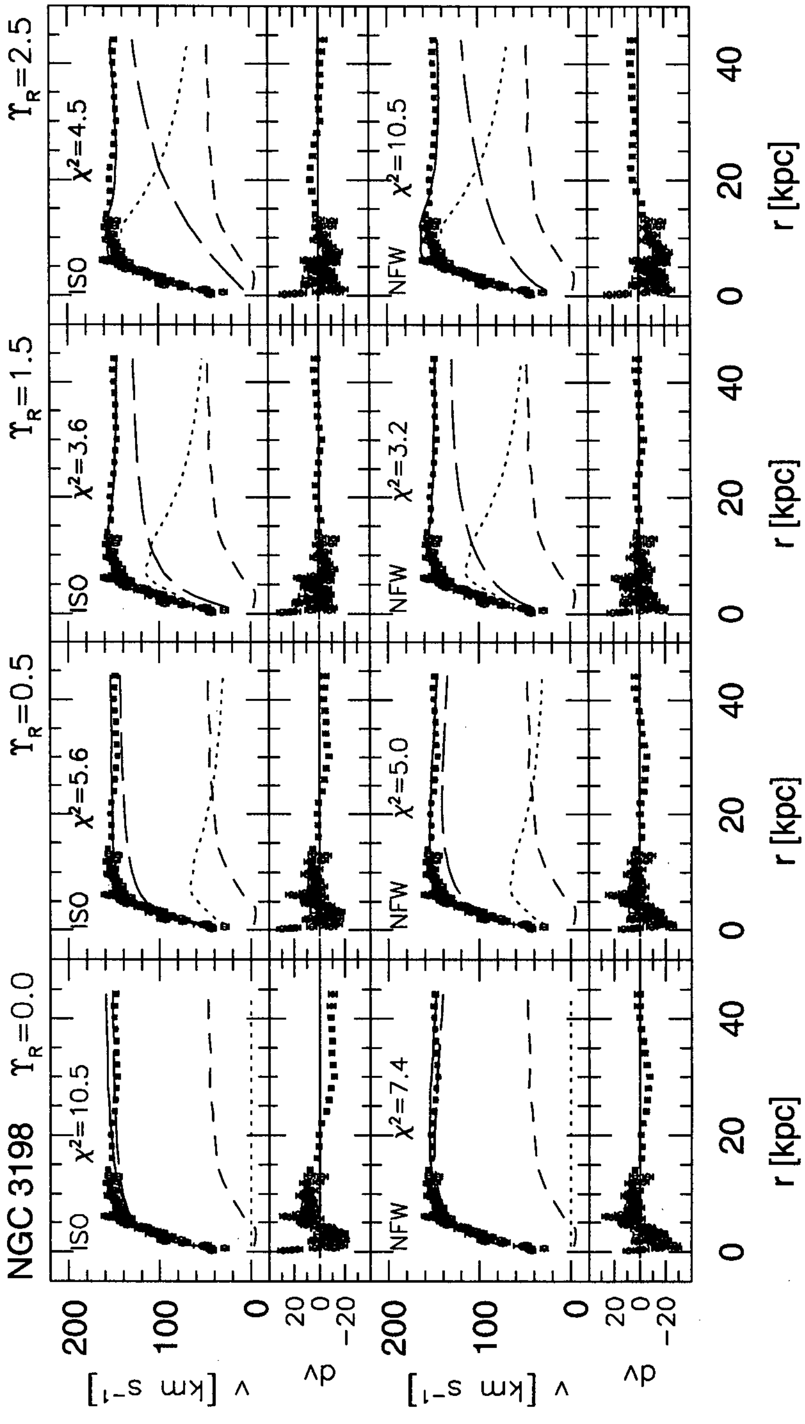

Figure 5.9: As Fig. (5.4), but for NGC 3198.

5.3 Best fit Dark Halo Shapes

The results shown in Figs. 5.4 & 5.5 confirm the finding of B01 that the rotation curves of IC 2574 and NGC 3109 cannot be reconciled with a NFW halo, while UGC 2259 (Fig. 5.6) is marginal. To quantify this, we extend our analysis by fitting a more general cuspy profile parameterized by α (see Eq. 2.40) to determine the range of α. As we describe in §5.4, strong correlations between α, M/L, and c exist. Hence we fix two of these parameters in the ranges $0 \leq \alpha \leq 2$ and $0 \leq M/L \leq (M/L)_{\mathrm{max}}$, and perform a 2-parameter fit with (c, v_{200}) for the halo. We compute these fits with minimum errors of 1 $\mathrm{km\,s^{-1}}$. The results of these fits are plotted in Fig. 5.10 and summarized in Table 5.4. Note that we do not give error bars on the best fitting α as these depend on the definition of the rotation curve errors.

B00 claimed that the best fit α increases with maximum rotation velocity v_{max}. Here we show that it is the maximum allowed α that increases with v_{max} (and also with luminosity M_{B}), as the best fit α depends on the $(M/L)_{\mathrm{disk}}$. For a maximum-disk fit all galaxies in this analysis favour $\alpha = 0$; as $(M/L)_{\mathrm{disk}}$ decreases, the best fit α increases with the highest α usually occuring for $(M/L)_{\mathrm{disk}} = 0$.

As is found in previous studies, none of these galaxies can be well fitted with a MOORE halo profile ($\alpha = 1.5$), however, due to the uncertainty in the definition of rotation curve error bars we cannot place a statistical significance to this.

Galaxy	M_B [mag]	v_{max} [$\mathrm{km\,s^{-1}}$]	α_{max}	α_{min}
NGC 3109	-16.35	67	0.0	0.0
IC 2574	-16.77	67	0.5	0.0
UGC 2259	-17.03	90	0.0	0.0
NGC 5585	-17.50	92	1.0	0.0
NGC 2403	-19.50	132	1.3	0.0
NGC 3198	-19.90	157	1.0	0.0

Table 5.4: Maximum and minimum values of the best fitting α.

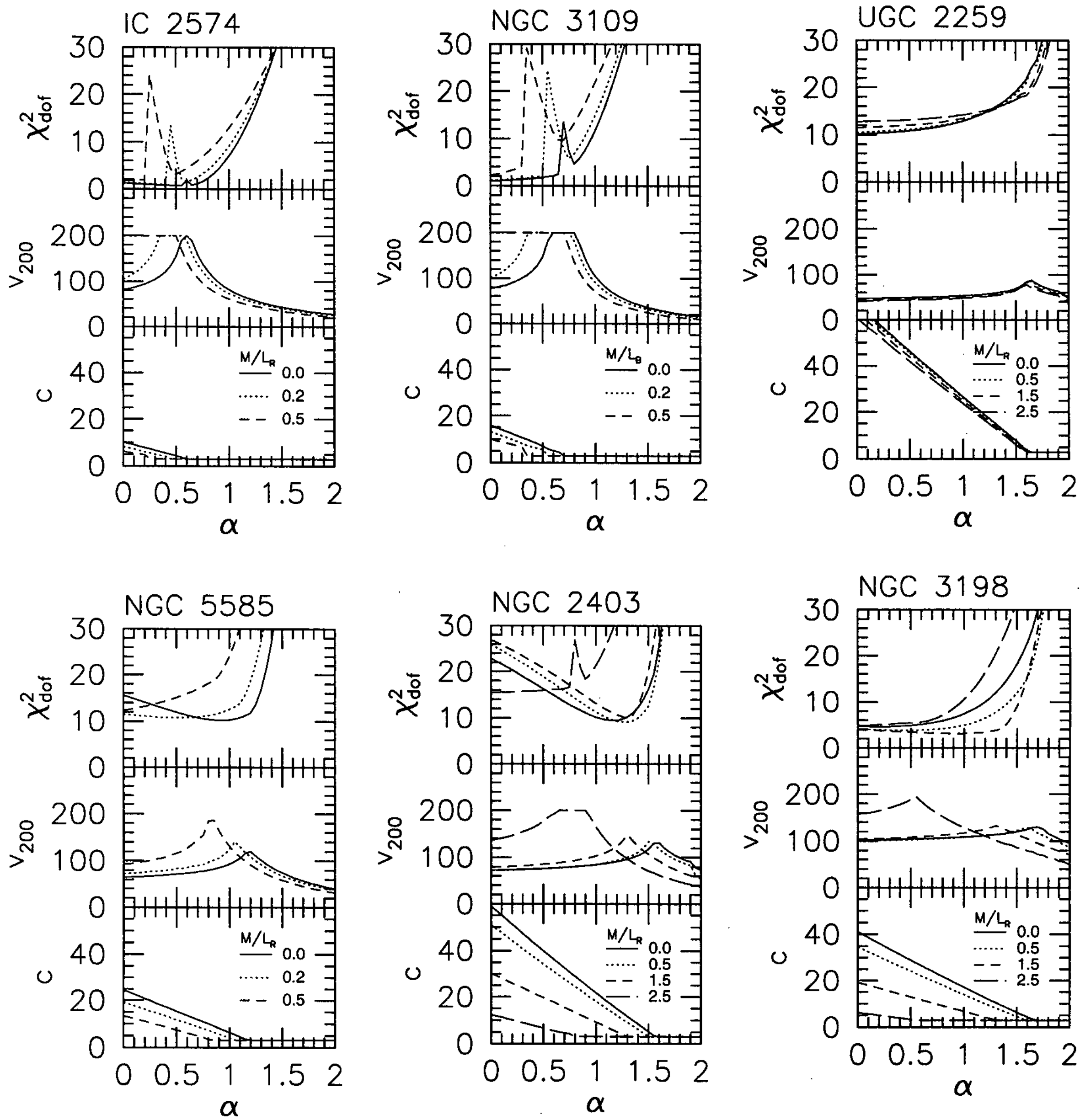

Figure 5.10: Reduced χ^2 and halo parameters vs. α for a full range of M/L. Note: $\alpha = 1$ is the NFW profile, while $\alpha = 1.5$ is the MOORE profile. The spikes in the χ^2 are due to an upper limit of $v_{200} < 200\,\mathrm{km\,s^{-1}}$ being enforced. When a lower limit of $c > 3$ is enforced the χ^2 also increases, but more smoothly.

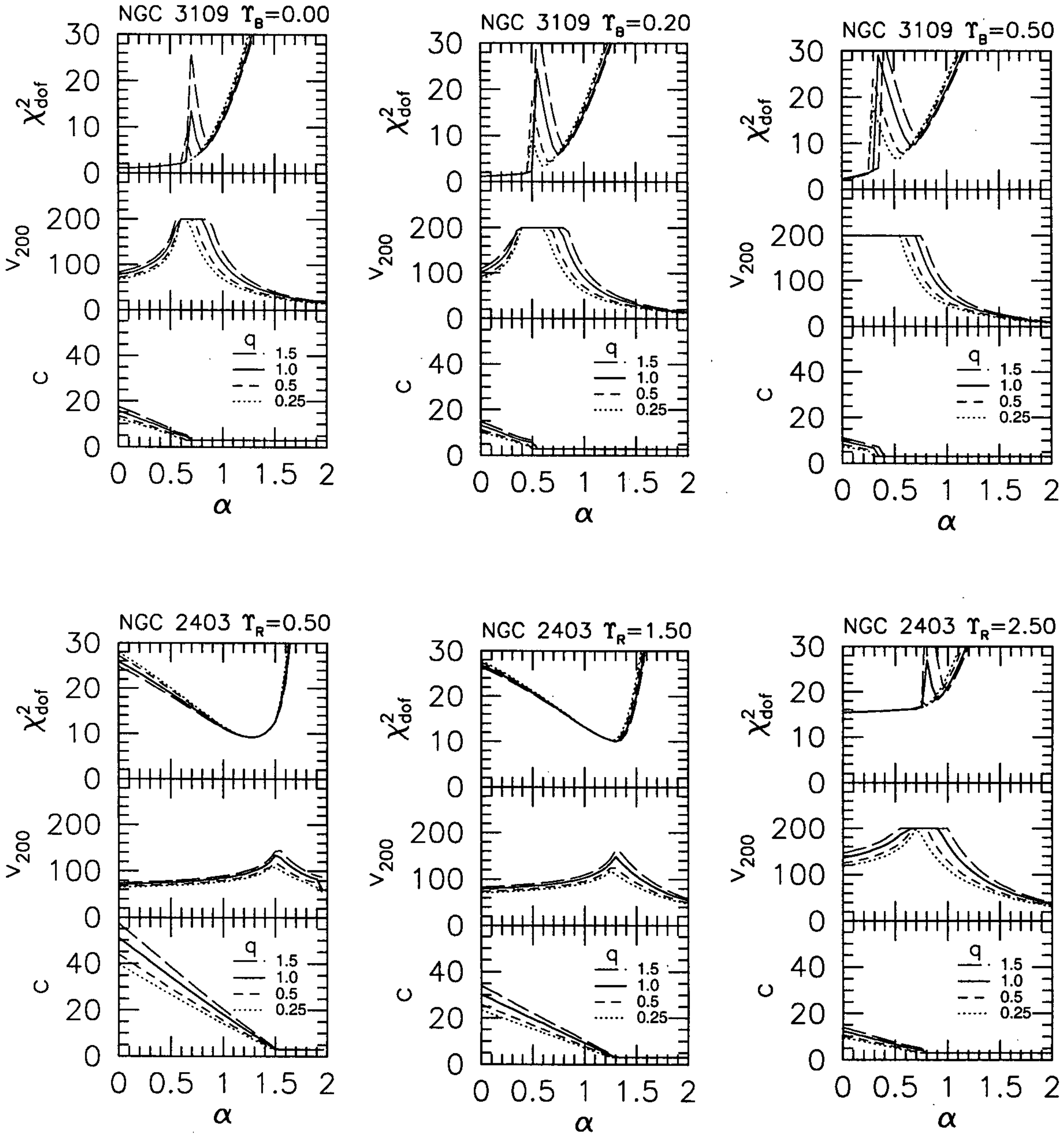

Figure 5.11: Reduced χ^2 and halo parameters vs. α for a range of q, and M/L. A spherical halo is $q = 1$, while $q > 1$ is prolate and $q < 1$ is oblate.

5.3.1 Effect of Oblate/Prolate Halos

For a given V_{200} and c, an oblate halo will result in a higher rotation velocity with a steeper rise, while for a prolate halo the reverse is expected. Thus we can reduce the steepness of the rising part of the halo rotation curve by increasing the halo flattening parameter, q, though in practice the effect on the rotation curve is small for realistic values of q (see Fig. 2.9).

We follow the same procedure as before, fixing α and M/L but now with $0.25 \leq q \leq 1.5$. Fig. 5.11, shows that the value of q has a minimal effect on χ^2, and only alters the range of best fitting α by 0.1 or less, though the best fitting halo parameters c and v_{200} can change significantly for fit as we go from $q = 0.25$ to $q = 1.5$.

5.3.2 Effect of Adiabatic Contraction

Adiabatic contraction will enhance the cuspiness of the halo and thus yield lower α for the initial non-contracted halo (assuming the same M/L). The effects of adiabatic contraction increase as a function of baryon fraction. For halos with minimal disks, adiabatic contraction has an insignificant effect on the halo density profile and hence rotation curve. The effect can be significant for higher $(M/L)_{\rm disk}$, until the baryons dominate the mass fraction (within a given radius) and the adiabatic approximation breaks down. Fig. 5.12 shows a comparison between ISO, NFW and ALP halo fits with (dotted lines) and without (solid line) adiabatic contraction for NGC 2403. For low $M/L_{\rm R} \sim 0.5$ the ISO and NFW fits are slightly improved by contraction, though for larger $M/L_{\rm R}$ values the χ^2 rapidly increases. At $M/L_{\rm R} \sim 1.5$, the favoured sub-maximal disk value for NGC 2403, all models with a contracted halo provide a poor fit to the data. This illustrates the impact baryons can have on the dark matter distribution.

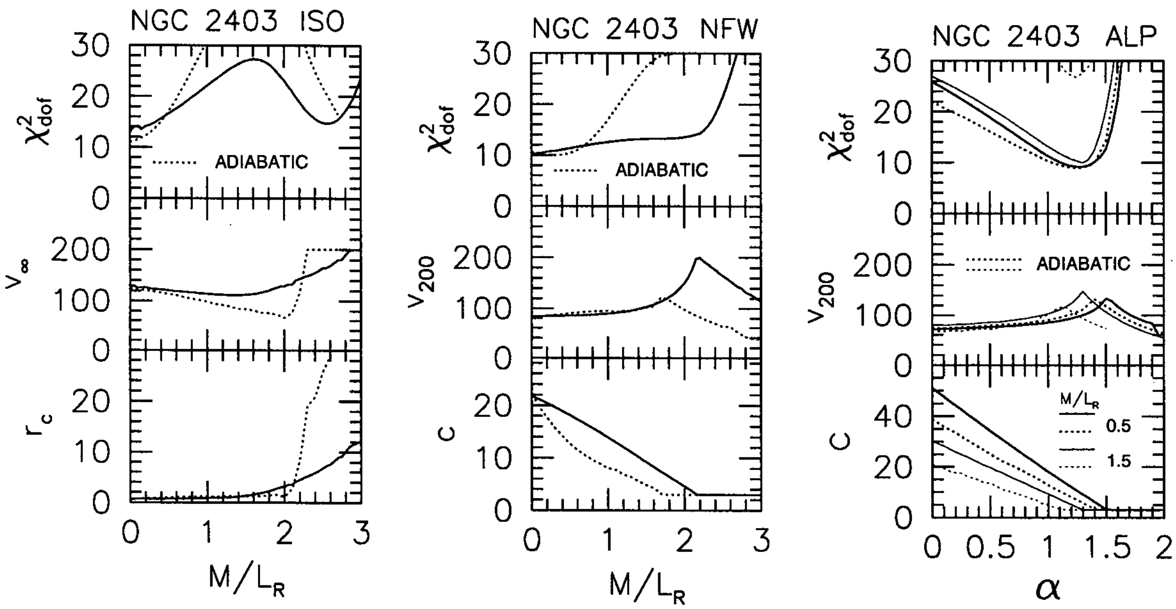

Figure 5.12: Effect of adiabatic contraction on ISO (left), NFW (middle), and ALP (right) halos for NGC 2403. The dotted and solid lines represent mass models with and without adiabatic contraction respectively.

5.4 Model Degeneracies

As discussed in §5.3 degeneracies exist between the model parameters, which prevent a unique mass decomposition. We illustrate these degeneracies in Fig. 5.13 for fits with fixed values of $(M/L)_{\rm disk}$, α, and c for NGC 5585, NGC 2403, and NGC 3198 respectively. The degeneracies exist to a greater or lesser extent for all these galaxies, so these 3 examples are not exhaustive or unique. The degeneracies are not perfect, as the χ^2's for the fits shown here are slightly larger than the best χ^2's for each galaxy, however, these differences are not statistically significant.

In Fig. 5.13 the r and v axes have been scaled by the scale length of the disk, h, and the maximum rotation velocity, $v_{\rm max}$, for each galaxy respectively. The galaxies have been ordered in increasing $v_{\rm max}$ from left to right. With these dimensionless axes we can see that the higher the $v_{\rm max}$, the steeper the rise of the rotation curve. Due to the degeneracy between $(M/L)_{\rm disk}$ and the halo parameters α, c, and v_{200} we are unable to determine whether this trend is caused by an increasing stellar component, or a more cuspy dark halo. This degeneracy is illustrated with NGC 2403 for fixed α and NGC 3198 for fixed c. To break this degeneracy we need to know $(M/L)_{\rm disk}$ and the distance to the galaxy. If the disk and halo thicknesses are ignored, this fixes the density profile of the dark halo.

However, because of degeneracies between the halo parameters in many cases, we are unable to distinguish between density profiles with cusps ($\alpha \simeq 1$) from those with cores ($\alpha \simeq 0$). This degeneracy is illustrated for NGC 5585. To break this degeneracy we need a further constraint on c or v_{200}. For $\alpha \simeq 1$, we can apply the correlation between c and v_{200} found in N-body simulations, which should allow us to determine if the NFW profile is consistent with the data. For bright galaxies we can apply the constraint on v_{200} from lensing and Tully Fisher analyses (see §2.5.3), we attempt this in the following section.

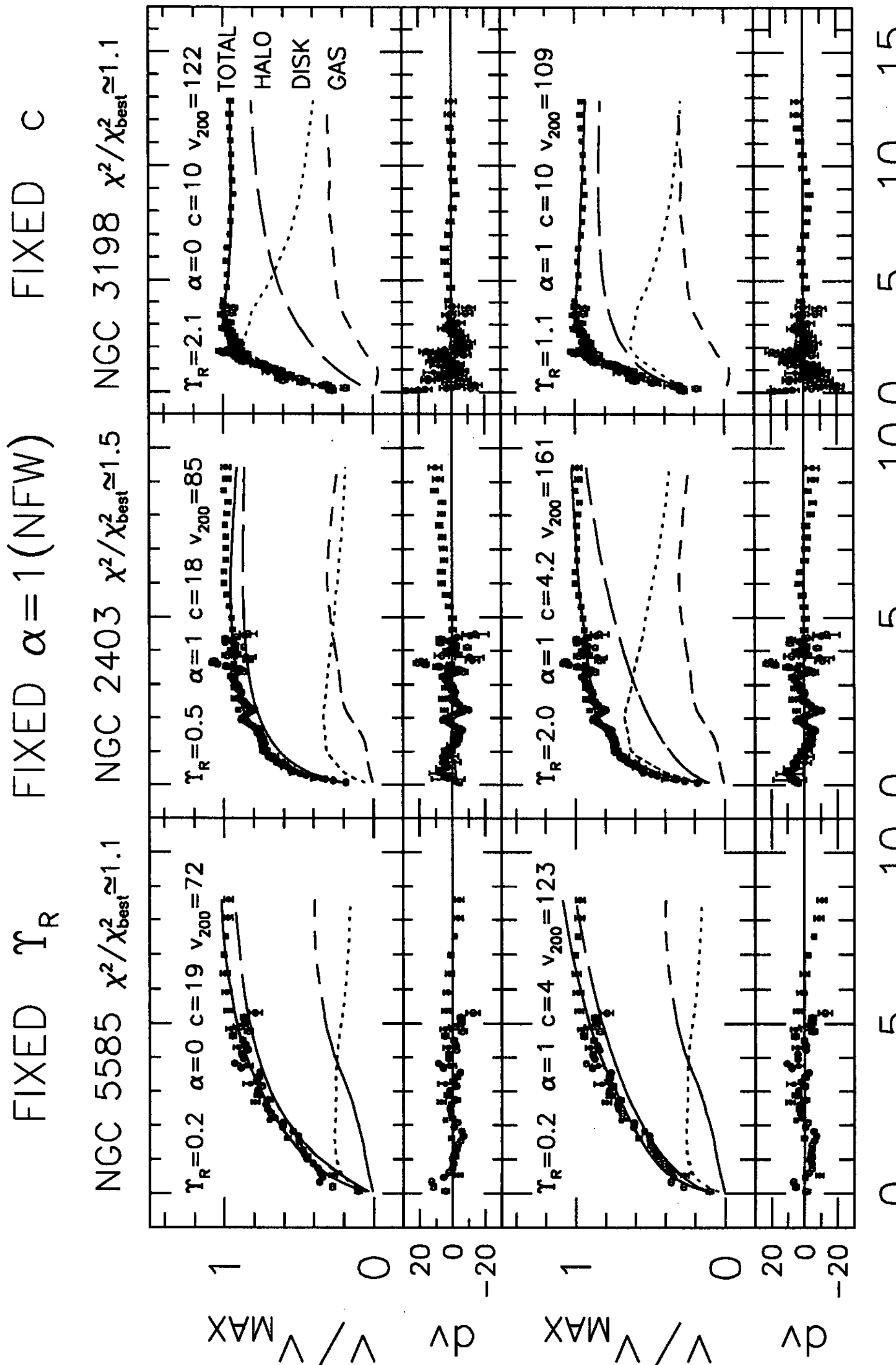

Figure 5.13: Illustration of model degeneracies with NGC 5585, NGC 2403 and NGC 3198.

5.5 Fits with M/L Constraints

The galaxies NGC 2403 and NGC 3198 are massive enough to warrant application of the lensing/TF constraints discussed in §2.5. From §5.3, we find that the best fit α increases if we apply the sub-maximal disk constraint: $v_{\rm disk}/v_{\rm tot} \simeq 0.6$ at 2.15 disk scale lengths. This corresponds to $M/L_{\rm R} \simeq 1.5$ for both of these galaxies, and requires a $B - R = 1.17$ (see Fig 2.12). Accurate colours are still not available for these galaxies, though for late-type spirals this value is reasonable (Bell & de Jong 2001).

We now impose the additional constraint that $v_{\rm disk}(2.15R_{\rm d}) \simeq v_{\rm tot}(r_{200})$. By fixing $M/L_{\rm R} = 1.5$, this equation fixes $v_{\rm halo}(r_{200})$, and we are left with a 1-parameter fit for the halo! Much of the appeal of this approach is that it reduces the mass decomposition to a single parameter. However, for both galaxies, we are unable to produce a satisfactory fit with these constraints. The velocity data are significantly higher than the model in the flat outer part of the rotation curve. At the last measured data point, the discrepancy is $\sim 20\,{\rm km\,s^{-1}}$ for NGC 2403 and $\sim 15\,{\rm km\,s^{-1}}$ for NGC 3198 (see Fig. 5.14).

A number of alternatives can be invoked to explain this discrepancy, such as, a greater contribution of the gas and disk to the overall potential inside the last measured rotation curve data point, or a modification of the halo profile such as a steeper than r^{-3} fall-off at large radii. However, the simplest explanation is that the assumption that *all* galaxies have sub-maximal disks at $2.15R_{\rm d}$ with $v_{\rm disk}/v_{\rm tot} \simeq 0.6$ and $v_{\rm tot}(2.15R_{\rm d}) \simeq 1.8v_{200}$ is not realistic. The latter (lensing) constraint is probably the most inadequate of the two. It will be interesting to see what role this constraint plays with a more careful treatment of the stellar contribution. With colour-corrected stellar disk mass profiles, and bulge-to-disk decompositions, the shape of the stellar rotation curve could change.

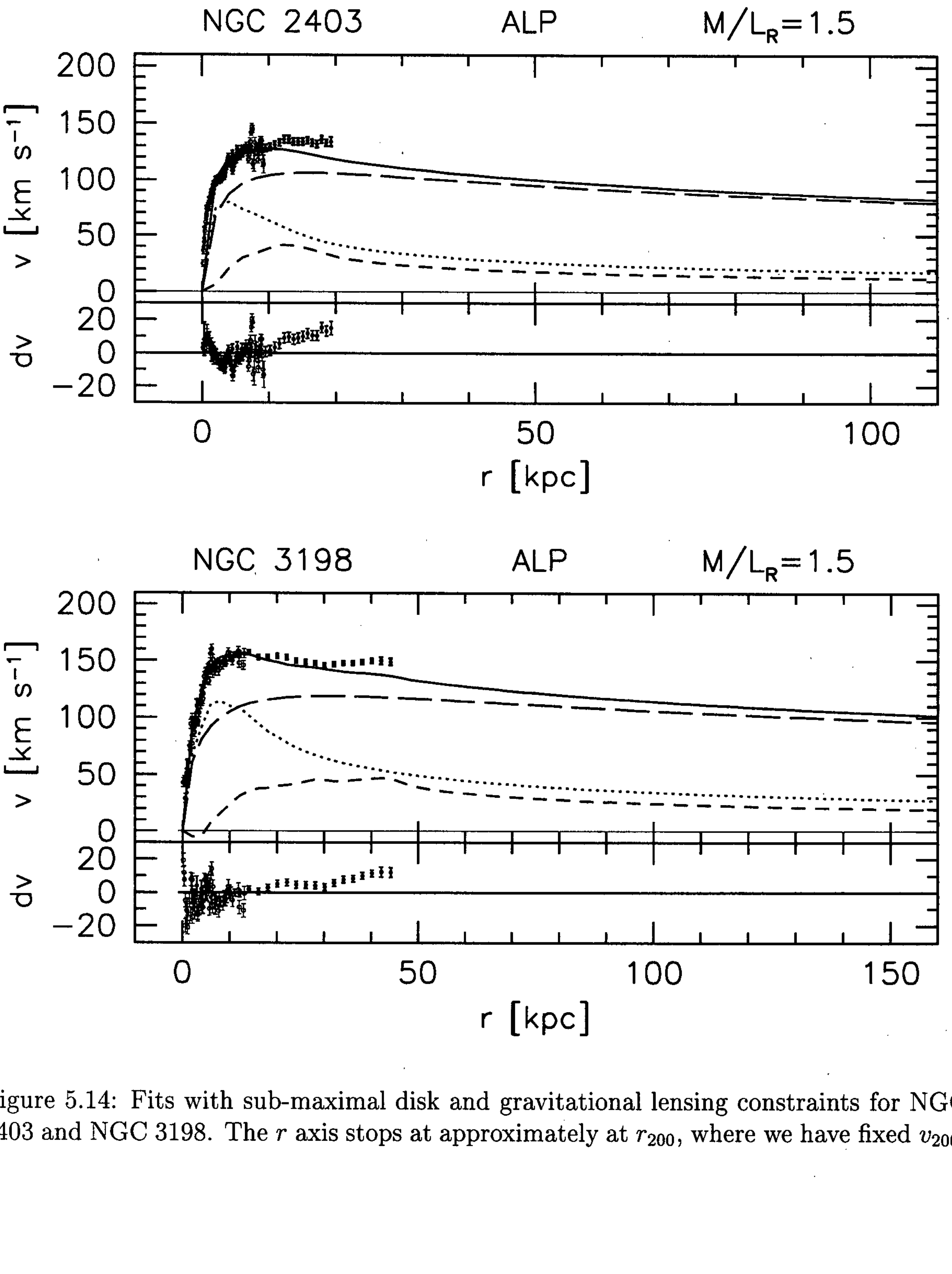

Figure 5.14: Fits with sub-maximal disk and gravitational lensing constraints for NGC 2403 and NGC 3198. The r axis stops at approximately at r_{200}, where we have fixed v_{200}.

Chapter 6

Discussion and Conclusions

There is an ongoing debate on whether the rotation curves of spiral galaxies, especially the dwarf and low surface brightness types, are consistent with numerical simulations of a cold dark matter Universe. In a landmark paper, De Blok et al. (2001a) decomposed and analyzed the Hα and HI rotation curves of 29 LSB galaxies and concluded that the NFW profile is not a good description of the data. Rather, the inner rotation curves show a more solid-body like rise consistent with a central density core. In an analysis of *all* dwarf and LSB galaxies with high-resolution rotation curves studied to date, de Blok et al. (2001b) inverted the rotation curve into a mass density profile and fitted a power-law ($\rho(r) \propto r^{-\alpha}$) to the innermost points, finding $\alpha = 0.2 \pm 0.2$. In the latest study of this kind, Swaters et al. (2003) find a somewhat different result with $\sim 75\%$ of the galaxies being consistent with NFW ($\alpha = 1$). Further, they claim that when systematic errors are taken into account cusps as steep as $\alpha \simeq 1$ cannot be ruled out for the remaining $\sim 25\%$. However, they also note that most of their galaxies are equally or better fitted by halos with constant density cores. Thus, based on these studies, it still cannot be stated that CDM has been disqualified on the basis of rotation curve fits.

In an attempt to develop our own analysis we have obtained high-resolution Hα rotation curves and multi-wavelength optical and near-infrared imaging for a sample of 24 galaxies previously studied in HI by Broeils 1992. These data were collected by Courteau & de Jong at Steward Observatory for a sample that contains a full range of spiral galaxy morphological types and surface brightnesses.

To analyze these data we have developed a comprehensive rotation curve mass modeling code that synthesizes and improves upon current modeling techniques. Our code is based on a non-linear least squares (NLLS) Levenberg-Marquardt fitting routine and allows for 6 free parameters: the mass-to-light ratio of the disk, $(M/L)_{\rm disk}$; the central slope of the dark halo, α; the concentration of the dark halo, c; the virial velocity of the dark halo, v_{200}; the c/a axial ratio of the dark halo, q; and the fraction of gas in HI, $f_{\rm HI}$, (which we fix at 1.33). Other parameters, that are kept fixed, include: the distance to the galaxy; the thickness of the disk; and a minimum rotation curve error bar. Novel additions to our mass modeling technique include the adiabatic contraction of the dark halo and the possibility that the dark halo is oblate or prolate.

Ideally we would fit for all the parameters simultaneously, resulting in best fit parameters with standard deviations. In practice there are local minima in the parameter space and covariances between the model parameters that cause the standard deviations to be under-estimated. To find a global minimum we use a grid search by fixing $(M/L)_{\rm disk}$, α, and q; this leaves a 2 parameter fit for the halo which we compute using a NLLS algorithm. An alternative approach would be to use Genetic-type Algorithms (GA) (e.g. Charbonneau 1995) that generate a new population of trial solutions by breeding the better solutions of the previous population. The advantage of GA over NLLS is that they find the global minimum, inside a specified parameter space, and do not require an initial guess. The disadvantage of GAs is they do not provide any information on the standard deviations of the fitted parameters. A common approach to this problem is to feed the final GA solution into a NLLS package to compute the covariance matrix and hence standard deviations. Our grid search method gives us this and more; not only does it give us the best fit and covariance matrix, it tells us about the global topology of the parameter space, and hence a better understanding of the allowed ranges of the model parameters than are encoded in standard deviations.

In this thesis we test our code extensively on 6 galaxy mass modeling "standards", most recently studied by Blais-Ouellette et al. (2001). We plan to return to the Steward Observatory data once our modeling technique has been satisfactorily calibrated.

To make a firm statement on the absolute goodness-of-fit of a model to the data it is crucial to understand the errors that can affect the rotation curve. These consist of: Statistical errors in measuring the velocity in a given radial bin; Systematic errors in measuring the velocity, such as beam smearing and long-slit position error; Non-circular motions that perturb the underlying galaxy potential such as from spiral arms, bars, substructure, warps and tidal effects of interactions; Radial variations in $(M/L)_{\rm disk}$ and $f_{\rm HI}$; To correct or rule out non-circular motions, 2D velocity fields and more detailed modeling are needed. At present we cannot quantify these systematic errors, since we do not have the original data, thus at best we can discuss the relative merit of one model against another for a given galaxy.

We have confirmed the finding of Blais-Ouellette (2001) that IC 2574 and NGC 3109 are seemingly incompatible with NFW halos, though without understanding the rotation curve errors we cannot place a statistical significance to this. The Hα rotation curves used in our study were derived from 2D Fabry-Perot velocity fields, and as such are not affected by many of the systematic problems that were raised by Swaters et al. (2003), such as beam smearing and slit position error. However, these galaxies require uncharacteristically low $(M/L)_{\rm disk}$ for good ISO or $\alpha = 0$ fits. However, since we have not corrected the surface brightness profiles for inclination or extinction and without having near IR imaging, we cannot determine if these $(M/L)_{\rm disk}$ values are in conflict with stellar population synthesis (SPS) models.

Blais-Ouellette (2000) found a trend between α and the maximum rotation velocity of the galaxy, $v_{\rm max}$, with larger rotators having steeper cusps. We confirm the possibility of a trend but for $\alpha_{\rm max}$ (the maximum realistic inner halo slope) with $v_{\rm max}$, as all the galaxies studied here are consistent with $\alpha = 0$ for suitable $(M/L)_{\rm disk}$. There is a degeneracy between α and $(M/L)_{\rm disk}$, such that even if $(M/L)_{\rm disk}$ is known, there often remains a degeneracy between the halo parameters c, v_{200} and α. To break all degeneracies we need $(M/L)_{\rm disk}$ constraints from SPS models and constraints on c or v_{200}, such as those from N-body simulations (this strictly applies to $\alpha \simeq 1$ only, as halos with $\alpha \simeq 0$ are not found in N-body simulations).

As an alternative to applying SPS models to constrain $(M/L)_{\rm disk}$, several independent techniques suggest that bright spiral galaxies have, on average, sub-maximal disks with $v_{\rm disk} \simeq 0.6 v_{\rm opt}$ (e.g. Bottema 1993, 1999; Mo, Mao & White 1998; Courteau & Rix 1999; Trott & Webster 2002). NGC 2403 and NGC 3198 are bright enough to warrant applying this constraint. The sub-maximal disk constraint implies $M/L_{\rm R} \simeq 1.5$ for both galaxies, yielding best fit $\alpha \simeq 1.3$ and $\alpha \simeq 1$ for NGC 2403 and NGC 3198 respectively. A further constraint, from gravitational lensing, that $v_{\rm opt} \simeq 1.8 v_{\rm tot}(r_{200})$ for bright galaxies (Seljak 2002) can be applied to these 2 galaxies. However, in both cases, the model under-predicts the flat outer part of the rotation curve, suggesting that the halo density profile should decline faster than r^{-3} or that the lensing constraint is not very tight.

Previous studies have assumed the halo to be spherical, though it has been known for over a decade that pure DM N-body simulations generate triaxial halos (Dubinski 1991; Jing & Suto 2002). When baryons are included, simulations tend to generate oblate halos (Katz & Gunn 1991; Dubinski 1994) in agreement with observations (see F. Combes 2002 and references therein). For simplicity we have assumed that the halo is axially symmetric (defining the c/a axial ratio as q), and that the disk and halo are aligned. If either of these assumptions are broken, the orbits of the stars and gas in the disk may not be circular, and the extraction of a rotation curve from the velocity field is greatly complicated. We find the effect of q is insignificant on the goodness-of-fit, since the halo parameters can be adjusted to compensate. However, if we constrain c and v_{200}, we must exercise care since their definition depends on q.

Finally, we have explored the effects of adiabatic contraction. This is a prescription for modeling the effect on the halo density profile of the slow contraction of the baryons that settle into a disk. Adiabatic contraction increases the cuspiness of the halo, with the effect increasing with baryon fraction. For minimum disks the effect is insignificant (as expected), but for larger $(M/L)_{\rm disk}$ the goodness-of-fit and model parameters can be substantially altered. For example without adiabatic contraction NGC 2403 is well fitted with an NFW halo and a disk with $M/L_{\rm R} < 2.2$, though when adiabatic contraction is applied $M/L_{\rm R} < 0.8$ for NFW halos, which rules out the favoured sub-maximal disk $M/L_{\rm R} \simeq 1.5$. However, to apply adiabatic contraction we need to specify the initial distribution of baryons. It is usually assumed that the baryons are initially mixed with the dark matter though this strictly applies only to monolithic collapse models. In a Universe where structure forms hierarchically the merger history of the dark halo needs to be considered, such as done in semi-analytic models of galaxy formation (e.g. Somerville & Primack, 1999).

Aside from adiabatic infall there are other mechanisms by which baryons can alter the dark matter profile, such as stellar feedback and stellar bars, though these are less clearly understood. Studies that ignore these effects cannot make a fair comparison between density profiles found in N-body simulations (e.g. NFW) and observations, unless the galaxy is dominated by dark matter at all radii (as is suspected for LSB galaxies).

In summary, in order to obtain accurate mass models of spiral galaxies from rotation curves we need:

- Galaxy images and 2D velocity fields with well-defined centres;
- High-quality optical and radio rotation curves with well-defined errors;
- Accurate stellar mass-to-light ratios from SPS models based on near-IR and optical

photometry;

- Improved understanding of the impact of baryons on the distribution of dark matter in galaxies;
- Tight constraints on c and v_{200} from N-body simulations.
- Minimization techniques that do not strictly rely on a global χ^2 statistic.

The most crucial of these is to understand (or model) the errors in the rotation curve data. This is the approach we intend to follow in our continuing study.

Bibliography

[1] Abramowitz, M. & Stegun, I. A. 1972, Handbook of Mathematical Functions, New York: Dover, 1972

[2] Begeman, K. G. 1987, Ph.D. thesis, Kapteyn Institute

[3] Begeman, K. G. 1989, AAP, 223, 47

[4] Bell, E. F. & de Jong, R. S. 2001, ApJ, 550, 212

[5] Bertschinger, E. 1985, ApJS, 58, 39

[6] Binney, J. & Tremaine, S. 1987, Princeton, NJ, Princeton University Press,

[7] Blais-Ouellette, S. 2000, PhD Thesis

[8] Blais-Ouellette, S., Amram, P., & Carignan, C. 2001, AJ, 121, 1952

[9] Blumenthal, G. R., Faber, S. M., Flores, R., & Primack, J. R. 1986, ApJ, 301, 27

[10] Bolatto, A. D., Simon, J. D., Leroy, A., & Blitz, L. 2002, ApJ, 565, 238

[11] Bosma, A. 1978, PhD Thesis, Groningen Univ.

[12] Bosma, A. 1981, AJ, 86, 1791

[13] Bottema, R. 1993, AAP, 275, 16

[14] Broeils, A. H. 1992, PhD thesis, Univ. Groningen

[15] Broeils, A. H. & Courteau, S. 1997, ASP Conf. Ser. 117: Dark and Visible Matter in Galaxies and Cosmological Implications, 74

[16] Bullock, J. S., Dekel, A., Kolatt, T. S., Kravtsov, A. V., Klypin, A. A., Porciani, C., & Primack, J. R. 2001, ApJ, 555, 240

[17] Carignan, C. 1985, ApJ, 299, 59

[18] Carignan, C. & Freeman, K. C. 1988, ApJL, 332, L33

[19] Carignan, C., Sancisi, R., & van Albada, T. S. 1988, AJ, 95, 37

[20] Carignan, C. & Beaulieu, S. 1989, ApJ, 347, 760

[21] Casertano, S. 1983, MNRAS, 203, 735

[22] Charbonneau, P. 1995, ApJS, 101, 309

[23] Cole, S. & Lacey, C. 1996, MNRAS, 281, 716

[24] Combes, F. 2002, New Astronomy Review, 46, 755

[25] Corradi, R. L. M., Boulesteix, J., Bosma, A., Amram, P., & Capaccioli, M. 1991, AAP, 244, 27

[26] Côté, S., Carignan, C., & Sancisi, R. 1991, AJ, 102, 904

[27] Côté, S., Carignan, C., & Freeman, K. C. 2000, AJ, 120, 3027

[28] Courteau, S. & Faber, S. M. 1988, PASP, 100, 1219

[29] Courteau, S. 1996, ApJS, 103, 363

[30] Courteau, S. & Rix, H. 1999, ApJ, 513, 561

[31] Courteau, S., et al. 2003 in preparation

[32] Dalcanton, J. J., Spergel, D. N., & Summers, F. J. 1997, ApJ, 482, 659

[33] de Blok, W. J. G., McGaugh, S. S., & van der Hulst, J. M. 1996, MNRAS, 283, 18

[34] de Blok, W. J. G. & McGaugh, S. S. 1997, MNRAS, 290, 533

[35] de Blok, W. J. G., McGaugh, S. S., & Rubin, V. C. 2001a, AJ, 122, 2396

[36] de Blok, W. J. G., McGaugh, S. S., Bosma, A., & Rubin, V. C. 2001b, ApJL, 552, L23

[37] de Blok, W. J. G. & Bosma, A. 2002, AAP, 385, 816

[38] de Grijs, R., Peletier, R. F., & van der Kruit, P. C. 1997, AAP, 327, 966

[39] Dubinski, J. & Carlberg, R. G. 1991, ApJ, 378, 496

[40] Dubinski, J. 1994, ApJ, 431, 617

[41] Eisenstein, D. J. & Loeb, A. 1996, ApJ, 459, 432

[42] Flores, R., Primack, J. R., Blumenthal, G. R., & Faber, S. M. 1993, ApJ, 412, 443

[43] Flores, R. A. & Primack, J. R. 1994, ApJL, 427, L1

[44] Freedman, W. L. et al. 2001, ApJ, 553, 47

[45] Freeman, K. C. 1970, ApJ, 160, 811

[46] Fukushige, T. & Makino, J. 1997, ApJL, 477, L9

[47] Fukushige, T. & Makino, J. 2001, ApJ, 557, 533

[48] Ghigna, S., Moore, B., Governato, F., Lake, G., Quinn, T., & Stadel, J. 2000, ApJ, 544, 616

[49] Gnedin, O. Y. & Zhao, H. 2002, MNRAS, 333, 299

[50] Gradshteyn, I. S. & Ryzhik, I. M. 1980, New York: Academic Press, 1980, 5th corr. and enl. ed.

[51] Hayashi, E., Navarro, J. F., Taylor, J. E., Stadel, J., Quinn, T. astro-ph/0203004

[52] Hinshaw, G., et al. astro-ph/0302217, ApJ in press

[53] Huss, A., Jain, B., & Steinmetz, M. 1999, MNRAS, 308, 1011

[54] Jaffe, A. H. et al. 2001, Physical Review Letters, 86, 3475

[55] Jesseit, R., Naab, T., & Burkert, A. 2002, ApJL, 571, L89

[56] Jimenez, R., Verde, L., Oh, S. P. astro-ph/0201352

[57] Jing, Y. P. & Suto, Y. 2000, ApJL, 529, L69

[58] Jing, Y. P. & Suto, Y. 2002, ApJ, 574, 538

[59] Jobin, M. & Carignan, C. 1990, AJ, 100, 648

[60] Katz, N. & Gunn, J. E. 1991, ApJ, 377, 365

[61] Kent, S. M. 1985, ApJS, 59, 115

[62] Kent, S. M. 1986, AJ, 91, 1301

[63] Kent, S. M. 1987, AJ, 93, 816

[64] Kent, S. M. 1988, AJ, 96, 514

[65] Klypin, A., Kravtsov, A. V., Valenzuela, O., & Prada, F. 1999, ApJ, 522, 82

[66] Klypin, A. astro-ph/0005504

[67] Kregel, M., van der Kruit, P. C., & de Grijs, R. 2002, MNRAS, 334, 646

[68] Lahav, O. et al. 2002, MNRAS, 333, 961

[69] Mac Low, M. & Ferrara, A. 1999, ApJ, 513, 142

[70] Maller, A. H., Simard, L., Guhathakurta, P., Hjorth, J., Jaunsen, A. O., Flores, R. A., & Primack, J. R. 2000, ApJ, 533, 194

[71] Mao, S., Mo, H. J., & White, S. D. M. 1998, MNRAS, 297, L71

[72] Marchesini, D., D'Onghia, E., Chincarini, G., Firmani, C., Conconi, P., Molinari, E., & Zacchei, A. 2002, ApJ, 575, 801

[73] Martimbeau, N., Carignan, C., & Roy, J.-R. 1994, AJ, 107, 543

[74] McGaugh, S. S. & de Blok, W. J. G. 1998, ApJ, 499, 41

[75] McGaugh, S. S., Rubin, V. C., & de Blok, W. J. G. 2001, AJ, 122, 2381

[76] Merrifield, M. R. 2002 in 'The shapes of Galaxies and their Halos' Yale, May 2001, ed. World Scientific (astro-ph/0107291)

[77] Mo, H. J., Mao, S., & White, S. D. M. 1998, MNRAS, 295, 319

[78] Moore, B. 1994, Nature, 370, 629

[79] Moore, B., Governato, F., Quinn, T., Stadel, J., & Lake, G. 1998, ApJL, 499, L5

[80] Moore, B., Ghigna, S., Governato, F., Lake, G., Quinn, T., Stadel, J., & Tozzi, P. 1999a, ApJL, 524, L19

[81] Moore, B., Quinn, T., Governato, F., Stadel, J., & Lake, G. 1999b, MNRAS, 310, 1147

[82] Moore, B. astro-ph/0009247

[83] Navarro, J. F., Eke, V. R., & Frenk, C. S. 1996, MNRAS, 283, L72

[84] Navarro, J. F., Frenk, C. S., & White, S. D. M. 1996, ApJ, 462, 563

[85] Navarro, J. F., Frenk, C. S., & White, S. D. M. 1997, ApJ, 490, 493

[86] Navarro, J. F. & Steinmetz, M. 1997, ApJ, 478, 13

[87] Navarro, J. F. & Steinmetz, M. 2000, ApJ, 528, 607

[88] Peacock, J. A. et al. 2001, Nature, 410, 169

[89] Phillips, J., Weinberg, D. H., Croft, R. A. C., Hernquist, L., Katz, N., & Pettini, M. 2001, ApJ, 560, 15

[90] Press, W. H. & Schechter, P. 1974, ApJ, 187, 425

[91] Press, W. H., Teukolsky, S. A., Vetterling, W. T., & Flannery, B. P. 1992, 'Numerical Recipies' Cambridge: University Press, —c1992, 2nd ed.,

[92] Primack, J. R. astro-ph/0205391

[93] Rix, H. & Zaritsky, D. 1995, ApJ, 447, 82

[94] Rubin, V. C., Thonnard, N., & Ford, W. K. 1978, ApJL, 225, L107

[95] Rubin, V. C., Thonnard, N., & Ford, W. K. 1980, ApJ, 238, 471

[96] Ryden, B. S. & Gunn, J. E. 1987, ApJ, 318, 15

[97] Ryden, B. S. 1988, ApJ, 329, 589

[98] Ryden, B. S. 1991, ApJ, 370, 15

[99] Seljak, U. 2002, MNRAS, 334, 797

[100] Somerville, R. S. & Primack, J. R. 1999, MNRAS, 310, 1087

[101] Spitzer, L. J. 1942, ApJ, 95, 329

[102] Swaters, R. A. 1999, Ph.D. thesis, Rijksuniversiteit Groningen

[103] Swaters, R. A., Madore, B. F., & Trewhella, M. 2000, ApJL, 531, L107

[104] Swaters, R. A., Madore, B. F., van den Bosch, F. C., & Balcells, M. astro-ph/0210152, ApJ in press

[105] Taylor, J. E. & Navarro, J. F. 2001, ApJ, 563, 483

[106] Tinker, J. L., Ryden, B. S. astro-ph/0209165

[107] Trott, C. M. & Webster, R. L. 2002, MNRAS, 334, 621

[108] Valenzuela, O., Klypin, A. astro-ph/0204028

[109] van Albada, T. S., Bahcall, J. N., Begeman, K., & Sancisi, R. 1985, ApJ, 295, 305

[110] van Albada, T. S. & Sancisi, R. 1986, (Royal Society Discussion on Material Content of the Universe, London, England, Oct. 23, 24, 1985) Royal Society (London), Philosophical Transactions, Series A, 320, p. 447-464.

[111] van den Bosch, F. C., Burkert, A., & Swaters, R. A. 2001a, MNRAS, 326, 1205

[112] van den Bosch, F. C. & Swaters, R. A. 2001b, MNRAS, 325, 1017

[113] van der Hulst, J. M., Skillman, E. D., Smith, T. R., Bothun, G. D., McGaugh, S. S., & de Blok, W. J. G. 1993, AJ, 106, 548

[114] van der Kruit, P. C. & Searle, L. 1981a, AAP, 95, 105

[115] van der Kruit, P. C. & Searle, L. 1981b, AAP, 95, 116

[116] van der Kruit, P. C. & Searle, L. 1982a, AAP, 110, 61

[117] van der Kruit, P. C. & Searle, L. 1982b, AAP, 110, 79

[118] van der Kruit, P. C. 1988, AAP, 192, 117

[119] Verde, L. et al. 2002, MNRAS, 335, 432

[120] Verheijen, M. A. W. 1997, PhD thesis, Univ. Groningen

[121] Vitvitska, M., Klypin, A. A., Kravtsov, A. V., Wechsler, R. H., Primack, J. R., & Bullock, J. S. 2002, ApJ, 581, 799

Appendix A

Intensity and Surface Brightness

Intensity (I) is the power radiated per unit area (A) and solid angle (Ω), or flux (F) per solid angle, expressed in physical units of $L_\odot\,\mathrm{pc}^{-2}$. Observationally the intensity relates to surface brightness, as

$$\mu^\lambda = -2.5\,\log I^\lambda + C^\lambda \tag{A.1}$$

where λ is the band-pass. Thus,

$$\mu^\lambda = m^\lambda + 2.5\,\log\,\Omega \tag{A.2}$$

where m^λ is the specific apparent magnitude and Ω is the solid angle in arcseconds. Using

$$\begin{aligned}
m^\lambda &= -2.5\,\log\frac{F^\lambda}{F^\lambda_\odot} + m_\odot, && \text{(A.3)}\\
F^\lambda &= \frac{L^\lambda}{4\pi d^2}, && \text{(A.4)}\\
\frac{\Omega\,(\mathrm{arcsec}^2)}{\Omega\,(\mathrm{radian})} &= \left(\frac{360\,60^2}{2\pi}\right)^2 = 206265^2,\ \text{and} && \text{(A.5)}\\
\Omega &= \frac{A}{4\pi d^2}, && \text{(A.6)}
\end{aligned}$$

substituting these into Eq. (A.2) gives

$$\mu^\lambda = -2.5\,\log\left(\frac{L^\lambda}{L^\lambda_\odot}\right) + 2.5\,\log\left(\frac{d}{d_\odot}\right) + m^\lambda_\odot + 2.5\,\log\left(206265^2\right) + 2.5\,\log\left(\frac{A}{4\pi d^2}\right). \tag{A.7}$$

The apparent magnitude of the Sun $m^\lambda_\odot$ and its distance $d_\odot$ can be replaced by its absolute magnitude $M^\lambda_\odot$, via

$$m^\lambda_\odot - M^\lambda_\odot = 5\,\log(d_\odot) - 5\,\log(\mathrm{pc}). \tag{A.8}$$

Substituting this into Eq. (A.7) gives,

$$\mu^{\lambda} = -2.5 \log\left(\frac{I^{\lambda}}{L_{\odot}^{\lambda}/\mathrm{pc}^2}\right) + 2.5 \log(206265^2) - 5 + M_{\odot}^{\lambda}. \tag{A.9}$$

Rearranging to give the intensity in $L_{\odot}^{\lambda}\,\mathrm{pc}^{-}2$ finally gives

$$I^{\lambda} = 206265^2 10^{(M_{\odot}^{\lambda} - 5 - \mu^{\lambda})/2.5}. \tag{A.10}$$

Appendix B

Surface Density and Rotation Curve for an Exponential Disk

The surface brightness profiles of many galaxies can be fitted to a straight line, as seen in Fig. (3.3), $\mu^\lambda = a + bR$. Expressed in terms of intensity, this corresponds to

$$I^\lambda(R) = I_0^\lambda \, e^{-R/R_\mathrm{d}}, \tag{B.1}$$

where R_d is the disk scale length and I_0 is the central intensity. Substituting this into Eq. (A.9) gives

$$\mu^\lambda = -2.5 \log I_0^\lambda + 2.5 \frac{R}{R_\mathrm{d}} \log(e) + 5 \, \log(206265) - 5 + M_\odot^\lambda \tag{B.2}$$

thus

$$\begin{aligned} a &= -2.5 \log I_0^\lambda + 5 \log(206265) - 5 + M_\odot^\lambda & \text{(B.3)} \\ \Rightarrow I_0^\lambda &= 206265^2 (M_\odot^\lambda - 5 - a)/2.5 & \text{(B.4)} \\ b &= 2.5 \log(e)/R_\mathrm{d} & \text{(B.5)} \\ \Rightarrow R_\mathrm{d} &= 2.5 \log(e)/b = 2.5/b \ln(10). & \text{(B.6)} \end{aligned}$$

By assuming that light traces mass we arrive at the surface density of an exponential disk,

$$\Sigma(R) = \Upsilon_\mathrm{disk}^\lambda \, I_0^\lambda \, e^{-R/R_\mathrm{d}}, \tag{B.7}$$

where $\Upsilon_\mathrm{disk}^\lambda$ is the mass-to-light ratio of the disk in pass band λ, and the central surface density $\Sigma_0 = \Upsilon_\mathrm{disk}^\lambda I_0^\lambda$.

The gravitational potential is found by solving Laplace's equation $\nabla^2\Phi = 0$, subject to appropriate boundary conditions on the disk and at infinity (Toomre 1962). Using cylindrical polar coordinates, one finds

$$\Phi(R,z) = \int_0^\infty S(k)\, J_0(kR)\, e^{-k|z|}\, dk \tag{B.8}$$

$$S(k) = -2\pi G \int_0^\infty J_0(kR)\, \Sigma(R)\, R\, dR, \tag{B.9}$$

where $S(k)$ is the Hankel transform of $-2\pi G\Sigma(R)$, and $J_o(kR)$ is the cylindrical Bessel function of order zero.

For the case of an exponential disk, Eq. (B.7), these integrals can be computed analytically (Freeman 1970), resulting in

$$S(k) = -\frac{2\pi G \Sigma_0 R_d^2}{[1+(kR^2)]^{\frac{3}{2}}}, \tag{B.10}$$

$$\Phi(R,0) = -\pi G \Sigma_o R[I_0(y)K_1(y) - I_1(y)K_0(y)], \tag{B.11}$$

$$v_{\text{disk}}(R)^2 = R\frac{\partial\phi}{\partial R} = 4\pi G\Sigma_0 R_{\text{d}}^2[I_0(y)K_0(y) - I_1(y)K_1(y)], \tag{B.12}$$

where I_n and K_n are modified Bessel functions of the first and second kinds and $y = \frac{R}{2R_{\text{d}}}$.

Appendix C

The Radial Force for an Axisymmetric Thick Disk

This appendix is largely a reproduction of the derivation by Casertano (1983). The gravitational potential Φ for an axisymmetric density distribution $\rho(r,z)$, in cylindrical coordinates r, θ, and z, is the solution of the Poisson equation,

$$\nabla^2 \Phi = 4\pi G \rho. \tag{C.1}$$

We take zero-order radial Fourier-Bessel (Hankel) transforms on both sides of Eq. (C.1)

$$-k^2 \tilde{\Phi}(k,z) + \frac{\partial^2}{\partial z^2} \tilde{\Phi}(k,z) = 4\pi G \tilde{\rho}(k,z) \tag{C.2}$$

where for any quantity $A(r)$ the Hankel transform $\tilde{A}(k)$ is defined as

$$\tilde{A}(k) = \int_0^\infty J_0(kr)\, A(k)\, k\, dk. \tag{C.3}$$

Eq. (C.2) is, for any value of k, a linear non-homogeneous ordinary differential equation. Its solution, found by standard (Greens Function) methods, is

$$\tilde{\Phi}(k,z) = -\frac{2\pi G}{k} \int_{-\infty}^{\infty} \exp(-k|z-\zeta|)\, \tilde{\rho}(k,\zeta)\, d\zeta, \tag{C.4}$$

where boundary conditions at infinity have been included. The solution, Eq. (C.4), is valid provided the density vanishes for $|z| \to +\infty$.

We are especially interested in evaluating the gravitational potential on the plane $z = 0$ for a density distribution that is symmetrical with respect to it. Therefore, we have

$$\tilde{\Phi}(k, z=0) = -\frac{4\,\pi\,G}{k}\int_0^\infty \tilde{\rho}(k,\zeta)\,\exp(-k\,\zeta)\,d\zeta. \tag{C.5}$$

Using the inversion formula Eq. (C.3) we obtain

$$\Phi(r, z=0) = -4\,\pi\,G\int_0^\infty J_o(kr)\left\{\int_0^\infty \tilde{\rho}(k,\zeta)\exp(-k\zeta)\,d\zeta\right\}\,dk. \tag{C.6}$$

The radial force is

$$F_r(r) = -\frac{\partial}{\partial r}\Phi(r,z=0) = -4\,\pi\,G\int_0^\infty k\,J_1(kr)\left\{\int_0^\infty \tilde{\rho}(k,\zeta)\exp(-k\zeta)\,d\zeta\right\}\,dk. \tag{C.7}$$

Applying the definition Eq. (C.3) to $\tilde{\rho}(k,\zeta)$ and integrating by parts, we have

$$F_r(r) = 4\pi G\int_0^\infty J_1(kr)\left[\int_0^\infty \exp(-k\zeta)\left\{\int_0^\infty J_1(ku)\left(\frac{\partial}{\partial u}\rho(u,\zeta)\right)u\,du\right\}d\zeta\right]dk. \tag{C.8}$$

Numerical evaluation of integrals involving Bessel functions over a large range can give severe cancellation errors. Therefore it is better to exchange the order of integration and single out the integration over k. The Kernel is

$$K(r,u,\zeta) = \int_0^\infty J_1(kr)\,J_1(ku)\,\exp(-k\zeta)\,dk. \tag{C.9}$$

With the aid of formula 6.612(3) in Gradshteyn & Rizhyk (1980), we obtain

$$K(r,u,\zeta) = \frac{1}{\pi\sqrt{ru}}\,Q_{1/2}\left\{\frac{r^2+u^2+\zeta^2}{2ru}\right\} \tag{C.10}$$

where $Q_{1/2}$ is the Legendre function of the second kind and of order 1/2. By the relation 8.13.7 in Abramowitz & Stegun (1972) it can be expressed in terms of the complete elliptic integrals $\mathcal{K}$ and $\mathcal{E}$:

$$K(r,u,\zeta) = \frac{1}{\pi\sqrt{ru}}\left\{x\sqrt{\frac{2}{x+1}}\mathcal{K}\left(\sqrt{\frac{2}{x+1}}\right) - \sqrt{2(x+1)}\mathcal{E}\left(\sqrt{\frac{2}{x+1}}\right)\right\} \tag{C.11}$$

where

$$x = \frac{r^2+u^2+\zeta^2}{2ru}. \tag{C.12}$$

Making use of the transformation formulae for elliptic integrals (Gradshteyn & Rizhik 1980, formulae 8.126(3,4)):

$$\mathcal{K}\left(\frac{2\sqrt{k}}{1+k}\right) = (1+k)\,\mathcal{K}(k), \tag{C.13}$$

and

$$\mathcal{E}\left(\frac{2\sqrt{k}}{1+k}\right) = \frac{2}{1+k}\mathcal{E}(k) - (1-k)\,\mathcal{K}(k). \tag{C.14}$$

One finally obtains

$$K(r,u,\zeta) = \frac{2}{\pi\sqrt{r\,u\,p}}\{\mathcal{K}(p) - \mathcal{E}(p)\}, \tag{C.15}$$

where

$$p = x - \sqrt{x^2-1} \tag{C.16}$$

and x is defined by Eq. (C.12).

The solution of Eq. (C.7) is the formula for the radial force in the galactic plane for an axially symmetric density distribution:

$$F_r(r) = 4\pi G\int_0^\infty du\int_0^\infty d\zeta\frac{2\sqrt{u}}{\pi\sqrt{rp}}\{\mathcal{K}(p)-\mathcal{E}(p)\}\,\frac{\partial}{\partial u}[\rho(u,\zeta)]. \tag{C.17}$$

Appendix D

Taylor-Navarro Density Profile

For an isotropic, spherically-symmetric system of collision-less particles, the Jeans equation may be written as

$$\frac{d(\rho\,\sigma^2)}{dr} = -\rho\,\frac{d\,\Phi}{d\,r} = -\rho\,\frac{G\,M(<r)}{r^2}, \tag{D.1}$$

where Φ is the gravitational potential and $M(<r)$ is the mass interior to r. This equation is equivalent to the equation of hydrostatic equilibrium for a gas of pressure $P = \rho\,\sigma^2$. Dividing both sides by $-G\rho/r^2$, taking derivatives with respect to r, and using the conservation of mass, we can rewrite this equation as,

$$\frac{d}{dr}\left\{\frac{-r^2}{G\rho}\left\{\frac{d(\rho\,\sigma^2)}{dr}\right\}\right\} = \frac{d}{dr}M(<r) = 4\,\pi\,\rho\,r^2. \tag{D.2}$$

Then assuming that the phase-space density is a power-law of radius:

$$\rho/\sigma^3(r) = (\rho_0/\sigma_0^3)(r/r_0)^{-\gamma}, \tag{D.3}$$

where r_0 is an arbitrary scale radius, $\sigma_0 = \sigma(r_0)$ and $\rho_0 = \rho(r_0)$. Defining the dimensionless variables, $x = r/r_0$ and $y = \rho/\rho_0$, Eq. (D.2) can be written as,

$$\frac{d}{dx}\left\{\frac{-x^2}{y}\frac{d}{dx}\left\{y^{5/3}x^{2\gamma/3}\right\}\right\} = \kappa\,y\,x^2, \tag{D.4}$$

where

$$\kappa \equiv \frac{4\,\pi\,G\,\rho_0\,r_0^2}{\sigma_0^2} = \frac{G\,M(<r_0)/r_0}{\sigma_0^2} = \frac{V_0^2}{\sigma_0^2} \tag{D.5}$$

is a dimensionless measure of the velocity dispersion at r_0. By fixing $\gamma = 1.875$ from N-body simulations (Taylor & Navarro 2001), κ characterizes the full set of physical solutions. Eq. (D.4) admits power-law solutions. Solving for $y = x^{-\alpha}$ and assuming that $\kappa \neq 0$, that is, a finite velocity dispersion at r_0 there is a unique solution with slope $\alpha = 2.25$ and $\kappa = 1.875$. For larger values of κ the density profiles are more complex, with an outer cut-off, one or more inflection points, and an inner cusp. For κ larger than some critical value, $\kappa_{\rm crit}$, the solutions become non-monotonic, and the density vanishes at a finite radius. All solutions with $1.875 < \kappa < \kappa_{\rm crit}$ have a steep inner cusp with asymptotic slope close to $\alpha = 2.25$, but the critical solution asymptotically approaches $\alpha = 0.75$ as r tends to 0. Taylor & Navarro (2001) give the following fitting formula for the slope of the "critical" density profile,

$$\beta(x) = \frac{d\ \ln\ \rho}{d\ \ln\ x} = -\frac{0.75 + 2.625\, x^{1/2}}{1 + 0.5\, x^{1/2}}, \tag{D.6}$$

which is accurate to 3% for $x = r/r_0 < 4$. Here r_0 is the radius where the logarithmic slope of the density profile equals -2.25 and $r_0 = (5/3)r_{\rm s}$, where $r_{\rm s}$ is the NFW scale radius.

Appendix E

Analytic Expressions for Rotation Curves of Spherical Halos

For a spherical distribution of matter the circular velocity at radius r is given by

$$v^2(r) = \frac{G\,M(r)}{r}, \tag{E.1}$$

where $M(r)$ is the mass enclosed within radius r,

$$M(r) = 4\,\pi \int_0^r \rho(r', \rho_0, r_\mathrm{s})\, r'^2\, dr'. \tag{E.2}$$

In dimensionless units

$$m(x) = \int_0^x \rho(x')\, x'^2\, dx', \tag{E.3}$$

where

$$x = r/r_\mathrm{s}, \tag{E.4}$$

$$\rho(x) = \rho(r, \rho_0, r_\mathrm{s})/\rho_0, \tag{E.5}$$

and

$$M(r) = 4\,\pi\,\rho_0\, r_\mathrm{s}^3\, m(x). \tag{E.6}$$

Thus

$$v^2(x) = 4\,\pi\, G\,\rho_0\, r_\mathrm{s}^2\, \frac{m(x)}{x}, \tag{E.7}$$

and in dimensionless units

$$u^2(x) = \frac{m(x)}{x}. \tag{E.8}$$

We now give results for specific halo profiles.

E.1 Pseudo-Isothermal Sphere (ISO)

$$\rho_{\rm ISO}(x) = \frac{1}{1+x^2} \tag{E.9}$$

$$m_{\rm ISO}(x) = \int_0^x \frac{x'^2}{1+x'^2}\,dx' \tag{E.10}$$

$$= \int_0^x 1 - \frac{1}{1+x'^2}\,dx' \tag{E.11}$$

$$= x - \arctan(x) \tag{E.12}$$

$$u^2_{\rm ISO}(x) = 1 - \frac{\arctan(x)}{x} \tag{E.13}$$

E.2 Burkert Profile

$$\rho_{\rm BUR}(x) = \frac{1}{(1+x)(1+x^2)} \tag{E.14}$$

$$m_{\rm BUR}(x) = \int_0^x \frac{x'^2}{(1+x')(1+x'^2)}\,dx' \tag{E.15}$$

$$= \int_0^x \frac{1}{2(1+x')} + \frac{2x'}{4(1+x'^2)} - \frac{1}{2(1+x'^2)}\,dx' \tag{E.16}$$

$$= \frac{1}{2}\ln(1+x) + \frac{1}{4}\ln(1+x^2) - \frac{1}{2}\arctan(x) \tag{E.17}$$

$$u^2_{\rm BUR}(x) = \frac{\ln(1+x)}{2x} + \frac{\ln(1+x^2)}{4x} - \frac{\arctan(x)}{2x} \tag{E.18}$$

E.3 Alpha Density Profile

$$\rho_\alpha(x) = \frac{1}{x^\alpha(1+x)^{3-\alpha}} \tag{E.19}$$

$$\rho_{\alpha=2}(x) = \frac{1}{x^2(1+x)} \tag{E.20}$$

$$m_{\alpha=2}(x) = \int_0^x \frac{1}{1+x'}\,dx' \tag{E.21}$$

$$= \ln(1+x) \tag{E.22}$$

$$u^2_{\alpha=2}(x) = \frac{\ln(1+x)}{x} \tag{E.23}$$

$$\rho_{\alpha=1}(x) = \frac{1}{x(1+x)^2} \tag{E.24}$$

$$m_{\alpha=1}(x) = \int_0^x \frac{x'}{(1+x')^2}dx' \tag{E.25}$$

$$= \frac{-x}{1+x} + \ln(1+x) \tag{E.26}$$

$$u^2_{\alpha=1}(x) = \frac{-1}{1+x} + \frac{\ln(1+x)}{x} \tag{E.27}$$

$$\rho_{\alpha=0}(x) = \frac{1}{(1+x)^3} \tag{E.28}$$

$$m_{\alpha=0}(x) = \int_0^x \frac{1}{(1+x')^3}dx' \tag{E.29}$$

$$= \frac{-x^2}{2(1+x)} - \frac{x}{1+x} + \ln(1+x) \tag{E.30}$$

$$u^2_{\alpha=0}(x) = \frac{-x}{2(1+x)} - \frac{1}{1+x} + \frac{\ln(1+x)}{x} \tag{E.31}$$

$$\rho_{\alpha=\frac{3}{2}}(x) = \frac{1}{x^{3/2}(1+x)^{3/2}} \tag{E.32}$$

$$m_{\alpha=\frac{3}{2}}(x) = \int_0^x \frac{x'^2}{x'^{3/2}(1+x')^{3/2}}dx' \tag{E.33}$$

$$= -2\sqrt{\frac{x}{1+x}} + \int_0^x \frac{1}{\sqrt{x'(1+x')}}dx' \tag{E.34}$$

$$= -2\sqrt{\frac{x}{1+x}} + 2\ln(\sqrt{x} + \sqrt{1+x}) \tag{E.35}$$

$$u^2_{\alpha=\frac{3}{2}}(x) = \frac{-2}{\sqrt{x(1+x)}} + \frac{2\ln(\sqrt{x}+\sqrt{1+x})}{x} \tag{E.36}$$

$$\rho_{\alpha=\frac{1}{2}}(x) = \frac{1}{x^{1/2}(1+x)^{5/2}} \tag{E.37}$$

$$m_{\alpha=\frac{1}{2}}(x) = \int_0^x \frac{x'^2}{x'^{1/2}(1+x')^{5/2}}dx' \tag{E.38}$$

$$= -\frac{2}{3}\sqrt{\frac{x^3}{(1+x)^3}} - 2\sqrt{\frac{x}{1+x}} + 2\ln(\sqrt{x}+\sqrt{1+x}) \tag{E.39}$$

$$u^2_{\alpha=\frac{1}{2}}(x) = -\frac{2}{3}\sqrt{\frac{x}{(1+x)^3}} - \frac{2}{\sqrt{x(1+x)}} + \frac{2\ln(\sqrt{x}+\sqrt{1+x})}{x} \tag{E.40}$$